U.PORTO
FACULDADE DE CIÊNCIAS
UNIVERSIDADE DO PORTO

PhD

3rd CYCLE

FCUP
CAUP

U.PORTO

Building Next-Generation Tools for the Exploitation of Space-Based Seismic Data

Miguel Clara

FC

U.PORTO
FACULDADE DE CIÊNCIAS
UNIVERSIDADE DO PORTO

Building Next-Generation Tools for the Exploitation of Space-Based Seismic Data

Miguel Clara
Doctoral Program in Astronomy
Department of Physics and Astronomy
Faculty of Sciences of the University of Porto and Instituto de Astrofísica e Ciências do Espaço
2025

Building Next-Generation Tools for the Exploitation of Space-Based Seismic Data

Miguel Clara
Doctoral Program in Astronomy
Department of Physics and Astronomy
2025

Supervisor
Margarida Cunha, Researcher, Instituto de Astrofísica e Ciências do Espaço

Co-supervisors
Pedro Avelino, Researcher, Instituto de Astrofísica e Ciências do Espaço
Tiago Campante, Researcher, Instituto de Astrofísica e Ciências do Espaço



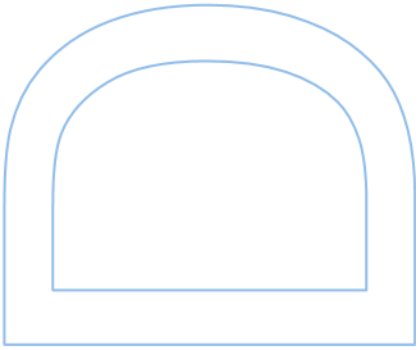


All the corrections determined by the jury, and only those, were made.

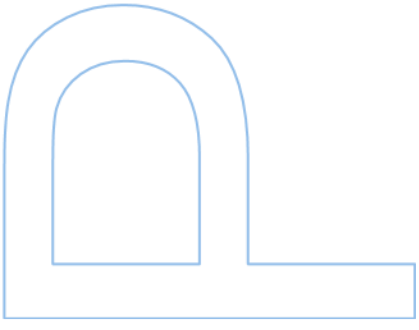
The Supervisor,

Assinado por: **Margarida Maria Salvador Cunha**
Num. de Identificação: 09873957
Data: 2026.03.09 13:32:58 +0000

Porto, _____/_____/_____







Acknowledgements

I would like to sincerely thank the projects and fellowships that made it possible for me to carry out and write this thesis. This work was supported by Fundação para a Ciência e a Tecnologia (FCT/MCTES) through national funds via a grant with reference 2020.07530.BD.

My deepest gratitude goes to my supervisors for their guidance throughout this project. In particular, I thank Margarida Cunha, whose unwavering enthusiasm for science made her a constant source of support and belief in this work. I am also grateful to Tiago Campante and Pedro Avelino for their valuable input as co-supervisors.

I would also like to thank my friends, who patiently endured my anxieties and grievances throughout the PhD program (and life in general), and who provided much-needed escapes during difficult times.

Finally, I really want to thank my parents — especially my mum — for everything: the constant presence, the care, and the heart-warming meals sent every Sunday when I visited.

Resumo

As técnicas de modelização atuais permitem determinar as propriedades estelares com grande precisão. O surgimento de modos mistos durante a fase de subgigante, cujas frequências são caracterizadas por uma rápida evolução com a idade, permitem uma determinação precisa das propriedades estelares, um objetivo fundamental para missões futuras como o PLATO. Contudo, as técnicas de modelização atuais consideram muitas vezes grelhas sem resolução suficiente para descrever adequadamente a rápida evolução da frequência do modo, o que exige o uso de algoritmos de interpolação para cobrir o espaço de parâmetros entre os modelos da grelha ao aplicar métodos de comparação entre modelos e dados observacionais.

Nesta tese, pretendemos reproduzir as frequências com $\ell = 1$ dentro dos limites de precisão tipicamente associados aos erros observacionais ($\sim$0,1 μHz) através da interpolação numa grelha de modelos de subgigantes. Para isso, utilizamos variações de um algoritmo de interpolação de dois passos, que considera dois métodos de interpolação (interpolação linear e por splines) e diferentes aproximações ou substitutos da idade da estrela (idade física, idade escalada e densidade central). Também considerámos a análise assimptótica dos modos mistos para definir um novo parâmetro, $\varphi(\rho_c)$, construído tal que as frequências variem aproximadamente de forma linear com este parâmetro.

Para os métodos de interpolação clássicos, os melhores resultados foram obtidos usando um algoritmo que considera o uso de interpolação por splines cúbicos ao longo dos trilhos evolutivos de uma estrela, interpolação linear entre os trilhos evolutivos de diferentes massas, e a densidade central $\rho_{\rm c}$ como substituto da idade estelar. Em média, esta combinação produziu um erro absoluto de 0,14 μHz, mas atingiu erros absolutos máximos 1,2 μHz para alguns modelos, valores uma ordem de grandeza superior aos erros observacionais típicos. Além disto, também investigámos o impacto na interpolação de alterações bruscas nas propriedades físicas das estrelas, mostrando, em particular, como a adição de *overshoot* no núcleo da estrela pode afetar significativamente os resultados. Também explorámos o potencial uso da análise assimptótica para melhorar os métodos de interpolação, mostrando que os resultados da interpolação em trilhos evolutivos a um valor fixo do substituto da idade $\varphi(\rho_{\rm c})$ podem ser uma ordem de grandeza menor do que quando a interpolação é realizada considerando $\rho_{\rm c}$ como o substituto da idade. No entanto, esta abordagem não considera o facto de que a representação assimptótica é específica para cada massa e ordem radial do modo, não podendo ser determinada para

estrelas com parâmetros desconhecidos. A solução encontrada para estimar as funções de transformação necessárias por meio da interpolação mostrou resultados semelhantes aos do método clássico.

Palavras-chave: astronomia, asterossismologia, estrelas: parâmetros fundamentais, estrelas: evolução, estrelas: oscilações, métodos: estatísticos

Abstract

Grid-based modelling techniques have enabled the determination of stellar properties with great precision. The emergence of mixed modes during the subgiant phase, whose frequencies are characterized by a fast evolution with age, can potentially enable a precise determination of stellar properties, a key goal for future missions like PLATO. However, current modelling techniques often consider grids that lack the resolution to properly account for the fast mode frequency evolution, consequently requiring the use of interpolation algorithms to cover the parameter space in between the grid models when applying model-data comparison methods.

In this thesis, we aim at reproducing the ℓ=1 mode frequencies within the accuracy limits associated with the typical observational errors ($\sim$0.1 μHz) through interpolation on a grid of subgiant models. For that, we used variations of a two-step interpolation algorithm, which considered linear and cubic splines interpolation methods and different age proxies (physical age, scaled age, and central density). We also considered an asymptotic analysis applied to the mixed modes, in order to define a new age proxy parameter, $\varphi(\rho_c)$, built so that the mode frequencies' dependence would vary approximately linearly with it.

For the classical methods, the best results were obtained using an algorithm that considers cubic splines interpolation along tracks, linear interpolation across tracks, and central density ρ_c as the age proxy. This combination yielded, on average, an absolute error of 0.14 μHz, but reached maximum absolute errors on the interpolated frequencies of 1.2 μHz for some models, which is an order of magnitude higher than the typical observational errors. Furthermore, we investigated the impact on the accuracy of the interpolation from changes in the physical properties of the stars, showing, in particular, how the addition of core overshoot can affect significantly the interpolation results. We also explored the potential of using asymptotic analysis to improve interpolation, showing that the results of interpolation across evolutionary tracks at a fixed value of the age proxy $\varphi(\rho_c)$ can be one order of magnitude better than when performed at fixed ρ_c. However, this approach does not consider the fact that the asymptotic representation is specific for each mass and mode radial order, and therefore cannot be determined for target stars with unknown parameters. A solution found to estimate the required transformation functions through interpolation showed results similar to those of the classical method.

Keywords: astronomy, asteroseismology, stars: fundamental parameters, stars: evolution, stars: stellar oscillations, methods: statistical

Table of Contents

List of Tables viii
List of Figures ix

1. Introduction 1
   1.1. General Background and Motivation 1
   1.2. Internal Structure of Solar-Like Stars 5
      1.2.1. The Differential Equations of Stellar Structure 5
      1.2.2. Energy Transfer in Solar-Like Stars 7
      1.2.3. Convective Boundary Mixing for Convective Cores 9
   1.3. Stellar Evolution of Low-Mass Stars in a Nutshell 16
   1.4. Theory of Stellar Pulsations 21
      1.4.1. Asteroseismology of MS Solar-Like Oscillators 25
      1.4.2. Asteroseismology in the SG Phase of Solar-Like Stars 30
   1.5. The Challenge of Interpolation for Stellar Modelling 32
2. Analytical Characterization of the Errors of Classical Interpolation Algorithms 38
   2.1. Introduction 38
   2.2. Characterization of the Stellar Grid and the Method 39
      2.2.1. Input physics of the stellar grid 40
      2.2.2. Interpolation methods 43
   2.3. Results of the Interpolation Tests 45
      2.3.1. Interpolation Along Evolutionary Tracks 46
      2.3.2. Full Interpolation with τ and τ_{scaled} as Age Proxies 49
      2.3.3. Central density ρ_c as an Alternative Age Proxy 50
      2.3.4. Results for the Full Grid 55
      2.3.5. Impact of the Order of Interpolation 56
      2.3.6. Testing the Grid Resolution 58
   2.4. Conclusions 61
3. The Effects of Convective Boundary Mixing on Interpolation 63
   3.1. Introduction 63
   3.2. The Convective Overshoot Problem in our Grid 67
   3.3. Discussing Solutions for the Convective Overshoot Problem 71
   3.4. Conclusions 75
4. A Mixed Mode Motivated Interpolation Algorithm 77
   4.1. Introduction 77
   4.2. Interpolation using $\varphi(\rho_c)$ as an Alternative Age Proxy 80

5. Conclusions 90

Bibliography 93

A. Interpolation Errors of $\ell = 1$ Modes Resulting from Interpolation Along Evolutionary Tracks 105

B. Interpolation Errors of $\ell = 1$ Modes Resulting from the Full Interpolation Algorithm ... 112

C. Testing Grid Resolution 117

List of Tables

2.1. Average offsets and maximum errors from interpolation along the evolutionary track with 1.245 $M_\odot$, for all $\ell = 0$ mode frequencies, considering the indicated interpolation algorithms. 47
2.2. Average offsets and maximum errors from interpolation along the evolutionary track with 1.245 $M_\odot$, for all $\ell = 1$ mode frequencies, considering the indicated interpolation algorithms. 48
2.3. Average offset and maximum errors from the full interpolation algorithm for all $\ell = 0$ modes associated with the evolutionary track with 1.245 $M_\odot$, for each of the age proxies indicated. 50
2.4. Average offset and maximum errors from the full interpolation algorithm, for all $\ell = 1$ modes associated with the evolutionary track with 1.245 $M_\odot$, for each of the age proxies indicated. 51
2.5. Average offsets and maximum errors resulting from interpolation along the evolutionary track with $M = 1.245$ $M_\odot$ (considering a cubic polynomial or cubic splines method), when considering ρ_c as the age proxy, for all associated $\ell = 1$ mode frequencies, and for the indicated grid resolutions, $1/k$. 59
2.6. Average offsets and maximum errors from the full interpolation algorithm (that considers cubic splines along tracks, the indicated interpolation method across tracks - linear or cubic splines, - and ρ_c as the age proxy) applied to all ℓ = 1 modes associated with the evolutionary track with $M = 1.245$ $M_\odot$, for different grid resolutions, $1/k$. 60

A.1. Average offsets and maximum errors from interpolation along evolutionary tracks, for all $\ell = 1$ modes associated with the missing models of each evolutionary track of the stellar grid, determined from interpolation using adjacent models of the same evolutionary track, for each of the age proxies indicated. 105

B.1. Average offsets and maximum errors from the full interpolation algorithm (that considers cubic splines along tracks and the indicated interpolation method across tracks), for all $\ell = 1$ modes associated with the interpolated evolutionary tracks of the grid, determined from interpolation using adjacent evolutionary tracks, for each of the age proxies indicated. 112

C.1. Average offsets resulting from interpolation along frequency curves determined using Equation C.2 (with 200 and 2000 initial models), when considering three interpolation methods (linear, cubic polynomial, and cubic splines), ρ_c as the age proxy, and the indicated grid resolutions, $1/k$. 119

List of Figures

1.1. Internal structure of solar-like stars and dependence of the temperature gradients ∇, ∇_{rad} and ∇_{ad} on the dimensionless radius, for models of MS solar-type stars with 1.1 and 1.2 $M_\odot$ and $X_c = 0.18$. 9
1.2. Schematic of the internal structure of a solar-like star with a convective core, a convective overshoot region, and different convective overshoot prescriptions applied to the convective core boundary of MS solar-type stars. 12
1.3. Evolution of the hydrogen content at the stellar centre for MS models with 1.2 and 1.5 $M_\odot$, under the Schwarzschild criterion without overshoot and the models with convective overshooting' prescriptions. 14
1.4. Impact of increasing the size of the convective overshoot region on different stellar parameters at the TAMS ($T_{eff,TAMS}$, $\log L_{TAMS}$, τ_{TAMS}, $m_{He,TAMS}$), for models of three initial masses. 15
1.5. Internal structure of a 1.5 $M_\odot$ stellar MS model, displaying the hydrogen abundance, the adiabatic gradient, the radiative gradient, and the Ledoux gradient as a function of the mass fraction. 15
1.6. Schematic diagram of the evolution of a one solar-mass, from the ZAMS to the formation of a white dwarf. 17
1.7. Evolution of the internal structure of a model star with M =1.10 $M_\odot$, as a function of the ρ_c, τ_{scaled} and the stellar radius r/R_*, during its MS and SG phases. 18
1.8. Evolution of the internal structure of a model star with M =1.20 $M_\odot$, as a function of the ρ_c, τ_{scaled} and the stellar radius r/R_*, during its MS and SG phases. 18
1.9. Evolution of various stellar parameters for stellar models with 1.1 and 1.2 $M_\odot$. 20
1.10. Propagation diagrams for models of a 1 $M_\odot$ star in the main sequence, subgiant, and red-giant phases. 26
1.11. Fourier power density spectrum of the MS star *Kepler* target 16 Cyg A. 28
1.12. Evolution of stellar and asteroseismic properties with age, for a 1.3 $M_\odot$ model, during the late MS and subgiant phases. 31
1.13. Evolution of the normalized frequencies of non-radial $\ell = 1$ modes, with $n = 11$, for evolutionary tracks of a stellar grid with masses between 1.23 and 1.27 $M_\odot$, as a function of τ and ρ_c. 36

2.1. Hertzsprung–Russell diagram displaying every tenth model of each of the 41 subgiant tracks of the stellar grid. 41
2.2. Evolution of $\ell = 0$ and 1 normalized mode frequencies with τ_{scaled} and ρ_c, for a mass track with 1.245 $M_\odot$. 43
2.3. Schematic of the 2-step interpolation procedure. 45
2.4. Interpolation errors as a function of τ_{scaled} and ρ_c, that resulted from interpolation along the evolutionary track with M = 1.245 $M_\odot$, for all $\ell = 0$ frequency modes. 47
2.5. Interpolation errors as a function of τ_{scaled} and ρ_c, that resulted from interpolation along the evolutionary track with M = 1.245 $M_\odot$, for all $\ell = 1$ frequency modes. 48
2.6. Interpolation errors as a function of τ_{scaled} and ρ_c, that resulted from the full interpolation algorithm for all ℓ=0 modes associated with the mass track M = 1.245 $M_\odot$, when considering τ, τ_{scaled} and ρ_c as age proxies. 52
2.7. Interpolation errors as a function of τ_{scaled} and ρ_c, that resulted from the full interpolation algorithm for all $\ell = 1$ modes associated with the track with M = 1.245 $M_\odot$, when considering τ, τ_{scaled} and ρ_c as age proxies. 53

2.8. Interpolation errors as a function of τ_{scaled} and ρ_c, that resulted from the full interpolation algorithm for all $\ell = 1$ modes associated with the track with $M = 1.245$ $M_\odot$, when considering τ, τ_{scaled} and ρ_c as age proxies. 54
2.9. Evolution of the scaled frequencies for the $\ell = 0$ modes, with radial order n=11, resulting from the application of the interpolation algorithm to the mass track with 1.245 $M_\odot$, presented as a function of τ and τ_{scaled}, when each is considered as the respective age proxy for interpolation. 56
2.10. Evolution of the normalized frequencies of $\ell = 1$ modes, for evolutionary tracks of the stellar grid with masses between 1.23 and 1.26 $M_\odot$, as a function of the various age proxies: τ, τ_{scaled}, and ρ_c. 57
2.11. Average offsets and maximum errors from the full interpolation method, and τ_{scaled} or ρ_c as the age proxy, for all $\ell = 1$ modes obtained for the interpolated tracks of the initial grid. 58

3.1. Inferred effective overshoot parameter $\alpha_{\text{ov,eff}}$ shown as a function of the modelled stellar mass, for the sample of 62 early post-MS stars from Lindsay et al. (2024). 64
3.2. Inferred effective overshoot parameter $\alpha_{\text{ov,eff}}$ obtained from various works as a function of the stellar mass. 65
3.3. Inferred convective overshoot values (f_{ov}) shown as a function of stellar mass, for the sample of dwarf and giant double-line eclipsing binaries presented in Claret and Torres (2018). 66
3.4. Interpolation errors as a function of τ_{scaled} and ρ_c, that resulted from the application of the full interpolation algorithm across the full grid. 68
3.5. Evolution of the frequency of ℓ=1 mode frequencies with mass, for ρ_c=16000 g.cm^{-3}. 69
3.6. Evolution of the $\nu_{1,11,\text{norm}}$ mode frequency along an avoided crossing taking place at central densities between 13000 and 18000 g.cm^{-3}, for models of the first subgrid. 69
3.7. Interpolation errors as a function of τ_{scaled} and ρ_c, that resulted from the application of the full interpolation algorithm to the first subgrid (with f_{ov}=0.01). 70
3.8. Evolution of the mass of the convective core during the MS phase as a function of the scaled age of the MS, for the different mass inputs of our subgrids (with $f_{\text{ov}} = 0.01$ and $f_{\text{ov}} = 0.00$). 71
3.9. Evolution of the $\nu_{1,11,\text{norm}}$ mode frequency along an avoided crossing taking place at central densities between 13000 and 18000 g.cm^{-3}, for the models of the stellar subgrid with f_{ov}=0.00. 72
3.10. Evolution of the central temperature with $\tau_{\text{scaled,SG}}$ for the two subgrids discussed in this section, with $f_{\text{ov}} = 0.01$ and $f_{\text{ov}} = 0.00$. 73
3.11. Interpolation errors as a function of τ_{scaled} and ρ_c, that resulted from the application of the full interpolation algorithm to the second subgrid, with $f_{\text{ov}} = 0.00$. 74
3.12. Interpolation errors as a function of τ_{scaled} and ρ_c, that resulted from the application of the full interpolation algorithm to the third subgrid, with $f_{\text{ov}}(M)$. 75

4.1. Evolution of the $\ell = 1$ frequency modes, along with the inferred trajectories of the corresponding pure g-modes and pure p-modes as a function of ρ_c, for a track with $M = 1.245$ $M_\odot$. 80
4.2. Evolution of the $\nu_{1,11,\text{norm}}$ frequency modes and the corresponding estimated fitting functions for each mass, expressed as a function of ρ_c, for all evolutionary tracks of the grid. 83
4.3. Results of the variable transformation algorithm, shown for all $\nu_{1,11,\text{norm}}$ frequency modes of the stellar grid. 84

4.4. Interpolation errors resulting from the full interpolation algorithm as a function of ρ_c, for all $\nu_{1,11}$ frequency modes in the stellar grid, and considering ρ_c or $\varphi(\rho_c)$ as the age proxy. 85
4.5. Evolution of the frequency modes $\nu_{1,11,\mathrm{norm}}$ as a function of ρ_c and $\varphi(\rho_c)$, for the masses near the transition where the core becomes convective. 85
4.6. Comparison of the residuals from the fitting process and the interpolation errors, that resulted from the variable transformation of both known and unknown frequency fitting functions. 87
4.7. Average offsets and maximum errors obtained for all $\ell = 1$ modes of the interpolated tracks of the initial grid. The results are presented for the three interpolation methods discussed in this section. 88

C.1. Results of applying the fitting function to $\ell = 1$ frequency modes with various radial orders n, computed using GYRE for the mass track with 1.245 $M_\odot$ from our initial grid. 118
C.2. Results of interpolation tests applied to the resolution of frequency modes of an evolutionary track in the SG phase, through the comparison of the results of interpolation applied to two frequency functions, one with an original track of 200 models and another with 2000 models, and of their degraded versions, with resolutions $1/k$ in respect to the original function. 120

1. Introduction

1.1. General Background and Motivation

Located a few to several thousands of light-years away, the stars that illuminate our night sky, like celestial fireflies, are of huge interest across numerous fields of astronomy, and constitute the main focus of stellar astrophysics. Stars possess physical, chemical and kinematic properties that reveal their structural, dynamical and evolutionary histories up to their present age. In relation to the rest of the Universe, stars interact in many significant ways with their surroundings. Not only do they contribute to the chemical evolution of the entire Universe, but are also the progenitors of numerous astronomical objects and events, such as supernovae, planetary nebulae, and black holes, that contribute to the Universe's evolution. Moreover, stars are also the hosts of exoplanets, whose properties are naturally connected to those of their host.

Despite a well-established framework, the modelling of the structure and evolution of stars still involves major uncertainties regarding how energy is produced and transported inside the star, how stars mix chemical elements, and how stellar matter behaves under extreme conditions.

Asteroseismology, the study of the internal structure of stars through the analysis of their intrinsic global oscillations, has significantly contributed to improving our understanding of stellar interiors and their evolution. Through the analysis of resonant oscillations observed in their oscillation spectra, we can infer internal stellar properties, and obtain unique insights that traditional observations cannot provide.

Once limited to theoretical studies constrained by observations of surface properties alone, the study of stellar interiors has advanced rapidly with modern asteroseismic techniques and the development of new observing facilities. Today, supported by a combination of stellar pulsation theory and an unprecedented volume of high-quality asteroseismic data from space missions such as the *Convection, Rotation and planetary Transits* mission (CoRoT; Baglin et al. (2006)), *Kepler* (Gilliland et al. (2010), Koch et al. (2010)), the *Transiting Exoplanet Survey Satellite* (TESS; Ricker et al. (2015), Campante et al. (2016), Cunha et al. (2019)), and the upcoming *PLAnetary Transits and Oscillations of stars* mission (PLATO; Rauer et al. (2014), Cunha et al. (2021a), Rauer et al. (2023), Goupil et al.

(2024)), stellar pulsations can be used to make robust inferences on stellar properties, internal structure, and dynamics.

In stellar astrophysics, the inputs that are used to model stars, and that are essential for understanding stellar structure, evolution, and dynamics, can be broadly classified into three groups:

1. Basic parameters: these correspond to the stellar fundamental properties, like mass (M) and initial chemical abundances, specifically the mass fractions of hydrogen (X), helium (Y), and heavy elements (Z)*. These parameters are fundamental inputs for stellar models, providing the initial conditions for evolutionary calculations.

2. Adopted physics: these refer to the set of physical assumptions implemented in stellar models, which affect the internal structure and evolution of a star. These include nuclear reaction networks, the equation of state, and opacities.

3. Parametrized physics: certain physical processes, such as convection and overshooting, are modelled using free parameters like the mixing-length parameter ($\alpha_{\rm MLT}$) and the overshoot parameter ($\alpha_{\rm ov}$). These parameters are not directly observed but are necessary in stellar modelling, and can be treated as input variables within stellar model grids - meaning that the aspects we can control represent only part of a more complex underlying physical process that remains incompletely understood. Together with the basic parameters defined in 1. and stellar age, they usually form the models' parameter space, for a fixed adopted physics.

In the context of asteroseismology, these stellar parameters (defined in 1. and 3.) can be determined for observed stars using current asteroseismic inference approaches that aim to identify the best-fitting stellar parameters by minimizing the differences between pre-calculated models and observations, based on *a priori* selected criteria. These models are generated using stellar evolution codes such as *Modules for Experiments in Stellar Astrophysics* (MESA), *Aarhus STellar Evolution Code* (ASTEC) and *Code d'Évolution Stellaire Adaptatif et Modulaire* (CESAM), together with pulsation codes such as the GYRE stellar oscillation code and the *Aarhus adiabatic oscillation package* (ADIPLS)). Typically, these fittings are performed considering a group of observational constraints established *a priori*. When modelling a single star, common classical constraints include the effective

*More commonly used throughout this work is the iron-metallicity, which serves as a proxy for the overall metallicity of the star, and that can be obtained as the abundance of iron in a star relative to that of hydrogen, as expressed by the equation $[\mathrm{Fe/H}]=\log_{10}\left(\frac{(\mathrm{Fe/H})_*}{(\mathrm{Fe/H})_\odot}\right)$.

temperature, $T_{\rm eff}$, the surface metallicity, [Fe/H]$_{\rm surf}$, and the stellar luminosity, L (or, when L is not available, the surface gravity, $\log(g)$). Meanwhile, the seismic data have provided additional constraints like the large frequency separation, $\Delta\nu$, and the frequency of maximum power, $\nu_{\rm max}$. Today, with increasing instrumental precision, it is also possible to extract individual oscillation frequencies from the data, which can be used as asteroseismic constraints, not only for the determination of the stellar global properties, but also to probe the internal structure and dynamics of stars.

The fitting procedure is often performed through the use of optimization algorithms that aim to minimize the chi-square (χ^2) function

$$\chi^2 = \sum_i [(y_i^{\rm obs} - y_i^{\rm mod})/\sigma_i]^2 \tag{1.1}$$

with respect to parameters $\{a_j\}$, where $y_i^{\rm obs}$ are the observed values of the observables (the constraints), $y_i^{\rm mod}$ are the corresponding model values computed for the given set of model parameters and σ_i are the uncertainties of the observations. These methods search for the best-fitting parameters within a defined physical setting, yielding a model that best matches the observed data and, depending on the approach, also probability distributions for a suit of stellar properties.

In this work, we are mostly interested in solar-like pulsators; stars in various phases of evolution - spanning from the main sequence (MS) to the red giant (RG) phase - with masses between 0.7 and 2.0 $M_\odot$, and whose oscillations are driven by stochastic motions of near-surface convection. Within these, we will focus particularly on subgiant stars (SG), whose seismic data are known to be particularly constraining. Indeed, the oscillation spectra of subgiant stars are characterized by mixed modes - oscillatory modes whose frequencies evolve rapidly as a star evolves, and which are highly sensitivity to the core structure. Despite their constraining power, these stellar pulsators have not received as much attention in the literature as main sequence pulsators. Examples of state-of-the-art studies include Huber et al. (2019), Stokholm et al. (2019), Li et al. (2020), Bellinger et al. (2021) and Noll et al. (2021).

The work in this thesis builds on previous work conducted by Clara (2019), where we applied the optimization algorithm *Asteroseismic Inference on a Massive Scale* (AIMS; Rendle et al. (2019)) to fit simulated data of subgiant stars produced for an Hares & Hounds (H&H) exercise, similar to the approach used for the simulated MS stars discussed in Cunha et al. (2021b). The H&H exercise focused on determining the best optimization

procedure to model solar-like pulsators in the subgiant phase. However, due to the presence of mixed modes, whose frequencies vary on a very short timescale (in evolutionary terms), we found it impossible to retrieve most stellar properties within the scientific requirements established for the PLATO mission. The accuracy of the mode frequency interpolation in the grid of models was identified as a potential source of the problem, partly motivating the studies carried out in this thesis.

In this thesis, we conduct a characterization of classical interpolation algorithms applied to the determination of the pulsation frequencies in the subgiant evolutionary phase and discuss the problems associated with them. In particular, we establish which method is capable of most accurately describing model frequencies interpolated both along and across evolutionary tracks of a two-parameter stellar grid. We also explore other, more complex interpolation methods, characterizing them and testing if they can perform better than their classical counterparts. As a reference, we compare the interpolation errors with typical observational errors of $\delta\nu \sim 0.1\mu$Hz (Li et al., 2020), which we set as our main accuracy target for the frequencies of the oscillation modes.

In this thesis, we will address challenges associated with frequency interpolation during the subgiant phase of stellar evolution. To that end, in the remainder of this introductory chapter, we will discuss four key topics that are essential for understanding the work presented in this thesis. In Section 1.2, we examine the theory describing the internal structure of solar-like stars, introducing the equations of stellar structure, the mechanisms of energy transport, and aspects related to convective boundary mixing, associated with the core convective overshoot problem in stellar modelling. These topics are relevant for understanding the different phases of solar-like stellar evolution, which are discussed in Section 1.3, with particular emphasis to the main sequence and subgiant phases. In Section 1.4, we summarize the theory of adiabatic stellar pulsations, presenting the fundamental equations and the necessary approximations, with a focus on solar-like pulsators, especially in the MS and SG phases. Finally, in Section 1.5, we introduce the forward modelling methods used in optimization procedures, and motivate the need for performing interpolation when using grids of models, highlighting the potential problems that may be associated to that procedure.

With the stage set by Chapter 1, we begin Chapter 2 by describing the grid of stellar models and the classical interpolation methods we intend to characterize. We analyse the interpolation errors associated with the application of the different interpolation methods

to the stellar grid, taking into account different interpolation schemes and choices of age proxies. We begin by considering interpolation only along an evolutionary track, before addressing the more general case of interpolation across the mass tracks of the grid. We also discuss the influence of different grid resolutions on the interpolation errors.

In Chapter 3, we investigate a specific problem associated to interpolation across mass tracks in the mass range where MS models begin to develop a convective core. We discuss the reason why interpolation can be particularly challenging in this part of the parameter space and how the overshoot parameter $f_{\rm ov}$ influences the interpolation results, accessing how this problem can be mitigated or resolved.

In Chapter 4, we make use of the asymptotic analysis of stellar pulsations to develop a more sophisticated frequency interpolation algorithm that may better satisfy the accuracy requirements we adopt as a reference, set by the typical observational error of 0.1 μHz.

Finally, in Chapter 5, we summarize the main results of this thesis.

1.2. Internal Structure of Solar-Like Stars

1.2.1 The Differential Equations of Stellar Structure

The evolution of a star is governed by the energy it generates in its core and radiates into space. This is especially clear during the long stable phases of stellar life, such as the main sequence, as a star uses the energy it produces to maintain its interior in hydrostatic equilibrium. During such periods, at any given time, its structure can be described by four differential equations. These then slowly evolve with time due to gravitational contraction, the nuclear reactions taking place at the stellar core, and the resulting changes in the chemical composition.

These differential equations rely on several simplifications in order to be valid: spherical symmetry (which allows parameters to depend solely on the radial direction, r), hydrostatic equilibrium, and the absence of rotation, magnetic fields, or other large-scale variations.

Consider a star in equilibrium at a given moment in time, during its evolution. Within that star, consider shells of mass dm, thickness dr' and density $\rho(r')$, located at a distance $r' \leq r$ from the centre of the star. The mass $m(r)$, within a radius r, is the sum of the

masses of all those shells. It is then given by

$$m(r) = \int_0^r 4\pi r'^2 \rho(r') dr'. \tag{1.2}$$

Differentiating such equation, and expressing it in terms of dm, we obtain

$$\frac{dr}{dm} = \frac{1}{4\pi r^2 \rho}\,, \tag{1.3}$$

which expresses the mass conservation.

Since stars do not evolve on a dynamical timescale, there must be an equilibrium between the forces acting in the stellar interior. Consider a mass shell with thickness dr, surface area dA, and mass dm, at a distance r from the centre. For such hydrostatic equilibrium to hold, the sum of all forces acting on the mass shell (i.e. the gravitational force and the pressure force) must be zero,

$$F_{\text{total}} = F_g + F_P = \left(-\frac{Gm}{r^2} dm\right) + \left(-\frac{dP}{dr} dr dA\right) = 0 \tag{1.4}$$

where P is the pressure and G is the gravitational constant. Rearranging these terms, Equation 1.4 simplifies to

$$\frac{dP}{dr} = -\frac{Gm}{r^2}\rho \tag{1.5}$$

or, when expressed in terms of dm,

$$\frac{dP}{dm} = -\frac{Gm}{4\pi r^4}, \tag{1.6}$$

which expresses the hydrostatic equilibrium.

Such equilibrium also requires a balance between the energy generated within the stellar interior and the energy lost to space. In general, considering the rate at which energy flows in and out of a shell located at a radius r and with local luminosity L_r, we obtain the following relationship

$$\frac{dL_r}{dm} = \varepsilon_{\text{nuc}} + \varepsilon_{\text{g}} - \varepsilon_\nu. \tag{1.7}$$

This equation corresponds to the energy conservation equation, and it highlights the primary sources of energy variation in a stellar shell: ε_{nuc} is the energy production rate per unit of mass due to nuclear reactions in the stellar core; ε_{g} is the energy absorbed or released per unit mass and time during any expansion or contraction of the star; and ε_ν is the energy loss rate per unit of mass by the star in the form of neutrinos.

Finally, there is a steady flow of energy from the deep interior, where nuclear reactions

take place, to the outermost layers of the star, where energy is radiated into the interstellar medium. The physics of energy transport allows us to establish a fourth equation for the stellar structure: the energy transport equation. This equation will be examined in greater detail in the following sections.

1.2.2 Energy Transfer in Solar-Like Stars

Within a star, energy is transferred through stellar material from the core to the outer layers thanks to a non-vanishing temperature gradient in the stellar interior. Depending on the thermodynamic properties of the local environment, this energy transfer can occur via radiative transfer or convective motions*, where photons and, in some cases, convective elements are exchanged between hotter and cooler environments.

When energy is only transported by radiation under the diffusion approximation, valid in regions inside the stars at high optical depth, the radiative transfer can be expressed as

$$\frac{dT}{dm} = -\frac{3}{64\pi^2 ac}\frac{\kappa L}{r^4 T^3}, \tag{1.8}$$

where a is the radiation density constant, c is the speed of light, κ is the mean opacity of the environment, and ρ is the local density. This equation expresses the temperature gradient required to transport a luminosity L to the surface.

Using the chain rule, assuming hydrostatic equilibrium (from Equation 1.6), and defining the temperature gradient as

$$\nabla = \frac{d\ln T}{d\ln P}, \tag{1.9}$$

we further have

$$\frac{dT}{dm} = \frac{dT}{dP}\frac{dP}{dm} = -\frac{GmT}{4\pi r^4 P}\nabla. \tag{1.10}$$

Thus, the radiative temperature gradient, expressing the temperature variation within the star when radiation is the only mechanism behind energy transport, is given by

$$\nabla_{\text{rad}} = \left(\frac{d\log T}{d\log P}\right)_{\text{rad}} = \frac{3}{16\pi acG}\frac{\kappa LP}{mT^4}. \tag{1.11}$$

In a layer where energy is transported by radiation, the actual temperature gradient, ∇, satisfies

$$\nabla = \nabla_{\text{rad}}. \tag{1.12}$$

*Conductive transfer is also a possibility for energy transfer, but it is only efficient under degenerate conditions, which are not characteristic of the stellar phases we are discussing.

However, when the radiative temperature gradient becomes too steep, the energy transfer through radiation is not sufficiently efficient, and convective instabilities set in. Convection is an efficient form of energy transport that occurs when a region becomes dynamically unstable, allowing hotter and cooler layers to exchange energy through the motion of macroscopic mass elements (also called convective blobs).

Within convective cores and throughout most convective envelopes, this process is very efficient and, as a result, the temperature gradient is essentially adiabatic. Thus, in a layer where energy is transported by convection, the temperature gradient satisfies approximately

$$\nabla = \nabla_{\rm ad}, \tag{1.13}$$

where the adiabatic temperature gradient is given by

$$\nabla_{\rm ad} = \left(\frac{d\ln T}{d\ln P}\right)_{\rm ad}. \tag{1.14}$$

In practice, the analysis of the stability of the plasma against convection establishes that in the absence of chemical gradients, the preferred energy transport process is the one that results in the smallest temperature gradient at each position within the stellar interior: radiative transport if $\nabla_{\rm rad} < \nabla_{\rm ad}$, or convection if $\nabla_{\rm ad} < \nabla_{\rm rad}$* (Schwarzschild criterion; Schwarzschild (1958)).

Accordingly, Figure 1.1 presents the expected internal structure for two solar-like stars in their MS, with masses 1.10 $M_\odot$ and 1.20 $M_\odot$. We can see that stars with $M \lesssim 1.1$ $M_\odot$† typically have a radiative core and a convective envelope, while stars with $M \gtrsim 1.1$ $M_\odot$ exhibit a convective core and a radiative envelope, potentially with a convective outer shell near the surface (as seen for the star with $M = 1.20$ $M_\odot$ in Figure 1.1).

We establish the boundary of the convective core at the position of neutral stability, defined as when $\nabla_{\rm rad} = \nabla_{\rm ad}$. However, this boundary is not rigid, essentially relying on the local buoyancy forces. The rising convective elements, which are accelerated within the convective core, can break through the convective core boundary due to their inertia. Beyond this point, the motion of these elements is slowed down, causing them to mix with their surroundings and altering their composition. This is the problem behind convective overshoot.

*Nearly adiabatic stratification (with $\nabla = \nabla_{\rm ad}$) is assumed in the convective region, while $\nabla = \nabla_{\rm rad}$ is assumed in the radiative region.

†The actual stellar mass at which stars begin to develop a convective core depends on additional physical properties, such as metallicity, [Fe/H], and the mixing length parameter, $\alpha_{\rm MLT}$.

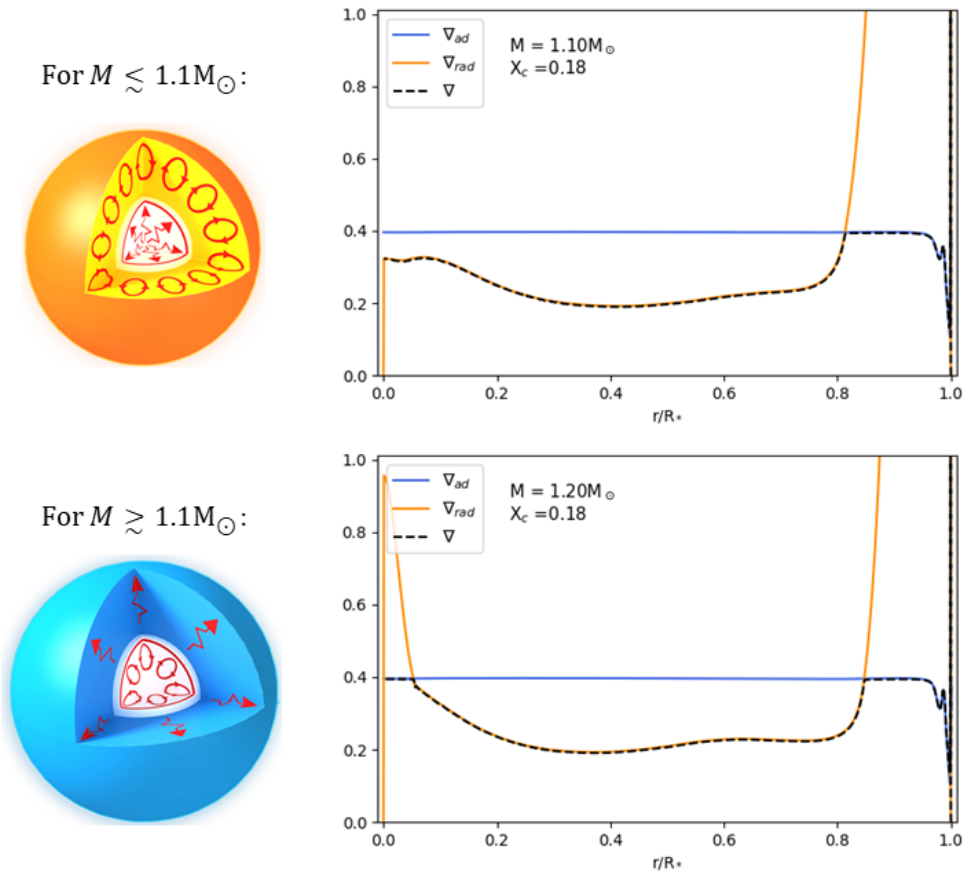


Figure 1.1: Internal structure of solar-like mass stars (left) and dependence of the temperature gradient (∇), radiative gradient ($\nabla_{\rm rad}$) and adiabatic gradient ($\nabla_{\rm ad}$) on the fractional radius (r/R_*) (right), for models of MS solar-type stars with masses $M = 1.1$ M$_\odot$ (top) and $M = 1.2$ M$_\odot$ (bottom), and with a central hydrogen mass fraction $X_c = 0.18$. The boundaries between convective and radiative regions were determined according to the Schwarzschild criterion (Schwarzschild, 1958). Stellar schemes on the left adapted from Creative Commons.

1.2.3 Convective Boundary Mixing for Convective Cores

Convection occurs in all MS stars. These convective regions, where the temperature gradient follows the adiabatic gradient ($\nabla = \nabla_{\rm ad}$), exhibit important properties that can be described by bulk convection theories. The mixing length theory for convection (MLT, Böhm-Vitense (1958)) is widely accepted as providing a reliable prescription for 1D stellar evolutionary codes, with empirical tests of the resulting stellar models showing a very strong agreement with observations*.

The MLT provides a simple method for treating convection locally, at any point inside the star. According to this theory, the transporting mass elements (*convective blobs*) can carry energy over a certain distance, after which the mass elements dissolve into

*For the general theory and equations, see Kippenhahn et al. (2013), Chapter 7.

their surroundings. The distance a fluid element can traverse before dissolving into its surroundings is

$$l_{\mathrm{m}} = \alpha_{\mathrm{MLT}} H_{\mathrm{P}} \tag{1.15}$$

where H_{P} is the pressure scale height* and α_{MLT} is a free parameter. Although α_{MLT} establishes the level of convective efficiency, it can only be determined through standard solar calibration, with typical values ranging from 1.5 to 2.5†.

However, the MLT is, by design, unable to properly model the interface between convective and radiative zones. According to this theory, the flow simply stops at the convective boundary, which contradicts basic principles in physics, as inertia acting on convective elements can allow them to penetrate beyond the convective boundary and induce mixing in the stable stratified (radiative) region. This physical mechanism is commonly referred to as convective overshoot.

When formulating a prescription for overshoot, there are two key questions that must be addressed: (a) how does the thermal structure of the overshooting region is affected by the extra mixing (a problem addressed by the penetrative overshoot and the convective overshoot prescriptions‡); and (b) what is the nature of this extra mixing beyond the convective core (a problem addressed by the step overshoot and the exponential diffusive overshoot prescriptions§). The principals behind these prescriptions are summarized in Figure 1.2. However, note that the terminology of this field is broadly defined, and may vary from author to author. Here, we adhere to the terminology used in Viallet et al. (2015), Pedersen et al. (2018) and Anders and Pedersen (2023).

If the convective boundary is located deep inside the star and the heat transport is efficient enough to mix both chemical elements and entropy, then the overshooting flow can establish a nearly adiabatic stratification, and extend the convection core into the radiative domain, even though it remains stable to convection (i.e. $\nabla \simeq \nabla_{\mathrm{ad}}$ in the overshooting region, despite $\nabla_{\mathrm{rad}} < \nabla_{\mathrm{ad}}$, as shown in Figure 1.2a). This is a case of penetrative

*H_{P} is the pressure scale height, given by $H_{\mathrm{P}}^{-1} = -\frac{d \ln P}{dr}$. In hydrostatic equilibrium, $H_{\mathrm{P}} = P/(\rho g)$.

†Higher α_{MLT} values are associated with more efficient convective transport, causing an evolutionary track in the HR diagram to shift towards higher luminosities.

‡Viallet et al. (2015) and Anders and Pedersen (2023) present a third possibility, where shear flows and overshooting motions drag material from the radiative zone into the convective zone - turbulent entrainment. However, this prescription is limited to the deep stellar interior, occurring when evolution is driven by neutrino losses (in the late stages of stellar evolution) or when there is a strong thermal imbalance (e.g., during the He-flash phase in low-mass stars).

§Other approaches are discussed in Pedersen et al. (2018) and Anders and Pedersen (2023).

overshoot*, whose profile of the diffusion coefficient is given by

$$D_{\text{ov}}(r) = D_0, \text{ for } r_{\text{cc}} < r < r_{\text{cc}} + z_{\text{ov}}, \tag{1.16}$$

implemented by artificially increasing the size of the adiabatic region from r_{cc}, the radius of the convective core, over an overshoot region with thickness z_{ov}. Additionally, chemical mixing is assumed to be instantaneous.

However, if fluid motions beyond the convective boundary can transport both chemical elements and momentum, but heat transport is inefficient, then overshoot does not affect the thermal structure (i.e. $\nabla = \nabla_{\text{rad}}$ in the overshooting region, as shown in Figure 1.2b). This is the case of convective overshoot, where mixing is not necessarily instantaneous anymore.

In the case of inefficient convection, we can model overshoot either as an instantaneous mixing or a diffusive process. When (quasi-)instantaneous, all chemical elements are homogeneously distributed in the overshooting region and the chemical mixing can be modelled through a step overshoot prescription (as illustrated in Figure 1.2c), whose profile of the diffusion coefficient

$$D_{\text{ov}}(r) = D_0, \text{ for } r_{\text{cc}} < r < r_{\text{cc}} + l_{\text{ov}} \tag{1.17}$$

is applied over an extension $l_{\text{ov}} = \alpha_{\text{ov}} H_{\text{P,cc}}$ beyond the convective core boundary (r_{cc}), where D_0 is a constant diffusion coefficient measured at the convective core boundary, $H_{\text{P,cc}}$ is the pressure scale height at the convective core boundary, and α_{ov} is a free parameter that measures the extent of the overshoot region into the radiative envelope. This simple description results from the simplified 1D description of convection in the mixing length theory (Böhm-Vitense, 1958), which is a common choice adopted by evolution codes like MESA.

When treated as a diffusive process, the chemical mixing is modelled through an exponential diffusive overshooting prescription (as illustrated in Figure 1.2d), which assumes that the vertical velocities of the convective elements decay exponentially with the distance from the convective core boundary (according to Herwig (2000) and Pedersen et al.

*This approach is more useful when convection is more efficient, such as in cases of core overshooting during the MS and convective envelope undershooting.

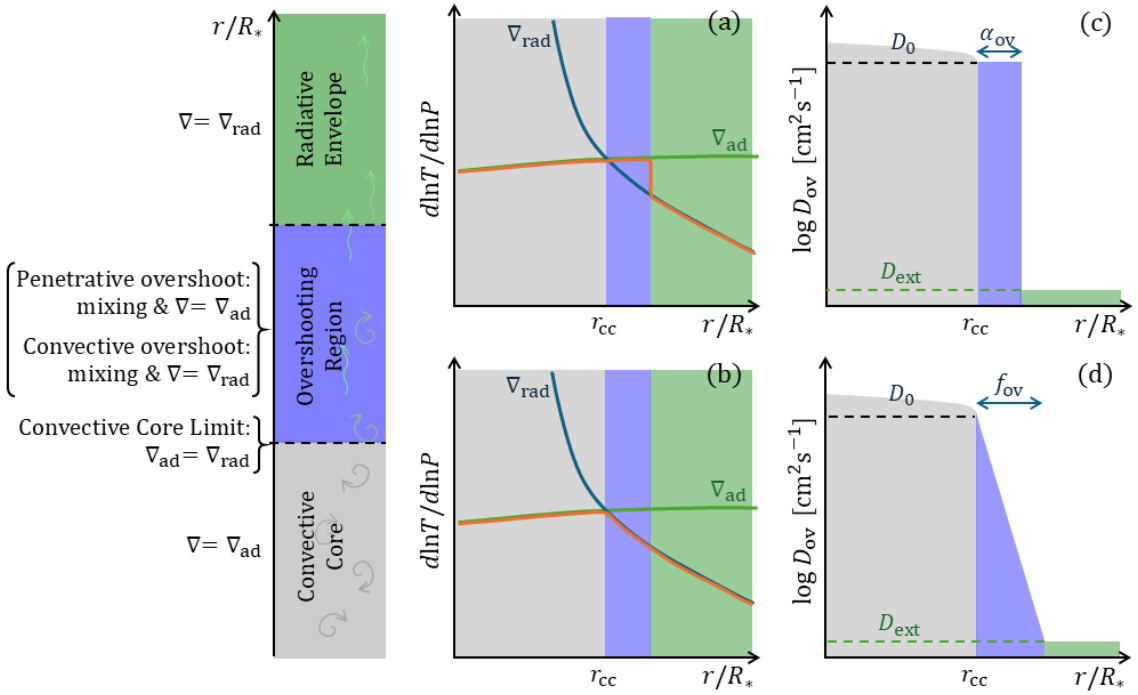


Figure 1.2: Illustration of the internal structure of a solar-like star with a convective core, a convective overshoot region, and different convective overshoot prescriptions applied to the convective core boundary of these MS solar-type stars. Plots adapted from Anders and Pedersen (2023).
(Left) Internal structure of a solar-like star with a convective core (where $\nabla = \nabla_{ad}$; grey shade), an overshooting region (blue shade), and a radiative envelope (where $\nabla = \nabla_{rad}$; green shade) as a function of the fractional radius (r/R_*). The convective core boundary is defined as $\nabla_{ad} = \nabla_{rad}$, according to what was described in the text. The overshooting region is outlined based on the temperature gradient prescriptions described in the text.
(Middle: a,b) Dependence of the temperature gradient (∇) on r/R_*, for the overshooting prescriptions described in the text: (a) penetrative overshoot and (b) convective overshoot. The curves show the evolution of the adiabatic temperature gradient (∇_{ad}, green), the radiative temperature gradient (∇_{rad}, blue) and the adopted temperature gradient in each region (∇, orange).
(Right: c,d) Different shapes of the internal profiles for the diffusion coefficient as a function of r/R_*. Panel (c) presents a step overshoot description, while panel (d) shows a exponential diffusive overshoot prescription. D_0 is a diffusion coefficient measured at the convective core boundary, while D_{ext} accounts for the diffusive mixing in the radiative envelope, a constant typically set to a very small value ($\simeq 0$).

(2018)). MESA adopts the formalism from Freytag et al. (1996), whose profile of the diffusion coefficient,

$$D_{ov} = D_0 . \exp\left(-\frac{2z}{f_{ov} H_P}\right), \text{ for } r > r_0, \tag{1.18}$$

is applied over any distance $z = r - r_0$ beyond r_0 (instead of the convective core boundary r_{cc}). This calibration is necessary because, according to the MLT, both the convective velocity and the mixing coefficient tend to zero at the typical Schwarzschild boundary (r_{cc}). Thus, overshoot begins being applied at $r_0 = r_{cc} - f_{ov} H_{P,0}$, where $D_0 = D_{ov}(r_0)$, f_{ov} is a free dimensionless parameter, and $H_{P,0}$ is the pressure scale height at r_0.

For stars with convective cores (i.e. $M \gtrsim 1.1$ $M_\odot$), convective overshoot can effectively increase the size of a convective core by bringing additional hydrogen into the central burning region, thereby increasing both the MS lifetime and the mass of the He core by the end of the MS.

Examples of how this physical mechanism affects high-mass stars with convective cores are discussed, e.g., in Silva Aguirre et al. (2011) and Anders and Pedersen (2023). Figure 1.3 presents the impact of applying two different prescriptions, one with and one without convective overshoot (dotted and solid lines, respectively), to the evolution of two solar-like stars, with 1.2 $M_\odot$ (red) and 1.5 $M_\odot$ (blue). The results show that models with convective overshoot can have MS lifetimes that are approximately 9% longer, thanks to the additional hydrogen brought in from the stable layers. Furthermore, Silva Aguirre et al. (2011) also shows that convective overshoot can create a smooth chemical profile at the convective border.

Figure 1.4 shows the effect of increasing convective overshoot (assuming exponential diffusive overshoot) in terms of the percentage change in various parameters at the Terminal Age of the Main Sequence (TAMS), for three different initial masses. Comparing the results of a prescription with highly efficient convective overshoot ($f_{\rm ov} = 0.04$) with a prescription with rather inefficient overshoot ($f_{\rm ov} = 0.002$), for TAMS models of a star with 2 $M_\odot$, we find that the efficient overshoot produces effective temperatures that are approximately 17% lower, luminosities that are about 11% higher, ages that are roughly 5% higher, and an He-core with a mass that is approximately 75% higher. These results highlight the importance of constraining both the extent and shape of convective overshoot to better understand stars with convective cores.

As mentioned earlier, other overshooting prescriptions have been considered in the literature, such as extended convective penetration (in Pedersen et al. (2018) and Anders and Pedersen (2023)) and turbulent entrainment (in Viallet et al. (2015) and Anders and Pedersen (2023)). However, these prescriptions are not considered suitable for the stars we intend to model, and therefore, they are not discussed here.

Throughout the work of this thesis, we establish the boundaries between convective and radiative zones following the Schwarzschild criterion (Schwarzschild, 1958). This is important because, unlike the Ledoux criterion (Ledoux, 1947), the Schwarzschild criterion does not account for any changes in the molecular weight of the environment (and therefore, does not consider any changes in the chemical gradient, ∇_μ). Depending on the

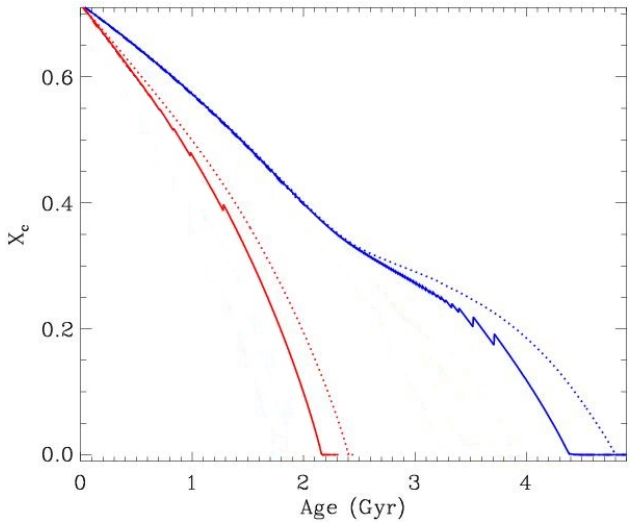


Figure 1.3: Evolution of the hydrogen content at the stellar centre (X_c) for MS models with masses $M = 1.2$ $M_\odot$ (blue) and $M = 1.5$ $M_\odot$ (red). Two prescriptions were considered for each model star: Schwarzschild criterion without overshoot (solid lines) and models with convective overshooting (dotted lines). Plot from Silva Aguirre et al. (2011).

chosen criterion, the position of the convective core boundary may differ, which can lead to the appearance of regions where convection serves as the primary energy transport process when the Schwarzschild criterion is used, but where radiative transport prevails if the Ledoux criterion is applied. These regions are known as semiconvective regions.

In these regions, the amount of mixing, described by a free parameter α_{sc}, is crucial, as efficient mixing can sufficiently reduce the molecular weight gradient to trigger convective instabilities. In other words, applying semiconvection to models that use the Ledoux criterion might be enough to replicate models that use the Schwarzschild criterion. The implementation of the Ledoux criterion for convection (with no mixing beyond the formal boundaries) produces the smallest convective cores (as shown in Figure 1.5) and, consequently, the shortest MS lifetimes, for any given stellar mass and composition. A time-dependent diffusive mixing in the semiconvective region can increase the amount of hydrogen in the core, allowing the convective core to reach the same size as the one determined by the Schwarzschild criterion, provided the mixing efficiency is sufficiently high. However, such physics will not be considered in our models, and therefore, no further discussion will be made here*.

*For a more in-depth discussion of this topic, see Silva Aguirre et al. (2011) and Kippenhahn et al. (2013), Chapter 30.4.

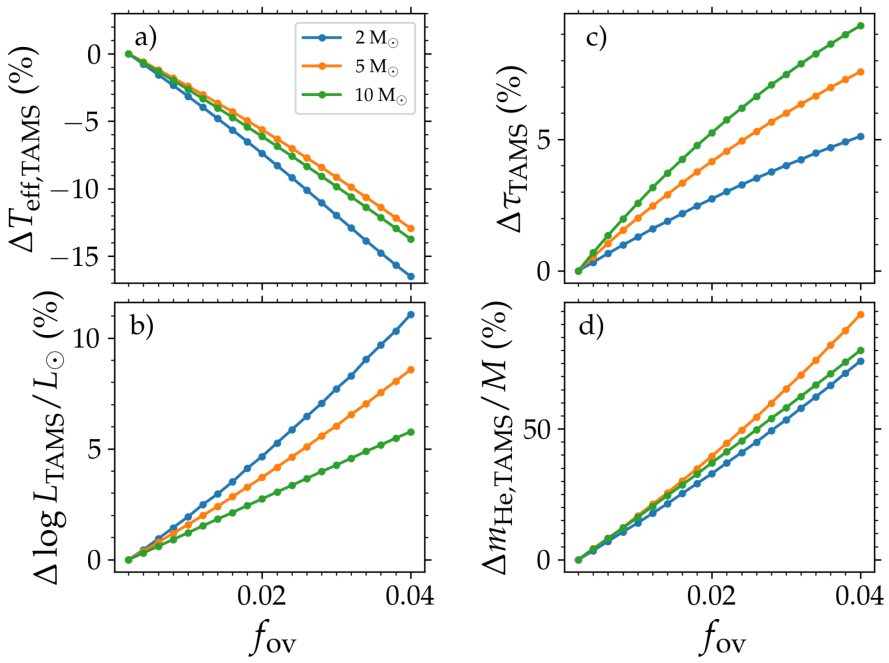


Figure 1.4: Impact of increasing the size of the convective overshoot region (assuming an exponential diffusive overshoot prescription) on different stellar parameters at the TAMS ((a) effective temperature, $T_{\rm eff,TAMS}$; (b) luminosity, $\log L_{\rm TAMS}$; (c) age, $\tau_{\rm TAMS}$; and (d) helium core mass, $m_{\rm He,TAMS}$), for models of three initial masses (M = 2, 5, 10 $M_\odot$). Each panel presents the percentage changes at the TAMS, relative to the $f_{\rm ov} = 0.002$ case. Plot from Anders and Pedersen (2023).

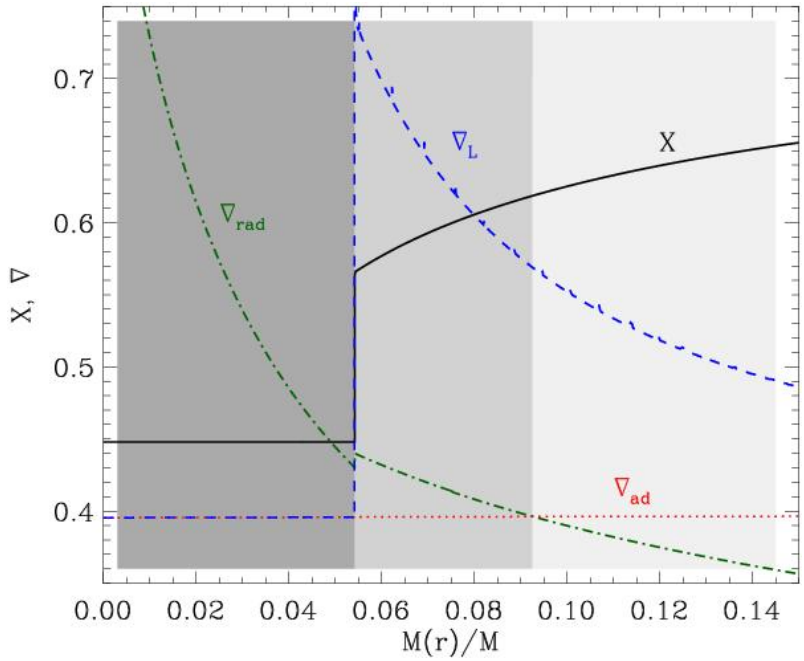


Figure 1.5: Internal structure of a 1.5 $M_\odot$ stellar MS model. The hydrogen abundance (X, black solid line), the adiabatic gradient ($\nabla_{\rm ad}$, red dotted line), the radiative gradient ($\nabla_{\rm rad}$, green dash-dotted line), and the Ledoux gradient ($\nabla_{\rm L} = \nabla_{\rm ad} + \nabla_\mu$, for a perfect gas, blue dashed line) are shown as functions of the mass fraction. From left to right, different grays correspond to regions of different energy transport processes: convective zone, semiconvective zone, and radiative zone. Plot from Silva Aguirre et al. (2011).

1.3. Stellar Evolution of Low-Mass Stars in a Nutshell

In this Section, we explore the evolutionary phases of low-mass stars, specifically those with masses between 0.7 and 2.0 $M_\odot$, and a chemical composition similar to that of the Sun, with focus on the main sequence and subgiant phases, as these are of primary interest to the thesis.

The structure, dynamics, evolution and the final fate of a star depend primarily on its initial mass and initial chemical composition - properties that are related to the location and time of a star's formation, as well as to possible interactions with the surrounding environment during its evolution. For a solar-like star, its expected evolution through the HR diagram is represented in Figure 1.6.

The main sequence results from sustained nuclear fusion reactions happening in the stellar core, where the conversion of hydrogen into helium generates the energy required to maintain hydrostatic equilibrium within the star. This phase is governed by the nuclear timescale,

$$\tau_H = E_H / L \propto M / L, \tag{1.19}$$

where E_H is the total energy that can be released from H-burning, which is intrinsically dependent on the stellar mass M. The nuclear timescale for a star like the Sun is on the order of 10^{10} years, rendering the MS the longest of the evolutionary phases*, and explaining why approximately 80-90% of stars in the solar neighbourhood are observed in this stage.

As discussed at the end of Section 1.2.2, stars of varying masses exhibit not only distinct internal structures, but also different efficiencies in the H-burning reaction networks operating in their cores. In stars with $M \lesssim 1.1\ M_\odot$, which typically possess radiative cores, energy generation is dominated by the proton-proton (pp) chain reactions, owing to their weaker dependence on temperature. Conversely, in stars with $M \gtrsim 1.1\ M_\odot$, the higher temperatures and densities at the core induce the activation of the carbon-nitrogen-oxygen (CNO) cycle. This enhanced energy production leads to the development of a convective core, driven by the substantial energy flux.

The above is illustrated in the left plots (corresponding to the MS phase) of Figures 1.7 (for the 1.1 $M_\odot$) and 1.8 (for the 1.2 $M_\odot$), where the blue regions trace the evolution of convective zones and the red regions highlight the stellar layers contributing to energy

*Later stages of evolution proceed faster, ruled by other more appropriate timescales.

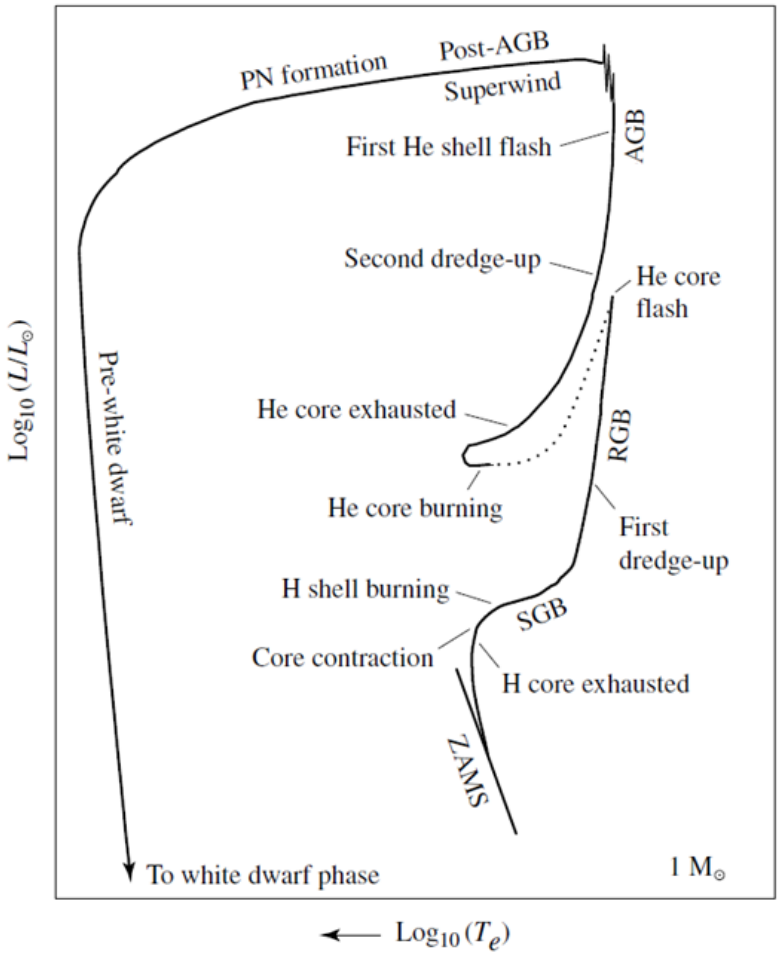


Figure 1.6: Schematic diagram of the evolution of a one solar-mass star, from the Zero Age Main Sequence (ZAMS) to the formation of a white dwarf. The dotted phase of evolution represents the rapid evolution following the helium core flash. Various phases of evolution are labelled as follows: Subgiant Branch (SGB), Red Giant Branch (RGB), Asymptotic Giant Branch (AGB), and Planetary Nebula formation (PN formation). Figure from Carroll and Ostlie (2017).

production, with the degree of transparency indicating the relative intensity of energy generation as a function of radius. Initially, the energy generation rate peaks at the centre, where the temperature is the highest and the hydrogen abundance is nearly homogeneous near the core. As stellar evolution progresses, the central temperature continues to rise, but the hydrogen abundance decreases due to ongoing fusion. Consequently, the location of maximum energy production gradually shifts slightly outward from the centre. This phenomenon accounts for the near-transparency of the central regions ($r \simeq 0$) in Figures 1.7 and 1.8.

Figure 1.9 illustrates the evolution of several stellar parameters throughout the MS phase (highlighted in blue). For a solar-type star, the luminosity L, radius R, effective temperature T_{eff}, and central density ρ_c increase progressively from the ZAMS to the TAMS, as shown in Figures 1.9a-c. Due to the nuclear fusion processes, the mean molecular weight

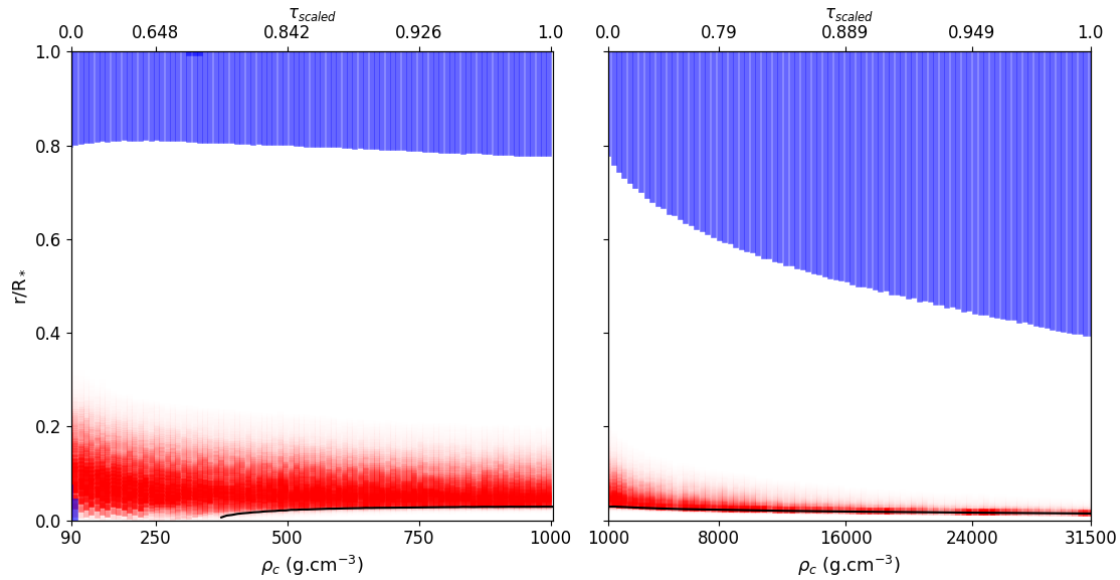


Figure 1.7: Evolution of the internal structure of a model star with M =1.10 $M_\odot$, as a function of the ρ_c (bottom x-axis) and τ_{scaled}, an age parameter defined as the fraction of time elapsed within each evolutionary phase (top x-axis). The structure is displayed in terms of the fractional stellar radius r/R_* (y-axis), during its MS (left panel) and SG (right panel) phases. The blue regions show the evolution of the convective zones inside the star - identified as regions where $\nabla < \nabla_{rad}$. The red regions indicate the parts of the star that contribute to energy production, with the degree of transparency reflecting the intensity of energy generation at a given radius. A black line marks the radius of the helium core - defined as the region when the central helium abundance (Y_c) exceeds 0.95.

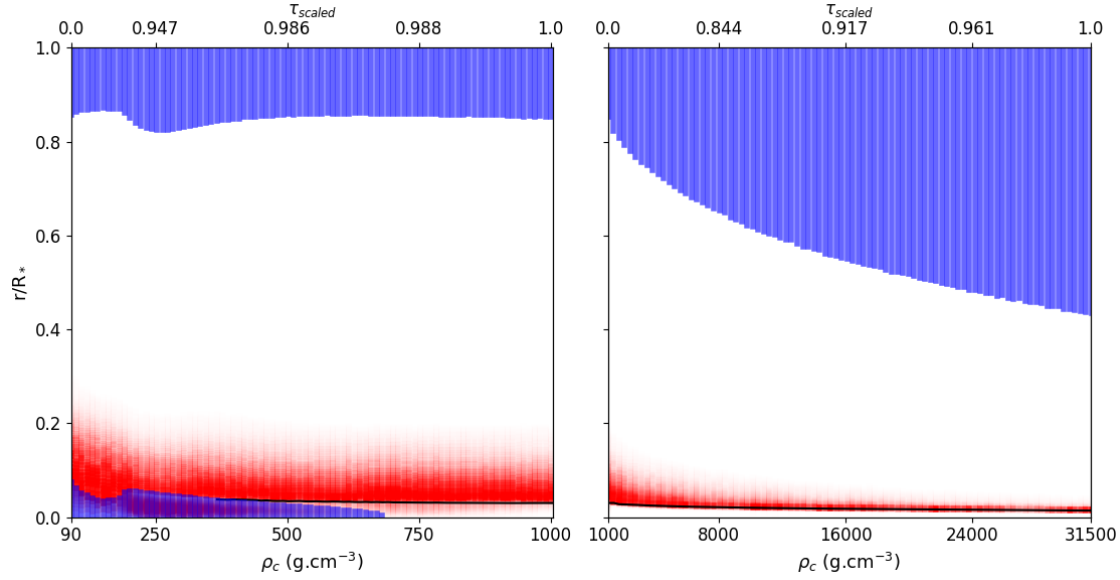


Figure 1.8: Similar to Figure 1.7, for a model star with M =1.20 $M_\odot$.

in the core, μ_c increases as the chemical composition changes. According to the ideal gas law, $P \propto \rho T/\mu$, maintaining the pressure balance in the core requires both T_c and ρ_c to increase. This gradual increase leads to the compression of the stellar core, and

accelerates nuclear burning, leading to a greater energy output required to support the overlying layers.

When the central density increases, gravitational potential energy is released and, as required by the Virial theorem, half of the energy will be radiated away and the other half will go into increasing the temperature of the gas. As a consequence, the stellar region that is sufficiently hot to sustain nuclear reactions will expand slightly during the MS. Moreover, the rising temperature and density more than compensate for the declining hydrogen mass fraction (as shown in Figure 1.9d), leading to a gradual increase in the stellar luminosity, along with its radius and T_{eff}. For the 1.1 $M_\odot$ and a 1.2 $M_\odot$ stellar models, the TAMS is reached after approximately 6.18 and 4.17 Gyr, respectively, roughly when the central hydrogen content drops below $X_c \simeq 0.001$. Beyond this point, the star transitions into the subgiant phase.

For stars that possess a convective core during their MS (i.e. $M \gtrsim 1.1$ $M_\odot$), the transition into the subgiant phase is marked by a characteristic hook-like feature in the star's trajectory on the HR diagram - as observed in Figure 1.9a for the 1.2 $M_\odot$ model. This feature results from an overall contraction of the star occurring on a Kelvin-Helmholtz timescale - the time it would take for a star to radiate away its total kinetic energy at its current luminosity, according to the equation

$$\tau_{\text{KH}} = \frac{GM^2}{2LR}, \tag{1.20}$$

- during which gravitational potential energy is released. This release causes the stellar radius to decrease, and both the luminosity and T_{eff} to increase. Eventually, the temperature just outside the He-core becomes sufficiently high to ignite hydrogen in a thin shell surrounding the core. Due to the rapid onset of shell burning, the overlying envelope is forced to expand slightly, absorbing some of the energy released by the shell, and marking the beginning of the subgiant phase, during which the T_{eff} rapidly decrease.

During the SG phase, the energy produced by the H-burning shell becomes quite intense, substantially exceeding what was produced by the core during the MS. This increase happens because such a thin shell of H-burning (displayed in the right plots of Figures 1.7 and 1.8) has to generate enough energy to counteract the gravitational collapse of the overlying envelope. As the shell continues to consume the available hydrogen, the He-core gradually grows in mass while approaching a nearly isothermal state. The absence

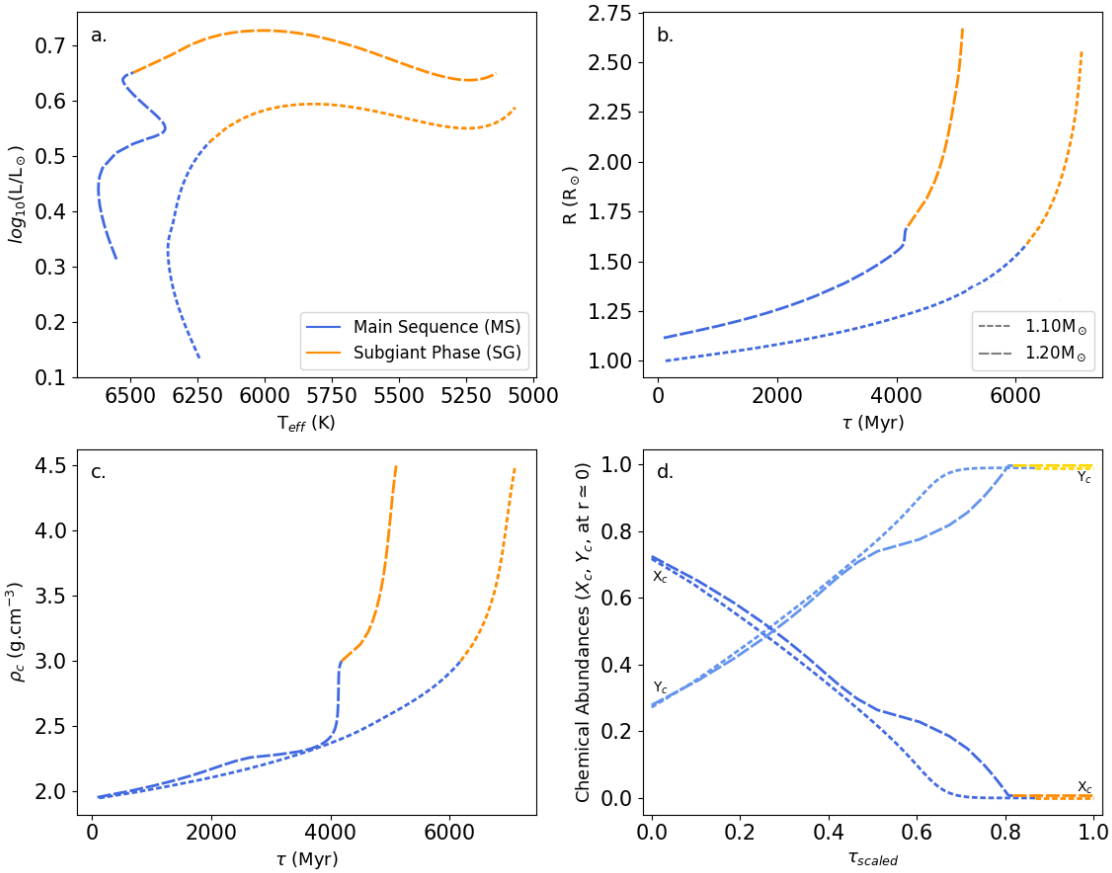


Figure 1.9: Evolution of various stellar parameters for stellar models with 1.1 $M_\odot$ (short-dashed lines) and 1.2 $M_\odot$ (long-dashed lines), both with initial [Fe/H] = -0.1 dex, during their MS (blue) and SG (orange) phases. (a) Evolution of the effective temperature, $T_{\rm eff}$, and luminosity, $\log_{10}(L/L_\odot)$, along the MS and SG evolutionary tracks. (b) Evolution of stellar radius, R, as a function of stellar age, τ. (c) Evolution of central density, $\rho_{\rm c}$, as a function of stellar age, τ. (d) Evolution of the central hydrogen and helium mass fractions ($X_{\rm c}$, $Y_{\rm c}$) as a function of a scaled age parameter, $\tau_{\rm scaled}$, defined as the fraction of time elapsed between the ZAMS and the Terminal Age of the SubGiant phase (TASG).

of energy generation to sustain hydrostatic equilibrium in the core leads to its rapid contraction, which causes the evolution along the SG phase to proceed on the KH timescale. This contraction is seen in Figure 1.9c, where $\rho_{\rm c}$ increases approximately a factor of 1.5 over the short period of the subgiant lifetime. Concurrently, the energy output from the H-burning shell combined with the gravitational energy released by the contracting core causes the stellar envelope to expand and $T_{\rm eff}$ to decrease, as illustrated in Figure 1.9.

For lower-mass stars (within the mass range relevant to this thesis), the cooling of the outer layers leads to the development of a large convective envelope, marking the beginning of the red giant phase. From this point onwards, solar-like stars ascend the red giant branch, increasing in luminosity until He-burning is triggered in the stellar core. Following

the RG phase, low-mass stars enter more complex stages of evolution that involve recurrent readjustments of its internal structure and dynamics, which eventually lead to the loss of the stellar outer layers and the formation of a white dwarf - as illustrated in Figure 1.6. This remnant represents the final stage for most solar-like stars: a carbon-oxygen core that cools over time and gradually crystallizes into a dense, Earth-sized contaminated diamond (Kippenhahn et al., 2013).

1.4. Theory of Stellar Pulsations

The study of the internal structure of stars through their intrinsic global oscillations has substantially contributed to improving our understanding of stellar structure, dynamics, and evolution. Asteroseismology constitutes a unique tool for analysing the resonant oscillations observed in stellar spectra and to understand how they are associated with key stellar properties such as density, temperature, gas motions, and chemical composition, thereby providing insights unattainable through traditional observational methods.

Thanks to a solid theoretical understanding of the phenomena of stellar pulsations and the availability of high-quality data from space missions such as CoRoT, *Kepler*, and TESS, the theory of stellar pulsations has significantly enhanced our understanding of a wide range of stars, from main sequence to red giant stars and white dwarfs. The ultimate goal of stellar pulsations studies is to infer information about the physics and dynamics of stellar interiors from asteroseismic data, typically achieved through forward modelling or inverse techniques, with the former discussed in greater detail in Section 1.5.

In this Section, we briefly review the theoretical foundations for the study of non-radial oscillations, starting with a brief summary of the relevant aspects of hydrodynamics, outlining all the assumptions made during the perturbation and the asymptotic analyses, and characterizing the types of mode oscillations associated with both the main sequence and subgiant phases.

We begin by discussing the theory of stellar pulsations, providing an overview of the linear, adiabatic equations that govern stellar oscillations. These equations allow the determination of stellar oscillation frequencies, which serve as a valuable diagnostic for probing stellar interiors. Most of the content discussed here has been thoroughly examined in the literature, notably by Unno et al. (1989), Aerts et al. (2010), Cunha (2018), and others.

Consider a hydrodynamical system with physical quantities like pressure P, density ρ, temperature T, and velocity $\bar{v}$, each expressed as a function of position $\bar{r}$ and time t. The evolution of these properties can be described by the following set of equations, corresponding respectively to the equation of conservation of mass, the equation of conservation of momentum, the equation of the conservation of energy, and the Poisson equation:

$$\frac{d\rho}{dt} + \rho\nabla\cdot\bar{v} = 0 \tag{1.21}$$

$$\rho\left(\frac{\partial}{\partial t} + \bar{v}\cdot\nabla\right)\bar{v} = -\nabla P - \rho\nabla\phi + \bar{F} \tag{1.22}$$

$$\frac{dq}{dt} = \frac{1}{\rho(\Gamma_3 - 1)}\left(\frac{dP}{dt} - \frac{\Gamma_1 P}{\rho}\frac{d\rho}{dt}\right) \tag{1.23}$$

$$\nabla^2\phi = 4\pi G\rho. \tag{1.24}$$

Here, ϕ denotes the gravitational potential, such that the gravitational acceleration can be written as $\bar{g} = -\nabla\phi$, and $\bar{F}$ represents all external forces besides gravity - such as electromagnetic forces - which can be neglected by setting $\bar{F} = 0$. q represents the heat supplied to the system per unit mass, Γ_1 and Γ_3 are adiabatic exponents defined by the adiabatic derivatives

$$\Gamma_1 = \left(\frac{\partial \ln p}{\partial \ln \rho}\right)_{\text{ad}}, \quad \Gamma_3 - 1 = \left(\frac{\partial \ln T}{\partial \ln \rho}\right)_{\text{ad}}, \tag{1.25}$$

and G is the gravitational constant*.

The properties of the fluid (and its perturbations) can be described both under the Eulerian framework (which corresponds to the perturbation of a physical quantity at a fixed position) and the Lagrangian framework (which follows the time evolution of a physical quantity along its trajectory), which are related to each other according to

$$\frac{df}{dt} = \frac{\partial f}{\partial t} + \nabla f\cdot\frac{d\bar{r}}{dt} \equiv \frac{\partial f}{\partial t} + \bar{v}\cdot\nabla f \tag{1.26}$$

in the case of a scalar property f of the fluid, and

$$\frac{d\bar{F}}{dt} = \frac{\partial \bar{F}}{\partial t} + (\bar{v}\cdot\nabla)\bar{F} \tag{1.27}$$

in the case of a vectorial property $\bar{F}$ of the fluid, where d/dt is the time derivative following the motion (Lagrangian description), and $\partial/\partial t$ is the time derivative at fixed position (Eulerian description).

*Note that the thermodynamic properties T, ρ and P are connected by an equation of state, generally expressed as $\mathcal{F}(T,\rho,P) = 0$. Since we are only considering adiabatic oscillations, the explicit form of the equation of state is not required. A detailed discussion of it can be found in Unno et al. (1989), Chapter 13.4.

In the equilibrium state, the fluid element is assumed to be static, such that both the time derivative and the fluid velocity are zero (i.e. $\partial/\partial t = 0$ and $\bar{v} = 0$). This assumption is justified by the fact that the timescales associated with stellar pulsations are significantly shorter than the evolutionary timescales of the MS and SG stages. For a spherically symmetric star, where the effects of rotation and magnetic fields are neglected, Equation 1.22 reduces to

$$-\nabla P_0 - \rho_0 \nabla \phi_0 = 0, \tag{1.28}$$

which expresses the hydrostatic equilibrium introduced by Equation 1.5 in Section 1.2.

We can now consider perturbations to the equilibrium state (Equations 1.21 to 1.24), assuming these to be small, linear (i.e. second-order or higher terms can be neglected) and adiabatic (i.e., no heat exchange occurs within the fluid during the perturbation) in the deep interior. Accordingly, the Eulerian (f') and the Lagrangian (δf) perturbations to the fluid allow us to express small perturbations as $f = f_0 + f'$ and $\delta f = f' + \bar{\xi} \cdot \nabla f_0$, where $\bar{\xi} \equiv \bar{r} - \bar{r_0}$ is the displacement vector, and $\bar{v} = \frac{d\bar{\xi}}{dt} \simeq \frac{\partial \bar{\xi}}{\partial t}$ is the fluid velocity.

Under these considerations, the system of perturbed equations imposed on a spherically symmetric star is given by

$$\rho' + \nabla \cdot (\rho_0 \bar{\xi}) = 0 \tag{1.29}$$

$$\rho_0 \frac{\partial^2 \bar{\xi}}{\partial t^2} = -\nabla P' - \rho_0 \nabla \phi' - \rho' \nabla \phi_0 \tag{1.30}$$

$$P' + \bar{\xi} \cdot \nabla P_0 = \frac{\Gamma_{1,0} P_0}{\rho_0} \left(\rho' + \bar{\xi} \cdot \nabla \rho_0 \right) \tag{1.31}$$

$$\nabla^2 \phi' = 4\pi G \rho', \tag{1.32}$$

which can be solved with appropriate boundary conditions.

It can be proved, by substitution, that the system of Equations 1.29 to 1.32 admits solutions of the form

$$\begin{aligned} f'(r,\theta,\varphi,t) &= \mathcal{R}\rceil \left[f'(r) Y_\ell^m(\theta,\varphi) e^{-i\omega t} \right] \\ \bar{\xi}(r,\theta,\varphi,t) &= \mathcal{R}\rceil \left[\left(\xi_r(r) Y_l^m(\theta,\varphi) \hat{e}_r + \xi_h(r) \left(\frac{\partial Y_\ell^m}{\partial \theta} \hat{e}_\theta + \frac{1}{\sin\theta} \frac{\partial Y_\ell^m}{\partial \varphi} \hat{e}_\varphi \right) \right) e^{-i\omega t} \right], \end{aligned} \tag{1.33}$$

where $e^{-i\omega t}$ expresses the time dependence of the solution (where ω is real as long as the boundary conditions are fully reflective, i.e. no energy is lost through the boundary), and ξ_r and ξ_h represent the radial and horizontal components of the displacement vector $\bar{\xi}$ in spherical coordinates (r, θ, φ). The angular dependence of these solutions is given

by the spherical harmonics, $Y_\ell^m(\theta,\varphi)$, which are proportional to the associated Legendre functions:

$$Y_\ell^m(\theta,\varphi) \propto P_\ell^m(\cos\theta)e^{im\varphi}. \tag{1.34}$$

The spherical harmonics are characterized by two indices: the angular degree ℓ, that describes the variation of physical quantities with co-latitude θ, and the azimuthal order m, which determines their variation with longitude, φ*.

Using the solutions from Equations 1.33 in the system of Equations 1.29 to 1.32, we find that the radial-dependent amplitudes P', ϕ', and ξ_r obey the following system†

$$\frac{1}{r^2}\frac{d}{dr}(r^2\xi_r) - \frac{g_0}{c_0}\xi_r - \left(\frac{S_l^2}{\omega^2}-1\right)\frac{P'}{c_0^2\rho_0} - \frac{l(l+1)}{r^2\omega^2}\phi' = 0 \tag{1.35}$$

$$\frac{dP'}{dr} + \frac{g_0}{c_0^2}P' - \rho_0(\omega^2 - N_0^2)\xi_r + \rho_0\frac{d\phi'}{dr} = 0 \tag{1.36}$$

$$\frac{1}{r^2}\frac{d}{dr}\left(r^2\frac{d\phi'}{dr}\right) - \frac{l(l+1)}{r^2}\phi' = 4\pi G\left(\frac{P'}{c_0^2} + \frac{\rho_0 N_0^2}{g_0}\xi_r\right), \tag{1.37}$$

where c^2 is the local sound speed, defined as

$$c^2 \equiv \frac{dP}{d\rho} = \frac{\Gamma_1 P}{\rho}, \tag{1.38}$$

S_l is the Lamb frequency, and N_0 is the Brunt-Väisälä frequency (or buoyancy frequency), defined respectively as

$$S_l^2 = \frac{l(l+1)c_0^2}{r^2}, \quad N_0^2 = g_0\left(\frac{1}{\Gamma_{1,0}}\frac{d\ln P_0}{dr} - \frac{d\ln\rho_0}{dr}\right). \tag{1.39}$$

These frequencies will be key for the interpretation of propagation diagrams in Sections 1.4.1 and 1.4.2.

Subjecting the system of Equations 1.35 to 1.37 to appropriate boundary conditions‡ results in an eigenvalue problem that yields solutions at discrete eigenvalues $\omega(n,\ell,m)$. Since these solutions are degenerate in m for the case of spherical symmetry considered here, they are characterized by the mode degree ℓ and the radial order n only. The absolute value of the latter is related to the radial dependence of the solutions, in particular,

*Since we are assuming spherical symmetry for the equilibrium state, with the effects of rotation and magnetic fields being neglected, the equations describing the radial dependence of the variables are independent of the azimuthal order m (as seen in Equations 1.35-1.37).

†The derivation proceeds accordingly to the methodology presented in Sections 13.2 and 13.3 of Unno et al. (1989).

‡Boundary conditions are discussed in detail in Chapter 14 of Unno et al. (1989) and in Section 2.4 of Cunha (2018).

to the number of nodes along the radial direction. From here onwards, when using the radial order n, we shall be referring to its absolute value.

Under the Cowling approximation, which assumes that the gravitational potential perturbation can be neglected (i.e. $\phi' = 0$), particularly for modes with large mode degree ℓ or large radial order n, the system of Equations 1.35 to 1.37 can be reduced to

$$\frac{1}{r^2}\frac{d}{dr}(r^2\xi_r) - \frac{g_0}{c_0^2}\xi_r - \left(\frac{S_l^2}{\omega^2} - 1\right)\frac{P'}{c_0^2\rho_0} = 0 \tag{1.40}$$

$$\frac{dP'}{dr} + \frac{g_0}{c_0^2}P' - \rho_0(\omega^2 - N_0^2)\xi_r = 0, \tag{1.41}$$

which reduces the system to two second-order equations in the variables P' and ξ_r.

For oscillations of high radial order, the eigenfunctions vary much more rapidly than the equilibrium quantities, which allows us to neglect such slower-varying terms and write

$$\frac{d\xi_r}{dr} = \left(\frac{S_l^2}{\omega^2} - 1\right)\frac{P'}{c_0^2\rho_0}\,; \qquad \frac{dP'}{dr} = \rho_0(\omega^2 - N_0^2)\xi_r. \tag{1.42}$$

Neglecting slowly-varying equilibrium terms, these can be combined into a single second-order differential equation for ξ_r

$$\frac{d^2\xi_r}{dr^2} = \frac{\omega^2}{c_0^2}\left(1 - \frac{N_0^2}{\omega^2}\right)\left(\frac{S_l^2}{\omega^2} - 1\right)\xi_r \equiv -k_r^2\xi_r\,, \tag{1.43}$$

where

$$k_r^2 = \frac{\omega^2}{c_0^2}\left(1 - \frac{N_0^2}{\omega^2}\right)\left(1 - \frac{S_l^2}{\omega^2}\right) \tag{1.44}$$

is the radial dispersion relation under the assumed conditions, clearly showing that the characteristic frequencies S_ℓ and N play a crucial role in determining the behaviour of the oscillations. Equation 1.43 is a simplified turning point equation describing small adiabatic pulsations, which while useful, disregards the impact of the stratification of the underlying equilibrium, contained in the terms we neglected. More complete derivations of a similar wave equation, including the neglected terms, can be found, e.g., in Unno et al. (1989) and Gough (1993).

1.4.1 Asteroseismology of MS Solar-Like Oscillators

The stars of interest to this thesis are solar-like oscillators, whose stellar oscillations are driven by the stochastic motions of near-surface convection (cf. Section 1.1). We discuss

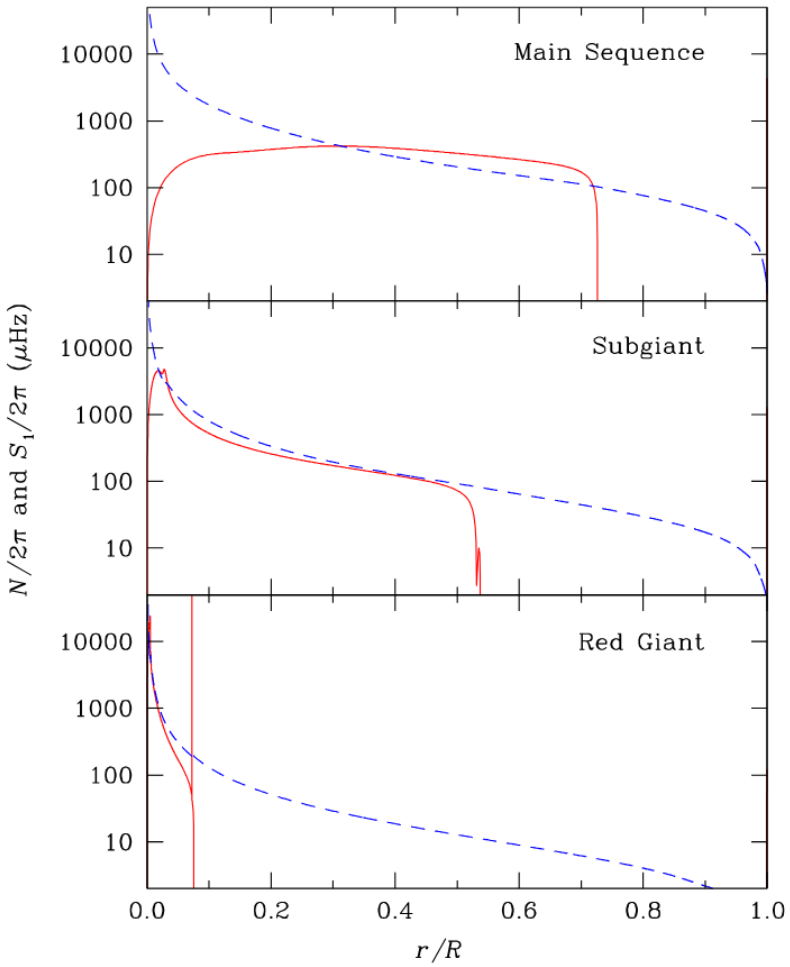


Figure 1.10: Typical propagation diagrams for models of a 1 $M_\odot$ star in the main sequence (top panel), subgiant (middle panel), and red-giant (bottom panel) phases. The Brunt-Väisälä frequency (N; solid red line) and the Lamb frequency (S_ℓ; dashed blue line) are both shown as a function of the fractional radius (r/R). The Brunt–Väisälä frequency defines the g-mode cavity, while the Lamb frequency defines the inner edge of the p-mode cavity. Plot adapted from Hekker and Mazumdar (2014).

the asteroseismic properties during their main sequence in this section and during the subgiant phase in the next section, as these are the primary focus of our work.

Below we examine the main types of waves propagating within the stellar interior. Consider the approximate local radial wave number, k_r, presented in Equation 1.44. When $k_r^2 > 0$, the solution is locally wave-like (i.e. oscillatory in the radial direction), and a mode is said to be oscillatory. However, when $k_r^2 < 0$, the solution is locally exponential, and the mode is said to be evanescent. An oscillatory region in between two evanescent regions is usually called a mode propagating cavity. Modes can be trapped within a single or multiple cavities. Any solutions where $k_r^2 = 0$ indicate radial turning points, which delineate the edges of the different propagation cavities.

An inspection of a propagation diagram like the one on the top panel of Figure 1.10

points towards the existence of two families of solutions: one at lower frequencies, where $\omega^2 < N_0^2, S_\ell^2$ and the mode cavity is essentially determined by the buoyancy frequency; and another at higher frequencies, where $\omega^2 > N_0^2, S_\ell^2$. In the latter case, the propagation cavity is determined by the Lamb frequency in the deeper regions and the critical frequency near the surface. The critical frequency, not apparent in Equation 1.44 (or Figure 1.10) - because it was neglected in the process of its derivation - is associated with the short scale variation of the equilibrium structure near the surface of the star.

In the case of $k_r^2 > 0$ and $\omega^2 \gg N_0^2$,

$$k_r^2 \sim \frac{\omega^2}{c_0^2} - \frac{\ell(\ell+1)}{r^2}, \tag{1.45}$$

which results in the dispersion relation

$$\omega^2 \approx c_0^2(k_r^2 + k_h^2), \quad \text{where } k_h^2 \sim \frac{\ell(\ell+1)}{r^2}, \tag{1.46}$$

characteristic of the acoustic waves (commonly referred to as p-modes). These modes are sustained by the gradient of pressure perturbation, and are predominantly sensitive to the conditions in the outer layers of the star. Their propagation cavities are located between the surface and an inner turning point whose depth strongly depends on the mode degree ℓ. Acoustic modes also exhibit frequencies that increase with both the mode degree ℓ and the radial order n.

In the case of $k_r^2 > 0$ and $\omega^2 \ll S_\ell^2$,

$$k_r^2 \sim \frac{S_\ell^2}{c_0^2\omega^2}(N_0^2 - \omega^2), \tag{1.47}$$

which results in the dispersion relation

$$\omega^2 \approx \frac{N_0^2}{1 + k_r^2/k_h^2}, \tag{1.48}$$

characteristic of the internal gravity waves (also referred to as g-modes). MS solar-like stars may support internal gravity waves maintained by gravity acting on density fluctuations, that is, the buoyancy force acts on fluid displacements to restore the equilibrium of the fluid. Because buoyancy opposes the motion of the fluid elements where $N_0^2 > 0$, i.e. in convectively stable zones, g-modes only propagate where there is no convection. In stars like the Sun, internal gravity waves are essentially confined beneath the convective envelope in a cavity largely independent of the mode degree ℓ, with frequencies always lower than $\max(N_0)$, that increase with mode degree ℓ, and decrease with absolute radial

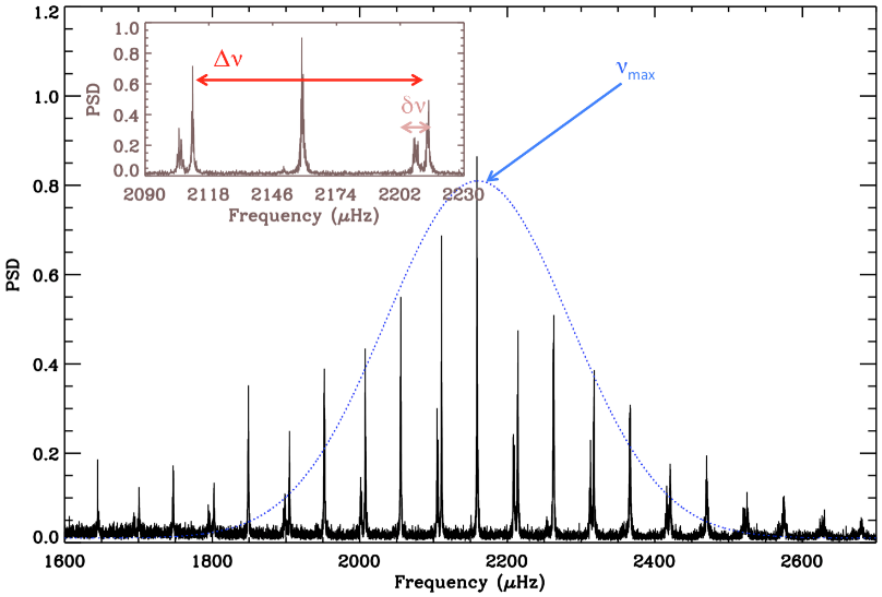


Figure 1.11: Fourier power density spectrum of the MS star *Kepler* target 16 Cyg A. The blue curve shows a Gaussian fit from which we determine the frequency of maximum power, ν_{max}. The inset highlights a selected range of frequencies, illustrating the large frequency separation, $\Delta\nu$, between consecutive $\ell = 0$ modes, as well as the small frequency separation, $\delta\nu_{0,2}$, between adjacent $\ell = 0$ and $\ell = 2$ modes. Figure from García and Ballot (2019).

order n. Nevertheless, despite some claims (García et al. (2010), Fossat et al. (2017)), it remains uncertain whether g-modes have been conclusively detected in the Sun.

In an MS solar-like star, the acoustic oscillation spectrum is similar to the one shown in Figure 1.11. It is composed of a sequence of frequency peaks exhibiting a repetitive pattern structure, whose power is modulated over frequency, and displays an overall characteristic Gaussian shape.

From the smooth Gaussian shape, we estimate the frequency of maximum power (of the p-mode envelope), ν_{max}, (shown in blue in Figure 1.11), which has been shown to scale well with the acoustic cut-off frequency, which, in turn, scales with the surface gravity and the effective temperature as

$$\nu_{\text{max}} \propto g T_{\text{eff}}^{-1/2} \propto M R^{-2} T_{\text{eff}}^{-1/2}. \tag{1.49}$$

From the asymptotic analysis of the second-order pulsation equations under the Cowling approximation, the eigenvalues of high-frequency p-modes are well approximated by

$$\nu_{\ell,n} \approx \Delta\nu \left(n + \frac{\ell}{2} + \epsilon_p \right), \tag{1.50}$$

where

$$\Delta\nu = \left(2\int_0^R \frac{dr}{c}\right)^{-1} \tag{1.51}$$

is the large frequency separation, which can be estimated as the inverse sound travel across a stellar diameter, and ϵ_p is a phase offset. With each frequency peak being identified by a mode degree ℓ and a radial order n, this expression predicts well the repetitive pattern observed in Figure 1.11, with the uniform spacing between frequencies of consecutive modes of the same degree providing an estimate of $\Delta\nu$. It has also been noted that

$$\Delta\nu \propto \sqrt{\bar{\rho}} \propto \sqrt{MR^{-3}}, \tag{1.52}$$

where $\bar{\rho}$ is the mean stellar density.

Considering the asteroseismic parameters ν_{max} and $\Delta\nu$, two scaling relations can be used to estimate the stellar mass and radius, once known the effective temperature, as follows:

$$R \propto \nu_{\text{max}}\Delta\nu^{-2}T_{\text{eff}}^{1/2} \tag{1.53}$$

$$M \propto \nu_{\text{max}}^{3}\Delta\nu^{-4}T_{\text{eff}}^{3/2}. \tag{1.54}$$

The combination of frequencies of modes of consecutive radial orders and degrees differing by two gives the small frequency separation, $\delta\nu$, shown in the inset of Figure 1.11, and defined as

$$\delta\nu_{\ell,n} = \nu_{\ell,n} - \nu_{\ell+2,n-1}. \tag{1.55}$$

This parameter is particularly sensitive to the structure of the innermost layers, due to a dependence on radius (r^{-1}), and to the stellar age.

Finally, in the case of high n, low ℓ g-modes, the first order term of the asymptotic analysis predicts a uniform spacing in mode periods, such that the eigenfrequencies of low-frequency g-modes follow the asymptotic expression

$$\Pi_{\ell,n} \equiv \frac{1}{\nu_{\ell,n}} \simeq \frac{\Pi_0}{\sqrt{l(l+1)}}(n+\epsilon_g), \quad \text{where } \Pi_0 = 2\pi^2\left(\int_{r_1}^{r_2} N\frac{dr}{r}\right)^{-1}, \tag{1.56}$$

and ϵ_g is a phase offset associated with the internal gravity waves.

All of these parameters are of critically importance for asteroseismic studies and for understanding the context and objectives of our work.

1.4.2 Asteroseismology in the SG Phase of Solar-Like Stars

Despite their potential, subgiant stars are not as extensively studied as MS stars or RG stars since they are both less common than MS stars and fainter than RG stars*. However, major advances in their understanding are expected, as subgiants constitute a significant fraction of the asteroseismic targets of TESS and the upcoming PLATO mission.

The properties of the p- and the g- modes discussed previously depend directly on the stellar structure, varying significantly with both stellar mass and evolutionary stage. As a star evolves through the SG phase, an H-burning shell outside the core supplies the star with energy, while its He-core contracts. The buoyancy frequency increases significantly toward the centre, and the star as a whole expands, resulting in a decrease of its mean density. This can be seen in the mid panel of Figure 1.10, where the maximum of the buoyancy frequency in the subgiant has a value comparable to the Lamb frequency in a significant region of the stellar interior. These structural changes cause the maximum frequency of the g-modes (which is limited by the maximum of the buoyancy frequency) to increase, while the frequencies of the p-modes decrease. The potential overlap in frequency leads to mode solutions that have two cavities, one - closer to the stellar centre - where the restoring force is dominated by buoyancy, and another - in the stellar envelope - where the restoring force is dominated by the perturbed pressure gradient. These modes, propagating within two cavities that are coupled through an evanescent region are named mixed-modes.

In terms of the (turning point) wave equation (Equation 1.43), this means that the mode has two separate regions where $k_r^2 > 0$. In such cases, Unno et al. (1989) have shown that the solutions obey an eigenvalue condition that can be expressed as,

$$\cot\left(\int_{r_a}^{r_b} k_r\, dr\right)\tan\left(\int_{r_c}^{r_d} k_r\, dr\right) = \frac{1}{4}\exp\left(-2\int_{r_b}^{r_c}\kappa\, dr\right), \quad \text{where } \kappa^2 \equiv -k_r^2, \tag{1.57}$$

where the g-cavity is located within the stellar fractional radii $[r_a, r_b]$ and the p-cavity is located within the stellar fractional radii $[r_c, r_d]$. The region $[r_b, r_c]$ corresponds to the evanescent region between the two cavities. In a more compact form, this relation becomes

$$\cot\theta_{\mathrm{g}}(\nu)\tan\theta_{\mathrm{p}}(\nu) = q(\nu), \tag{1.58}$$

where θ_g and θ_p are the phase integrals associated with the g- and p-mode cavities, respectively, and q is the coupling strength, a dimensionless coefficient that quantifies the

*Even though SG stars are more observationally accessible than MS stars - due to larger photometric amplitudes and longer dynamical timescales - and more computationally tractable than RGs.

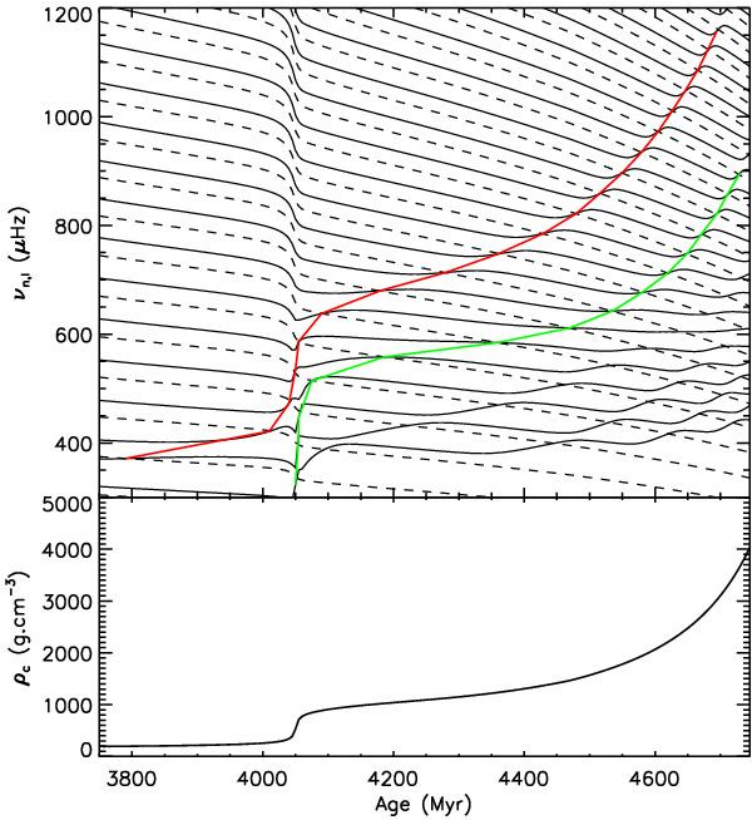


Figure 1.12: Evolution of stellar and asteroseismic properties with age for a 1.3 $M_\odot$ model, during the late MS and SG phases. The top panel shows the evolution of $\ell = 0$ (dashed black lines) and $\ell = 1$ (solid black lines) mode frequencies with age. The frequencies of the first two uncoupled $\ell = 1$ g-modes are also shown: the n_{g_1} mode in red and the n_{g_2} mode in green. The bottom panel shows the evolution of the central density, ρ_c, as a function of age. Plot from Deheuvels and Michel (2011).

strength of the coupling between the p- and g-mode cavities. This equation will be key to the theoretical developments presented in Chapter 4.

In the case of subgiant stars, only a few g-modes (the ones with the highest frequencies*) can couple with the relatively denser set of p-mode oscillations that persist in the convective exterior of the star. The frequencies of the resulting mixed modes shift relative to their uncoupled values (i.e., relative to the frequencies that pure p- or pure g-modes would have), changing smoothly as the star evolves in a manner that preserves the ordering of the complete set of eigenvalues in a continuous fashion throughout this evolution. This process is clearly presented in Figure 1.12 for a solar-like oscillator in its subgiant phase.

In Figure 1.12, we can see the frequency of each pure acoustic radial mode ($\ell = 0$; dashed lines on top panel) decreasing during the subgiant phase. In contrast, the frequencies of dipolar modes ($\ell = 1$, continuous lines on top panel), exhibit a local increase

*The frequency spacing between low-order g-modes is quite large - often several times greater than the large separation of p-modes.

at certain moments in evolution, superimposed on the overall decrease. This evolutionary feature results from near resonances between the p-mode and g-mode pure frequencies and is known as avoided crossing. Away from the avoided crossings, the modes have a p-mode character, showing an evolution similar to the radial modes, while during the avoided crossings they become significantly mixed. Thus, mixed modes are the result of the coupling between modes in the p- and g- mode cavities that are near resonance with each other. They are maintained by gravity acting on density perturbations in the deep interior (with the g-mode character of the mixed mode carrying information about the core region) and by the gradient of pressure perturbations in the outer layers (with the p-mode character allowing the mixed mode to reach the surface, thereby making this information detectable), both of which strongly constrain the stellar structure (Deheuvels and Michel, 2011).

Since mixed-mode frequencies evolve rapidly with age near the avoided crossings, they place very strong, seismic constraints on the structure and fundamental parameters of subgiants, enabling a potential determination of stellar properties with great precision (Li et al., 2019). There have been numerous theoretical studies stating the potential of using the avoided crossings to accurately determine stellar ages during the SG phase, but none has fully considered the challenges they set on model grid interpolation.

1.5. The Challenge of Interpolation for Stellar Modelling

In recent years, the combination of stellar pulsation theory with a vast amount of high-quality asteroseismic data from space missions - such as the Convection, Rotation, and planetary Transits mission (CoRoT; Baglin et al. (2006)), *Kepler* (Gilliland et al. (2010), Koch et al. (2010)), the Transiting Exoplanet Survey Satellite (TESS; Ricker et al. (2015), Campante et al. (2016), Cunha et al. (2019)), and the upcoming PLAnetary Transits and Oscillations of stars mission (PLATO; Rauer et al. (2014), Cunha et al. (2021a), Rauer et al. (2023), Goupil et al. (2024)) - has enabled significant and robust inferences on stellar properties, internal structure and dynamics.

Stellar models are essential for inferring stellar properties, but the task of identifying the model that best fits all observables from a target star is computationally demanding. This process is a non-linear, high-dimensional optimization problem, sensitive to numerous

input parameters that require optimization, such as stellar mass, initial composition, and a variety of mixing parameters*.

Forward modelling techniques are among the preferred methods to simulate stars observed by the mentioned missions and to estimate their global properties. These techniques consider an input model that defines the initial state of the system while assuming a given set of established physics (i.e. the grid inputs and the stellar physics for models, such as diffusion and atmosphere), and predicts its evolution at each time step, generating outputs that can be compared with the actual observations. Traditionally, optimization procedures find the best representation of a star by minimizing the differences between models and observations, based on criteria defined *a priori*†.

To efficiently determine the fundamental properties of a large sample of stars, several fast, stable, and robust optimization algorithms are currently available to the community, such as *Asteroseismic Inference on a Massive Scale* (AIMS; Rendle et al. (2019)), *BAyesian STellar Algorithm* (BASTA; Aguirre Børsen-Koch et al. (2022)), *Stellar Parameters INferred Systematically* (SPInS; Lebreton and Reese (2020)), and PARAM (Rodrigues et al., 2017). These algorithms provide a powerful diagnostic tool for the determination of stellar properties that allow for the determination of a representative set of models that best reproduce a given set of classical and asteroseismic constraints.

When discussing forward modelling techniques, we should distinguish between two main categories. The previously mentioned optimization algorithms fall under the *grid-based* modelling category, which requires access to a pre-computed grid of stellar models spanning a given parameter space to estimate stellar properties. These algorithms then compare the models with observations, while trying to minimize the differences between models and observations, according to criteria defined *a priori*. This approach differs significantly from the so-called *on-the-fly* modelling approach, where the goodness of the fit is calculated while generating the stellar models. In this case, the generated models are

*Typical input physical parameters include stellar mass, M, initial composition - comprising initial hydrogen abundance, X_0, and initial metallicity, Z_0 or [Fe/H], - and a variety of mixing parameters such as the mixing length parameter, $\alpha_{\rm MLT}$, and the convective overshoot parameter, $f_{\rm ov}$. Most of these parameters will be discussed throughout this work.

†Common optimization methods include the Monte Carlo Markov Chain (MCMC) algorithm, and the determination of minimization functions, based on individual χ^2 functions calculated for each observed parameter, P. This χ^2 statistic is typically defined as

$$\chi^2 = \frac{(P_{\rm obs} - P_{\rm model})^2}{\sigma^2_{P_{\rm obs}}}, \tag{1.59}$$

where $\sigma_{P_{\rm obs}}$ represents the uncertainty in the observed parameter.

specific to the target being modelled, with a new set of models being generated each time a different target is considered. A minimization function (typically described by a χ^2-value) is assigned to each profile to determine whether to maintain or discard a model. As a result, we end up with a grid built only with the models most likely to provide useful information. This method also makes the *on-the-fly* modelling approach computationally expensive and less appropriate for a pipeline of an instrument observing a vast number of stars*.

However, there is also a drawback associated with the grid-based method: When increasing the number of parameters of the models, the number of models on the stellar grid involved in the search also increases, exponentially, increasing the required storage and possibly decreasing the computational efficiency. To make stellar model searches more manageable, traditional optimization methods can employ a number of strategies: (i) lowering the model grid resolution, (ii) reducing the number of initial model parameters, and (iii) applying grid interpolation during the optimization process.

We can lower the resolution of the grid by increasing the timestep considered to output the models per each evolutionary track of the grid, resulting in a reduced number of models in the grid. However, this comes at the cost of parameter coverage, potentially leading to suboptimal solutions. Similarly, restricting the search to only a few free input parameters, and using approximations for other initial parameters - such as a solar-calibrated value for the mixing length parameter (α_{MLT}), or the Galactic enrichment relation to estimate the initial helium abundance (Y_0) from the initial metal abundance (Z_0) - we may be led to underestimated uncertainties and a reduction in the precision with which stellar properties are inferred. Additionally, a limiting factor in subgiant model searches is the time-consuming calculation of non-radial modes for evolved stars, which makes it expensive for search methods that require a large grid of models or on-the-fly calculation of stellar tracks.

Grid interpolation methods are another solution employed by optimization codes such as AIMS and BASTA to mitigate the need for a very fine grid of models, which help ensuring that the science requirements of a mission are satisfied. These methods compensate for the lack of resolution in model grids by predicting an approximate description of both the

*We note that despite their differences, these two modelling approaches are not necessarily mutually exclusive, as the result of grid searches may be used to restrict the region of parameter space being considered for the more refined model-on-the-fly analysis.

global and seismic properties of models at points of the parameter space located between the models of the initial pre-computed discrete grid.

When interpolating data on a grid, it is crucial to ensure that the interpolation errors on the model quantities are smaller than the uncertainties on the observations we aim at comparing with. Clearly, this is easier to achieve when the quantities we want to interpolate vary approximately linearly between the models of our grid. In this context, rapid frequency variations, such as those discussed for the mixed modes in Section 1.4.2, pose potential challenges for grid-based modelling and interpolation.

Since the timescale associated with avoided crossings can be several orders of magnitude shorter than the typical nuclear evolution time of low-mass subgiants, reproducing mixed modes with a traditional grid technique requires very fine steps in mass and age. This makes this method prohibitive when the number of free parameters is large, as it requires testing the model physics. Interpolation across tracks could mitigate the need for extremely fine steps in mass, but it needs to be tested for subgiants, especially because of the extreme sensitivity of the g-dominated frequencies to the masses of the models.

The emergence of mixed modes whose frequencies exhibit a fast evolution may result in, for a fixed age, the same mode being more acoustic- or gravity-dominated for different evolutionary tracks. This is shown in the top panel of Figure 1.13, which displays the evolution of the normalized frequency of a dipole mode of radial order $n = 11$ over various mass tracks, highlighting a fixed age value - 4.18 Gyr - with a vertical dashed line. Here the normalized frequency is defined as

$$\nu_{\ell,n,\text{norm}} = \nu_{\ell,n} / \sqrt{GM/R^3}, \tag{1.60}$$

where G is the gravitational constant, M is the stellar mass, and R is the stellar radius of the corresponding model. Because of this difference in the mode evolution at fixed age, when interpolating between different evolutionary tracks, we may be combining a mode that is evolving essentially as if it were acoustic (as in the case of the mass track with 1.23 $M_\odot$) with a mode that is undergoing an avoided crossing (as in the case of the mass track with 1.24 $M_\odot$).

This difference in the mode evolution phase at fixed age is expected to impact the accuracy of the interpolation. One possible way to improve this could be to use proxies of age that better align the avoided crossings of adjacent mass tracks, like central density, ρ_c, as illustrated in Figure 1.13. From the bottom panel, we see that avoided crossings appear

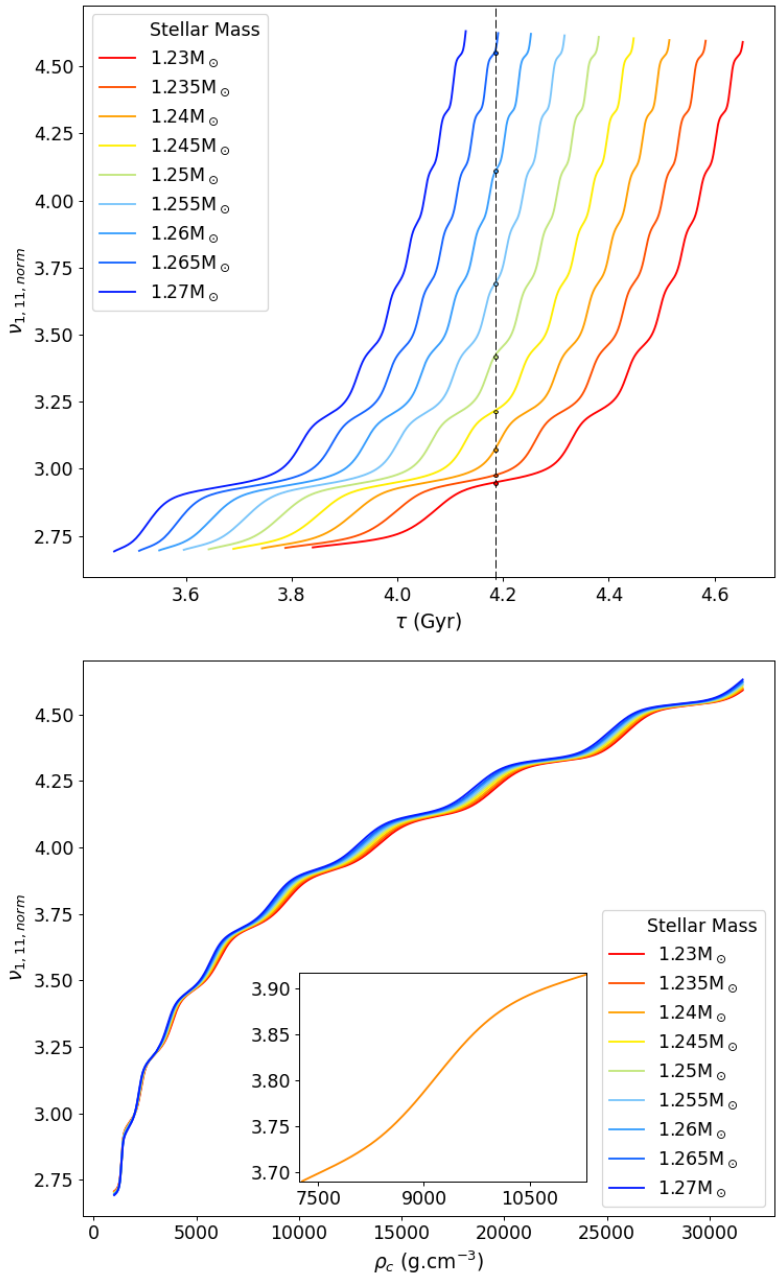


Figure 1.13: Evolution of the normalized frequencies of non-radial $\ell = 1$ modes, with radial order $n = 11$, for evolutionary tracks of a stellar grid (the details of which are provided in Section 2.2) with masses between 1.23 and 1.27 $M_\odot$, as a function of physical age τ (top panel) and central density ρ_c (bottom panel). The points connected by a dashed line in the left panel indicate models at a fixed age of 4.18 Gyr. The right panel displays a subplot highlighting a particular avoided crossing for the mass $M = 1.24$ $M_\odot$.

more closely aligned when displayed as a function of ρ_c.

To understand why ρ_c may be a better age proxy, we consider the evolution of the properties of the stellar core during the SG phase (discussed in Section 1.3). A contracting He-core influences the profile of the local Brunt-Väisälä frequency, causing the frequency

of g-modes to approach that of the p-modes, and giving rise to a forest of avoided crossings. In a fully ionized environment, the Brunt-Väisälä frequency (previously expressed in Equation 1.39) can be written as

$$N^2 = \frac{g\delta}{H_P}\left(\nabla_{ad} - \nabla + \frac{\phi}{\delta}\nabla_\mu\right), \tag{1.61}$$

where g is the local gravitational acceleration inside the star, H_P is the local pressure scale height, ∇_{ad} is the adiabatic gradient, ∇ is the temperature gradient, and ∇_μ is the gradient of the mean molecular weight. In this way, we see that the Brunt-Väisälä frequency carries information about both the thermal structure (the first two terms inside the parentheses) and the compositional structure (the last term) of the star.

Near the centre ($r \to 0$), the local gravity inside the compact radiative subgiant core can be written as $g(r) \sim G\rho_c r$. For an ideal gas in hydrostatic equilibrium, the Brunt-Väisälä frequency then scales as

$$N^2 \sim \frac{g(r)}{H_P} \sim \frac{\rho_c^3}{P_c} r^2 \sim \frac{\rho_c^2 \mu_c}{T_c} r^2. \tag{1.62}$$

In early post-MS models, the central temperature, T_c, and the central mean molecular weight, μ_c, hardly change within the isothermal core, where nuclear reactions are absent. This leaves ρ_c as the main dependency of the Brunt-Väisälä frequency scaling in Equation 1.62. Since ρ_c increases monotonically during the SG phase due to the contraction of the inner regions of the star, it can be considered as an age proxy for interpolation, with potential advantages over the use of physical age. In the following Chapters, we will explore the effectiveness of ρ_c and of other age proxies for improving grid interpolation accuracy during the subgiant phase.

2. Analytical Characterization of the Errors of Classical Interpolation Algorithms

The content of this Chapter is adapted from the work published in Clara et al. (2025), which has been published in *Astronomy & Astrophysics*.

2.1. Introduction

As discussed in Section 1.5, in order to guarantee a given precision in the inferred stellar properties and ensure that the science requirements of a mission like PLATO are met, an optimization algorithm may require combining a grid-based modelling approach with an interpolation scheme. Interpolation algorithms are employed to compensate for the limited resolution of model grids by providing approximate predictions (e.g., the basic and seismic properties) at parameter space points located between the models of the initial pre-computed discrete grid. They are commonly used in optimization codes such as AIMS, BASTA, SPInS, and PARAM, and have been discussed in the works of Rendle et al. (2019), Li et al. (2020) and Aguirre Børsen-Koch et al. (2022), among others.

Rendle et al. (2019) report the results of interpolation tests conducted while fitting observational data with AIMS. The authors compare their findings with the typical uncertainties found in the literature for a main-sequence (MS) target, 16 Cyg A, whose smallest and average uncertainties for $\ell = 0$ modes are 0.04 and 0.08 μHz, respectively, and for a red-giant-branch (RGB) target, KIC 4448777, whose smallest and average uncertainties for $\ell = 0$ modes are 0.014 and 0.018 μHz, respectively. For interpolation along evolutionary tracks, errors for $\ell = 0$ modes were found to be smaller than both the smallest and average uncertainties from literature values, except for a small fraction of RGB tracks (less than 3% of those tested) characterized by low masses and high metallicities. For cross-track interpolation, their root mean square average errors are comparable to their literature reference value of 0.08 μHz.

For BASTA, Aguirre Børsen-Koch et al. (2022) only discuss the results of the complete interpolation procedure (i.e., the errors on interpolation along and across tracks are not considered separately), restricting their analysis to MS stars. Using an interpolation procedure similar to that employed by AIMS, they show that the fractional differences in $\Delta\nu$ between the original and the interpolated track are at the 10^{-4} level, which is an order

of magnitude smaller than the relative uncertainty in $\Delta\nu$ measured for the best *Kepler* targets.

Li et al. (2020) test the interpolation of $\ell = 1,2$ oscillation mode frequencies while examining how seismic stellar ages for 36 *Kepler* subgiants depend on helium abundance (Y), the mixing-length parameter, and metallicity. Using cubic splines interpolation and physical age, τ, as the age proxy, the authors perform interpolation along a mass track with 1.20 $M_\odot$, where the models to be interpolated are separated by time steps of 6×10^6 yr. For $\ell = 1$ modes, the differences between interpolated frequencies and their true values were mostly below $\sim$0.05 μHz, particularly for frequencies in the 0.5-1.5 ν_{max} range. Using the same method, interpolation of $\ell = 2$ mode frequencies was found to work well for p-dominated modes but not for g-dominated ones. For 85% of the tested modes, frequency differences were found to be smaller than 0.2 μHz, but for the remaining poorly fitted g-dominated modes, differences reached 0.5 μHz.

In summary, among the literature on grid-based modelling of solar-like pulsators, only Li et al. (2020) performed interpolation tests on grids of subgiant stars. Yet, even in that case, the work focused exclusively on interpolation along evolutionary tracks. This underscores the absence of a systematic quantification of the accuracy of interpolation algorithms during the subgiant evolutionary phase.

In this Chapter, we characterize classical interpolation algorithms applied to the determination of the pulsation properties in the subgiant phase and discuss the associated problems, establishing which method is capable of most accurately describing model frequencies interpolated both along and across evolutionary tracks of a two-parameter stellar grid. As a reference, we compare the interpolation errors with typical observational errors of $\delta\nu \sim 0.1\mu$Hz (Li et al., 2020), which we set as our accuracy aim.

2.2. Characterization of the Stellar Grid and the Method

We start by describing the grid of stellar models used for our simulation tests and the procedure adopted to characterize the accuracy of linear and higher-order interpolation algorithms.

2.2.1 Input physics of the stellar grid

To perform tests that characterize the quality of interpolation, we compute a mass-age grid of evolutionary tracks in the subgiant phase. To this end, we used Modules for Experiments in Stellar Astrophysics (MESA, version r12778), an open-source stellar evolution package that is undergoing active development (Paxton et al., 2011, 2013, 2015, 2018, 2019). We adopted the solar composition from Asplund et al. (2009), with $(Z/X)_\odot$ = 0.018099, and the OPAL opacity tables given by Grevesse and Sauval (1998), which were supplemented by the low-temperature opacities from Ferguson et al. (2005). We used the nuclear reactions rates obtained from the Joint Institute for Nuclear Astrophysics Reaction Library (JINA REACLIB, Cyburt et al. (2003)) version 2.2, with specific rates for $^{12}\mathrm{C}(\alpha,\gamma)^{16}\mathrm{O}$ (Kunz et al., 2002) and $^{14}\mathrm{N}(p,\gamma)^{15}\mathrm{O}$ (Imbriani et al., 2005). The boundary conditions at the stellar surface were established using the Krishna-Swamy atmosphere (Krishna Swamy, 1966).

Our aim with this work is to test the interpolation across evolutionary tracks of different masses. Even though the ultimate goal is to test interpolation in a full grid varying a number of different parameters, we decided to keep things as simple as possible by fixing all the physical inputs of the grid except for mass. Thus, we fixed metallicity at [Fe/H] = -0.1 dex, and varied the stellar mass between values of 1.150 and 1.350 $M_\odot$, in steps of 0.005 $M_\odot$. The goal was to produce a small but dense grid of stellar models in the subgiant phase, with masses crossing the region where small convective cores develop during the main sequence. The initial helium fraction was determined following the law of Galactic enrichment,

$$Y_\mathrm{i} = Y_0 + \frac{\Delta Y}{\Delta Z} Z_\mathrm{i}, \tag{2.1}$$

where the primordial helium abundance is $Y_0 = 0.2485$, according to Planck Collaboration et al. (2016), and the ratio $\Delta Y/\Delta Z$ is estimated to be 1.36 (Balser, 2006, Nsamba et al., 2021).

The mixing-length parameter (first established in Böhm-Vitense (1958)) is defined by $\alpha_\mathrm{MLT} = \ell_\mathrm{MLT}/H_\mathrm{P}$, where ℓ_MLT is the mixing length, and H_P is the pressure scale height. In MESA, α_MLT is implemented by the `mlt` module for convection, as presented by Cox and Giuli (1968), and, for this grid, was fixed at 1.711. Convective overshooting was implemented via an exponential decay of the convective diffusion coefficient beyond the

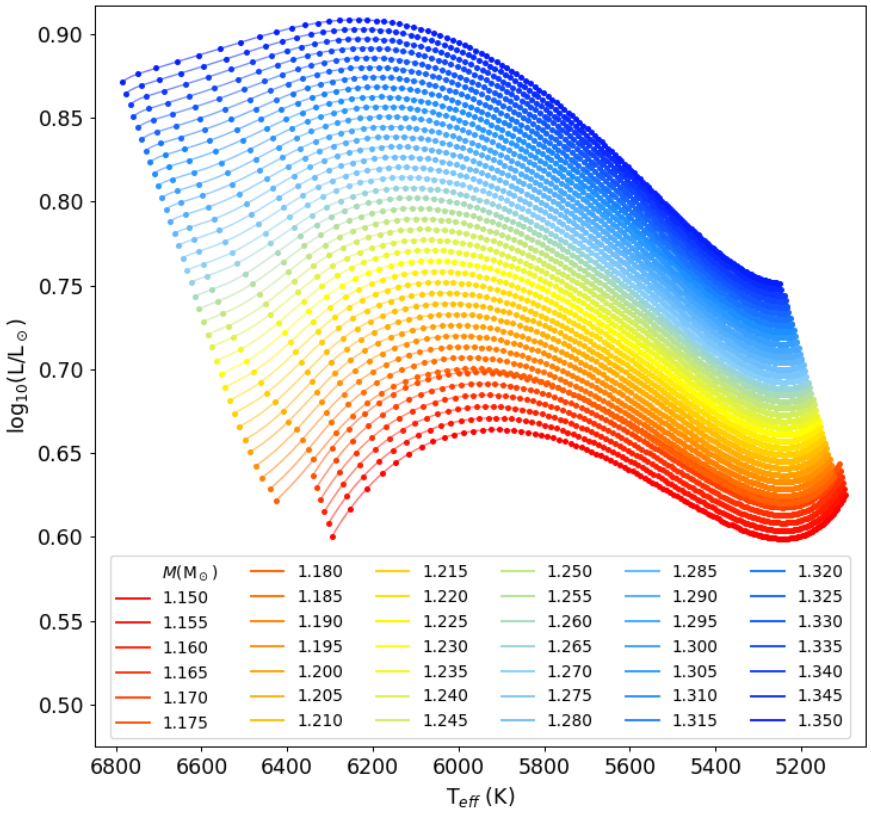


Figure 2.1: Hertzsprung–Russell diagram displaying every tenth model of each of the 41 tracks in the subgiant phase produced for the stellar grid described in the text.

convective boundary, according to Herwig (2000),

$$D_{\text{ov}} = D_{\text{conv},0}.\exp\left(-\frac{2z}{f_{\text{ov}}H_{\text{P}}}\right), \tag{2.2}$$

where $D_{\text{conv},0}$ is the diffusion coefficient at the convective border, z is the distance from the boundary of the convective region, and f_{ov} is a user-adjusted dimensionless parameter set to 0.01. Because the pressure scale height diverges at the centre, the classical implementation can generate unphysically large overshooting regions for small convective cores*. MESA can ensure that overshoot is always limited to a fraction of the convective region's extension through the application of a geometrical cut-off (Paxton et al., 2011), replacing H_{P} in Equation 2.2 with

$$\tilde{H}_{\text{P}} := H_{\text{P}} \cdot \min\left(1, \frac{\Delta R_{\text{cz}}}{H_{\text{P}} \cdot \alpha_{\text{ov}}}\right), \tag{2.3}$$

where ΔR_{cz} is the thickness of the convectively-unstable region, and α_{ov} is by default set to the mixing length parameter. Microscopic diffusion was not included.

*For stars with $M \gtrsim 1.1$ M$_\odot$, the size of the overshoot region can be the same as the core itself.

The stellar models for all evolutionary tracks from the Hayashi line to the bottom of the red-giant branch were computed using MESA, but only the models from the subgiant phase were considered. This stage corresponds to the models computed between the Terminal Age of the Main Sequence (TAMS), defined as when $\log(\rho_c) \simeq 3.0$ g.cm^{-3} (corresponding approximately to the age at which the central hydrogen abundance reaches $X_c = 10^{-4}$ in our grid), and the Terminal Age of the SubGiant phase (TASG), defined as when $\log(\rho_c) \simeq$4.5 g.cm^{-3} (Nsamba et al., 2018). Although unconventional, this ρ_c condition for TAMS allows us to structure the grid with a constant ρ_c-step, starting from models with the same ρ_c value.

Computing a grid of stellar models capable of comprehensively describing oscillation modes in the subgiant phase is time-consuming as mixed modes vary rapidly with age. We programmed MESA to output models at a ρ_c step of approximately 10 g.cm^{-3}, which resulted in a dense grid of 121,424 stellar models distributed over 41 evolutionary tracks, with the number of models per evolutionary track varying between 2959 and 2963. As the models of our stellar grid are equally spaced in central density, the number of models in the later stages of evolution is much larger than the number of models in the earlier stages of evolution. This is evident in Figure 2.1, where we plot one out of every 10 models along evolutionary tracks for illustration purposes. This information is important in order to correctly interpret the results in our figures and tables.

For each model generated by MESA, we used GYRE (Townsend and Teitler, 2013) to compute theoretical stellar oscillation frequencies for modes with ℓ = 0 and 1, by solving the equations of adiabatic stellar pulsations, outputting the frequencies within the frame window determined by

$$[\nu_{\ell,n}] = \nu_{\rm max} \pm 3\sigma_\nu, \text{ where } \sigma_\nu = \frac{0.66\nu_{\rm max}^{0.88}}{2\sqrt{2\log(2)}} \tag{2.4}$$

where $\nu_{\rm max}$ is the frequency of maximum power, and σ_ν is the width of the Gaussian envelope encompassing the distribution of pulsations, as given by Mosser et al. (2012). The normalized mode frequencies determined for this stellar grid are shown in Figure 2.2. Although all $\ell = 0$ modes determined by GYRE within the frame window defined by Equation (2.4) were considered, only positive radial orders of $\ell = 1$ modes were used in the tests. Only non-radial modes of degree $\ell = 1$ were computed, since the objective is to compare the interpolation of pure acoustic modes ($\ell = 0$) with the interpolation of mixed modes, for which $\ell = 1$ modes are the best example as their p-g coupling is maximal.

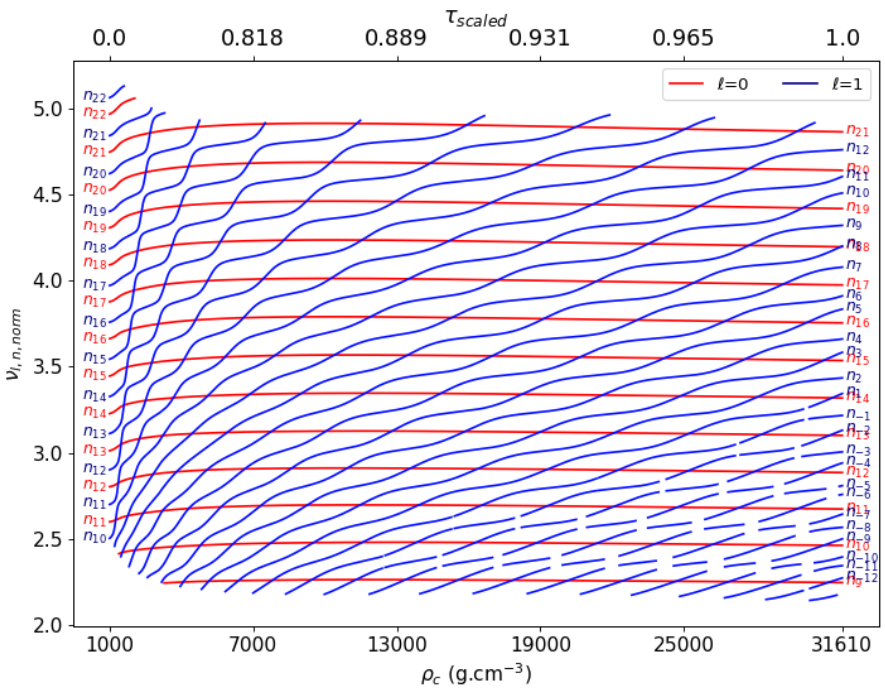


Figure 2.2: Evolution of $\ell = 0$ (red) and 1 (blue) normalized mode frequencies with τ_{scaled} (top) and ρ_c (bottom), for a mass track with 1.245 $M_\odot$. The correspondent radial orders n are indicated at the beginning and end of the evolution.

Finally, as discussed in Section 1.4.1, in order to remove the impact of the evolution-driven change in mean density, we considered normalized frequencies, as defined by Equation 1.60,

$$\nu_{\ell,n,\text{norm}} = \nu_{\ell,n} / \sqrt{GM/R^3}. \tag{2.5}$$

2.2.2 Interpolation methods

A complete interpolation process requires both interpolation along the evolutionary track (i.e., in the age proxy), and across the input parameters of the grid (in this case, mass). Therefore, we considered a series of interpolation methods to explore the regions between stellar models, dividing the procedure in two steps (as shown in Figure 2.3): (i) age interpolation between models within an evolutionary track, considering a certain age proxy, and (ii) track interpolation across different evolutionary tracks (in the mass parameter), for a constant value of the previously chosen age proxy.

For the interpolation procedure, we considered first (linear) and third (cubic) order methods, having used either polynomial or spline interpolation. Polynomial interpolation usually fits an n order function to $n + 1$ points, and is used to interpolate between the middle two. Spline interpolation considers a set of n order functions, each defined between two data points, to build a system of equations, constrained so that the values of the function

and of its first and second derivatives match as one approaches each data point from the left and right. These requirements still leave the system under-constrained, which requires some reasonable assumptions to be made about the values beyond the range of data being fitted, usually an assumption about the second derivative at the two end points. In both cases, the interpolated functions pass through all the existing points of the initial stellar grid. For example, consider an evolutionary track of a given mass M and a mode of a given radial order n (or similarly, consider a fixed value for a given age proxy τ and a mode of a given radial order n). Between every two models (x_1, x_2) on that evolutionary track (or at a fixed age proxy), we can linearly interpolate the frequencies to any point x within that interval by computing

$$f(x) = \frac{(x_2 - x)y_1 + (x - x_1)y_2}{x_2 - x_1} \tag{2.6}$$

where y_1 and y_2 are the mode frequencies of radial order n in the models x_1 and x_2, respectively.

In the case of cubic splines, interpolation is accomplished using the function

$$f(x) = \begin{cases} a_1x^3 + b_1x^2 + c_1x + d_1, \text{ if } x \in [x_1, x_2] \\ a_2x^3 + b_2x^2 + c_2x + d_2, \text{ if } x \in]x_2, x_3] \\ \ldots \\ a_kx^3 + b_kx^2 + c_kx + d_k, \text{ if } x \in]x_k, x_{k+1}] \end{cases} \tag{2.7}$$

where each group of the 4 coefficients (a_k, b_k, c_k, d_k), that define a segment $]x_k, x_{k+1}]$ of the resulting function, is obtained by solving the system of equations

$$\begin{cases} a_kx_k^3 + b_kx_k^2 + c_kx_k + d_k = y_k \\ a_kx_{k+1}^3 + b_kx_{k+1}^2 + c_kx_{k+1} + d_k = y_{k+1} \\ \frac{\mathrm{d}}{\mathrm{d}x}f_{k-1}(x_k) = \frac{\mathrm{d}}{\mathrm{d}x}f_k(x_k) \\ \frac{\mathrm{d}^2}{\mathrm{d}x^2}f_{k-1}(x_k) = \frac{\mathrm{d}^2}{\mathrm{d}x^2}f_k(x_k) \\ \text{+ boundary conditions.} \end{cases} \tag{2.8}$$

We note that each polynomial from Equation (2.7) is valid within the respective intervals only. For interpolation in Python, we used the library package `scipy.interpolate.interp1d()`, while considering its default conditions. This includes boundary conditions established by a 'not-a-knot' condition, i.e., the first and the last two polynomials' third derivatives are equal in the point where they touch each other.



Figure 2.3: Schematic of the 2-step interpolation procedure. Frequencies from known models (black dots) are used to estimate the frequencies of models at specific age proxy values (white dots) along a particular track M_i - interpolation along tracks. These estimated frequencies are then used to interpolate across the evolutionary tracks of masses M_i, for a specific age proxy value and fixed ℓ, n (red dot) - interpolation across evolutionary tracks.

For each choice of the interpolation method, we can consider different age proxies for interpolation. Here we consider three options, namely, physical age, τ; scaled age, τ_{scaled}; and central density, ρ_c, with

$$\tau_{\text{scaled}} = \frac{\tau - \tau_{\text{TAMS}}}{\tau_{\text{TASG}} - \tau_{\text{TAMS}}}. \tag{2.9}$$

For each model i, the errors associated with each interpolation method and chosen age proxy are given by

$$\delta\nu_{i,\ell,n,\text{norm}} = \left(\nu_{\ell,n,\text{norm,theoretical}} - \nu_{\ell,n,\text{norm,interpolation}}\right)_i, \tag{2.10}$$

where *theoretical* and *interpolation* stand for the value outputted by GYRE and by the interpolation algorithm considered, respectively. Dimensional versions of these errors were computed using the equation

$$\delta\nu_{i,\ell,n} = \delta\nu_{i,\ell,n,\text{norm}} \times \sqrt{GM/R^3}. \tag{2.11}$$

2.3. Results of the Interpolation Tests

In this Chapter, to characterize the interpolation errors on a given evolutionary track of mass M*, we define two metrics, namely: (i) the maximum error for a given mode degree ℓ ($m_{\ell,M}$), i.e. the maximum absolute interpolation error observed for all modes of a given degree in all interpolated models pertaining to the chosen evolutionary track, and (ii) the

*M is used as index to our metrics (and not to be confused with the azimuthal order).

average offset for a given mode degree ℓ on the evolutionary track of mass M ($\mu_{\ell,M}$), calculated as a weighted mean of all absolute interpolated errors, $|\delta\nu_{i,\ell,n,M}|$, for all modes on all interpolated models pertaining to the chosen evolutionary track. Specifically,

$$\mu_{\ell,M} = \frac{1}{\sum_n \sum_i w_{i,M}} \sum_n \sum_i |\delta\nu_{i,\ell,n,M}| w_{i,M} \tag{2.12}$$

where

$$w_{i,M} = (\tau_{\text{scaled},i+1} - \tau_{\text{scaled},i-1})/2. \tag{2.13}$$

The sum in n is over all the radial orders considered for an evolutionary track (cf. Section 2.2.1), while the sum over i includes all the models for a given radial order and evolutionary track. The weight $w_{i,M}$ ensures that the same weight is given to similar intervals of τ_{scaled}, preventing the metric from being biased towards the evolved subgiants due to our grid having models similarly distributed in ρ_c, rather than in τ_{scaled}. In the sections that follow, we drop the indices ℓ and M in the quantities $m_{\ell,M}$ and $\mu_{\ell,M}$, and the indices i and M in $\delta\nu_{i,\ell,n,M}$. The mode degree, the mass of the evolutionary track and, when relevant, the model are, instead, identified in the text or legend where these quantities appear.

2.3.1 Interpolation Along Evolutionary Tracks

We started by performing a control study of the errors on the frequencies that result from applying interpolation along an evolutionary track. Accordingly, we consider all evolution frequency curves (each defined by a different fixed radial order) determined for the mass track with $M = 1.245\ M_\odot$, and consider two possible interpolation methods - linear interpolation and cubic splines, and three possible age proxies - τ, τ_{scaled} and ρ_c. The results are displayed in Figure 2.4 and Table 2.1 for $\ell = 0$, and in Figure 2.5 and Table 2.2 for $\ell = 1$, according to their maximum errors, m, and average offsets, μ, as defined above.

The results of interpolation along evolutionary tracks considering τ as the age proxy are exactly the same as when considering τ_{scaled} as the age proxy, since both age proxies are related by a proportionality constant (cf. Equation 2.9) that remains unchanged within a fixed evolutionary track.

For radial modes, the average offset of the interpolation errors is about 3 orders of magnitude smaller than the accuracy limit we set ($\sim$0.1 μHz). This is expected, as the frequencies of radial modes evolve smoothly and therefore do not produce significant interpolation

Table 2.1: Average offsets (μ) and maximum errors (m) from interpolation along the evolutionary track with 1.245 $M_\odot$, for all $\ell = 0$ mode frequencies, considering the indicated interpolation algorithms. We notice that interpolation errors are the same for τ and τ_{scaled}.

	Errors	Linear	Cubic Splines
τ, τ_{scaled}	μ (μHz)	3.9×10^{-4}	9.8×10^{-5}
	m (μHz)	6.1×10^{-3}	3.7×10^{-3}
ρ_c	μ (μHz)	7.1×10^{-4}	1.6×10^{-4}
	m (μHz)	7.9×10^{-3}	5.6×10^{-3}

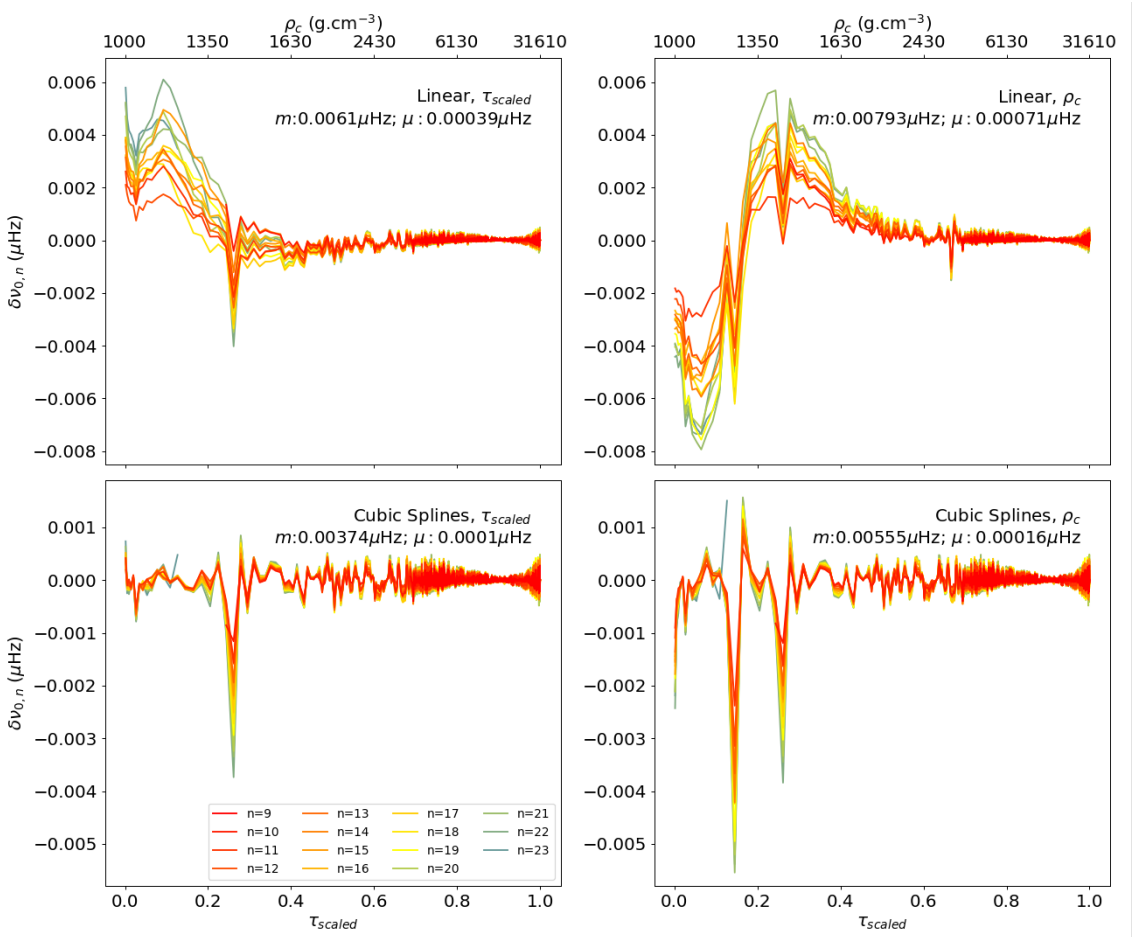


Figure 2.4: Interpolation errors presented as a function of τ_{scaled} (bottom x-axis) and ρ_c (top x-axis), that resulted from interpolation along the evolutionary track with $M = 1.245\ M_\odot$, for all $\ell = 0$ frequency modes, with radial orders $n \in [9, 23]$, indicated by different colours. Each subplot presents the results for a different interpolation method, considering different methods - linear (top panels) or cubic splines (bottom panels) - and different age proxies - τ_{scaled} (left) and ρ_c (right).

errors. We observe only a slight improvement when increasing the order of the interpolation (from linear to cubic splines) and no significant dependence on the adopted age proxy.

For the $\ell = 1$ modes, we again observe that the interpolation errors are essentially independent of the age proxy considered. However, the results for the dipole modes show a

Table 2.2: Average offsets (μ) and maximum errors (m) from interpolation along the evolutionary track with 1.245 $M_\odot$, for all $\ell = 1$ mode frequencies, considering the indicated interpolation algorithms. We notice that interpolation errors are the same for τ and τ_{scaled}.

	Errors	Linear	Cubic Splines
τ, τ_{scaled}	μ (μHz)	5.4×10^{-3}	2.3×10^{-4}
	m (μHz)	1.7×10^{-1}	3.0×10^{-2}
ρ_c	μ (μHz)	5.5×10^{-3}	3.4×10^{-4}
	m (μHz)	1.8×10^{-1}	3.3×10^{-2}

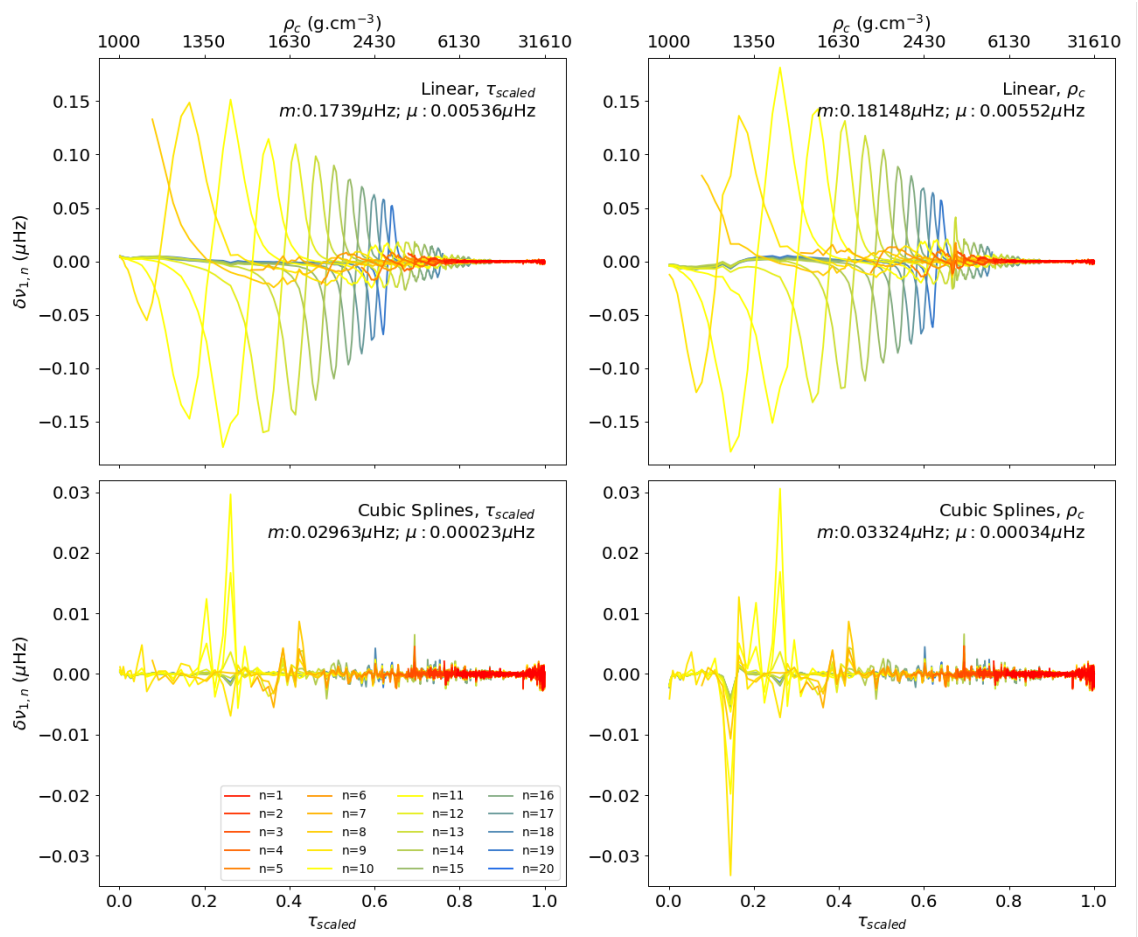


Figure 2.5: Interpolation errors presented as a function of τ_{scaled} (bottom x-axis) and ρ_c (top x-axis), that resulted from interpolation along the evolutionary track with $M = 1.245$ $M_\odot$, for all $\ell = 1$ frequency modes, with radial orders $n \in [1, 20]$, indicated by different colours. Each subplot presents the results for a different interpolation method, namely linear (top panels) and cubic splines (bottom panels), and different age proxies - τ_{scaled} (left) and ρ_c (right).

significant dependence on the interpolation method, with the average offset resulting from linear interpolation being approximately 19.8 times larger than the average offset obtained using cubic splines. This shows that the cubic splines interpolation method is preferred for interpolation along evolutionary tracks for dipole modes. Moreover, the results show that the maximum error when interpolating with cubic splines along the evolutionary track

is about an order of magnitude smaller than the typical observational errors ($\sim$0.1 μHz), leaving room for additional errors that will result from the interpolation across different evolutionary tracks, and that we will address in Sections 2.3.2-2.3.5.

In Appendix A, we present the results of interpolation along evolutionary tracks for all the mass tracks in our stellar grid. This emphasizes our choice in highlighting the results for the mass track with $M = 1.245$ M$_\odot$, as its interpolation errors are comparable in magnitude to those of other tracks, making it a representative example for interpolation along evolutionary tracks.

2.3.2 Full Interpolation with τ and τ_{scaled} as Age Proxies

In this section, we analyse the errors resulting from the application of the full interpolation algorithm employed in the computation of the frequencies of models that do not lie on a particular evolutionary track. To this end, we consider a subset of our grid composed only of the models whose third decimal place of the associated mass value is 0 (e.g., 1.240) in order to retrieve through interpolation the models of the initial complete grid - namely those whose third decimal place of the associated mass value is 5 (e.g., 1.245).

As before, the initial tests are performed for models with $M = 1.245$ M$_\odot$, whose frequencies are computed through interpolation, and subsequently compared with the true frequencies computed for the initial grid using GYRE. These tests will then be extended to the full grid in Section 2.3.4 and in Appendix B. The interpolation is made using the corresponding adjacent evolutionary tracks from the subset grid (2 for linear interpolation across tracks and 4 for the cubic splines interpolation across tracks). The results considering cubic splines along an evolutionary track and linear interpolation across evolutionary tracks are shown in Figure 2.6 and Table 2.3 for $\ell = 0$, and in Figure 2.7 and Table 2.4 for $\ell = 1$. Results from interpolating $\ell = 1$ modes using cubic splines both along and across evolutionary tracks are shown in Figure 2.8. In all three figures, the results from considering τ as the age proxy are shown in the top panels, while the results from considering τ_{scaled} as the age proxy are shown in the middle panels.

For radial modes (Figure 2.6), the smallest maximum errors and average offsets were obtained when τ_{scaled} is considered as the age proxy, with values of 1.4×10^{-1} and 6.9×10^{-2} μHz, respectively. This shows that, even for radial modes, interpolation errors can be larger than our goal, albeit not significantly so. Despite the absence of avoided crossings, the evolution of $\ell = 0$ mode frequencies for different mass tracks is not aligned when

Table 2.3: Average offset (μ) and maximum errors (m) from the full interpolation algorithm (that considers cubic splines along tracks and linear across tracks). The results are for all $\ell = 0$ modes associated with the evolutionary track with 1.245 $M_\odot$ (determined from interpolation using adjacent evolutionary tracks), for each of the age proxies indicated.

	Errors	Linear
τ	μ (μHz)	5.0×10^{-1}
	m (μHz)	3.7×10^{0}
τ_{scaled}	μ (μHz)	6.9×10^{-2}
	m (μHz)	1.4×10^{-1}
ρ_c	μ (μHz)	7.3×10^{-2}
	m (μHz)	3.0×10^{-1}

expressed as a function of the age proxies considered. Thus, interpolation between different evolutionary tracks will happen between different phases of evolution of the modes, as shown in Figure 2.9. This effect is more evident for the frequency evolution in age (top panel) than for the frequency evolution in τ_{scaled} (bottom panel), which is consistent with the errors presented in Table 2.3.

In the case of $\ell = 1$ modes, the linear interpolation across tracks is again found to give better results when τ_{scaled} is taken as the age proxy (middle panel of Figure 2.7), compared to using τ (top panel of Figure 2.7). However, the average offset of 5.6×10^{-1} μHz and the maximum error of 3.6×10^{0} μHz are already larger than our accuracy limit, with m being an order of magnitude greater than that limit. The reason for these errors when considering τ or τ_{scaled} as the age proxy has been discussed in Section 1.4.2 and can be further understood from the left and middle panels of Figure 2.10. Because the mixed modes are not aligned when the frequency curves are described as a function of these age proxies, interpolation between different evolutionary tracks happens between different phases of evolution of the mixed modes, failing even when considering a relatively dense grid of models. Thus, for the cases presented, it is not possible to obtain results within the accuracy limit set by the typical observational errors with this choice of methods and age proxies, which could potentially limit the use of stellar grids with interpolation to explore the parameter space when fitting seismic data for subgiant stars.

2.3.3 Central density ρ_c as an Alternative Age Proxy

As discussed in Section 1.4.2, the avoided crossings on evolutionary tracks with different masses appear more aligned when the frequencies are displayed as a function of the central density, ρ_c (right plot of Figure 2.10). With the avoided crossings showing an

Table 2.4: Average offset (μ) and maximum errors (m) from the full interpolation algorithm (that considers cubic splines along tracks and the indicated regression method across tracks). The results are for all $\ell = 1$ modes associated with the evolutionary track with 1.245 $M_\odot$ (determined from interpolation using adjacent evolutionary tracks), for each of the age proxies indicated.

	Errors	Linear	Cubic Splines
τ	μ (μHz)	7.3×10^{0}	6.1×10^{0}
	m (μHz)	2.6×10^{1}	2.7×10^{1}
τ_{scaled}	μ (μHz)	5.6×10^{-1}	5.7×10^{-1}
	m (μHz)	3.6×10^{0}	3.3×10^{0}
ρ_c	μ (μHz)	1.4×10^{-1}	1.5×10^{-1}
	m (μHz)	1.2×10^{0}	1.3×10^{0}

increased alignment when described as a function of ρ_c, interpolation can happen between models whose mode frequencies are in a more similar phase of evolution, which is expected to lead to more accurate results.

With the above in mind, we now analyse the results from applying the full interpolation algorithm to predict the frequencies of models of the evolutionary track of $M = 1.245\ M_\odot$, using ρ_c as the age proxy. These results are shown in the bottom panels of Figures 2.6, 2.7 and 2.8, and summarized in Tables 2.3 and 2.4, for mode frequencies with $\ell = 0$ and 1, respectively.

For the radial modes ($\ell = 0$) (bottom panel of Figure 2.6), interpolation errors using ρ_c as the age proxy can be as high as 3.0×10^{-1} μHz, only decreasing below 5.0×10^{-2} μHz in later stages of evolution. In fact, this maximum error is close but slightly larger than the one obtained considering τ_{scaled} as the age proxy ($m = 1.4 \times 10^{-1}$ μHz) and than the reference value of 0.1 μHz. This is not surprising since radial modes do not have avoided crossings; thus, no particular improvement was to be expected by choosing ρ_c over τ_{scaled} as the age proxy. Although some of the radial orders produce interpolation errors above the established accuracy limit, these are limited to the models of the early subgiant phase with $\tau_{\text{scaled}} < 0.4$. Despite these large maximum absolute errors in some models, the average offset is 7.3×10^{-2} μHz, well within the proposed accuracy limit.

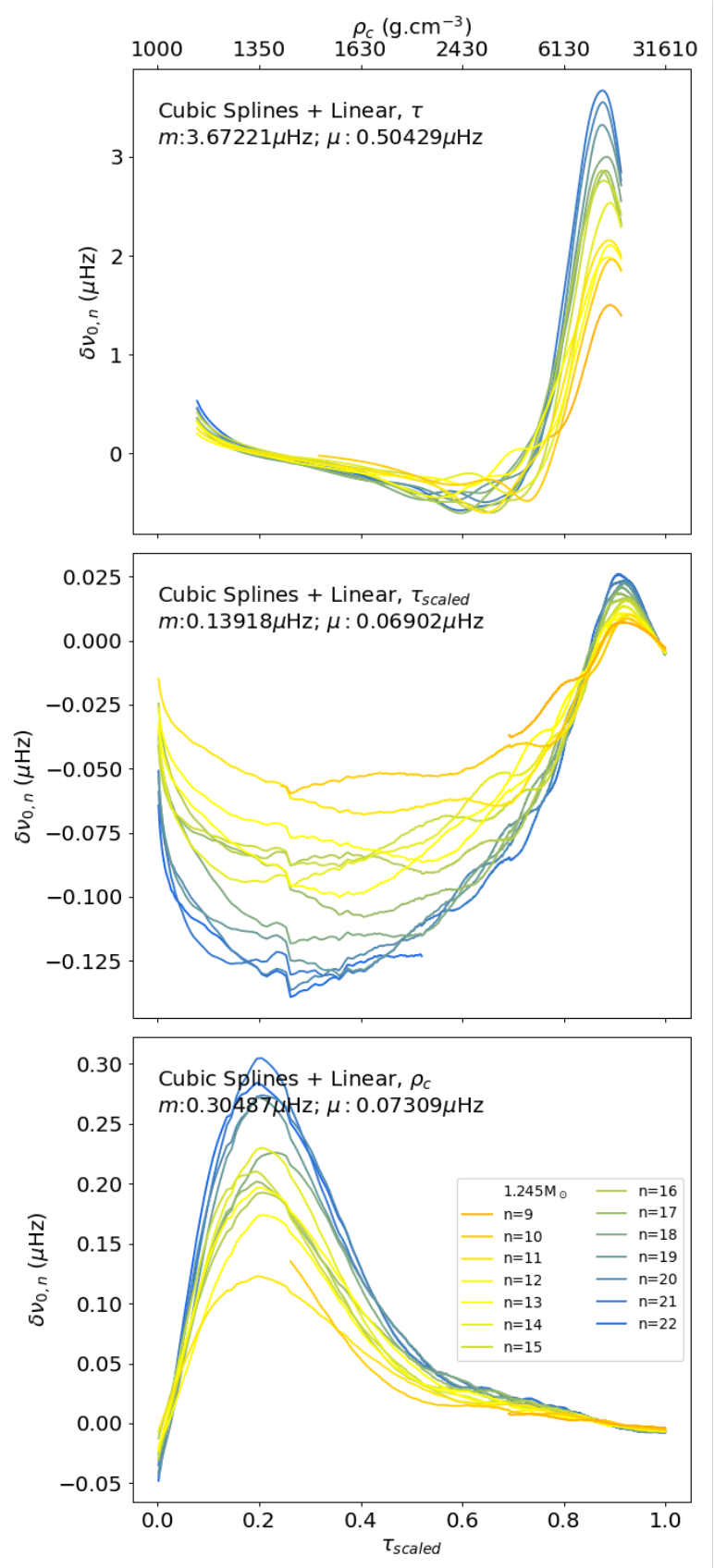


Figure 2.6: Interpolation errors presented as a function of τ_{scaled} (bottom x-axis) and ρ_{c} (top x-axis), that resulted from the full interpolation algorithm (cubic splines interpolation along tracks, and linear interpolation across tracks) for all $\ell = 0$ modes associated with the mass track $M = 1.245\,\text{M}_\odot$, when considering τ (top), τ_{scaled} (middle) and ρ_{c} (bottom) as the age proxies for interpolation.

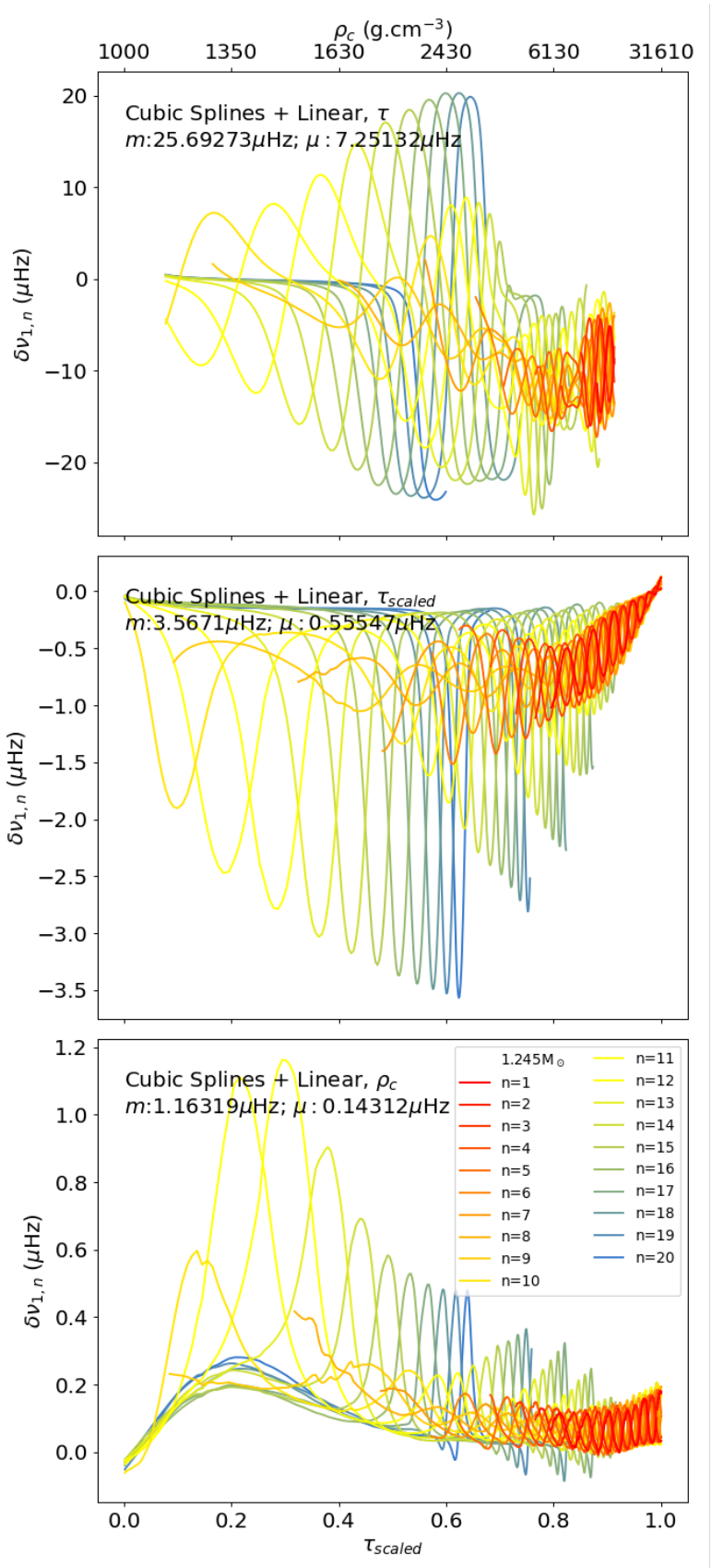


Figure 2.7: Interpolation errors presented as a function of τ_{scaled} (bottom x-axis) and ρ_{c} (top x-axis), that resulted from the full interpolation algorithm (cubic splines interpolation along tracks, and linear interpolation across tracks) for all $\ell = 1$ modes associated with the track with $M = 1.245$ M$_\odot$, when considering τ (top), τ_{scaled} (middle) and ρ_{c} (bottom) as the age proxies for interpolation.

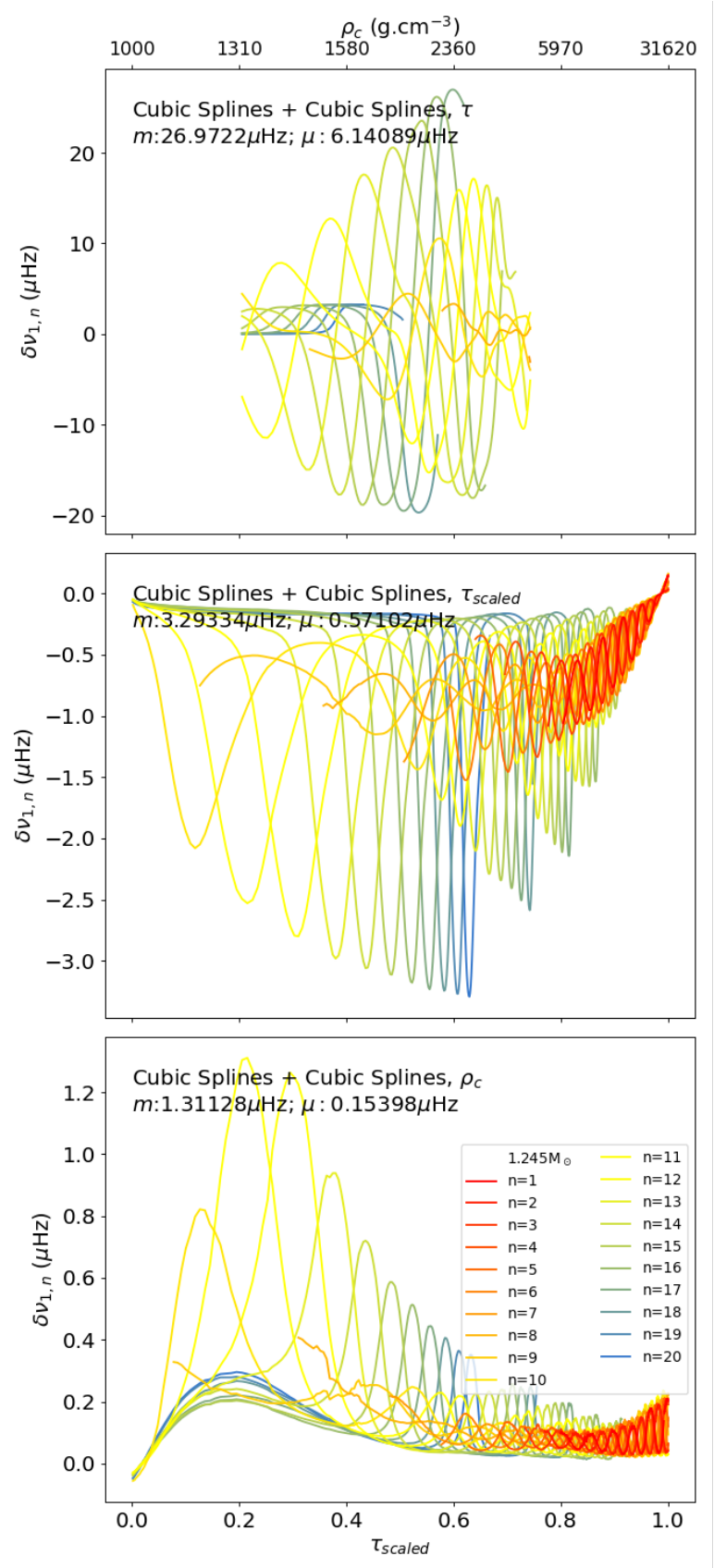


Figure 2.8: Interpolation errors presented as a function of τ_{scaled} (bottom x-axis) and ρ_{c} (top x-axis), that resulted from the full interpolation algorithm (cubic splines interpolation both along and across tracks) for all $\ell = 1$ modes associated with the track with $M = 1.245$ M$_\odot$, when considering τ (top), τ_{scaled} (middle) and ρ_{c} (bottom) as the age proxies for interpolation.

For $\ell = 1$ modes, errors from interpolation considering ρ_c as the age proxy can be as high as 1.2×10^0 and 1.3×10^0 μHz, depending on the order of the interpolation method considered (Figures 2.7 and 2.8, respectively), only decreasing to values below 4.0×10^{-1} μHz in the later stages of the subgiant evolution. Although their maxima are quite large (about an order of magnitude above the accuracy limit we set as reference), the average offset is improved by a factor of $\sim$3.9 over the average offset of interpolation with τ_{scaled} as the age proxy, yielding results similar to the expected accuracy limits: 1.4×10^{-1} and 1.5×10^{-1} μHz for linear and cubic splines interpolation, respectively. We verified that this improvement in the interpolation errors is not a consequence of the grid being equally spaced in ρ_c, rather than τ_{scaled}, (note that the errors from interpolation along the tracks are always small, regardless of the age proxy being adopted when compared with the final errors) (cf. Table 2.2).

2.3.4 Results for the Full Grid

Next, we apply the analysis to the full grid and discuss the complete set of results. To this end, we use the mode frequencies from the models whose third decimal place in the associated mass value is 0 to obtain the frequencies for the missing mass tracks that also appear in the initial grid (i.e., those whose third decimal place in the associated mass value is 5). Results are presented in the tables in Appendix B, and summarized in Figure 2.11. Interpolation was not performed for tracks with masses 1.155 and 1.345 $M_\odot$, as they are near the limit where there are not enough models on one side to allow cubic spline interpolation.

The results from Figure 2.11 show that using ρ_c as the age proxy significantly improves the accuracy of the interpolation compared to τ_{scaled}. For $M > 1.20$ $M_\odot$, both the average offset and maximum error are smaller when ρ_c is used instead of τ_{scaled}, as the age proxy. For lower masses, there are a few cases where the interpolation errors obtained with the two age proxies are comparable, but only for one mass track both the average offset and the maximum error are larger when ρ_c is chosen. Moreover, we see that, with the exception of the mass track $M = 1.175$ $M_\odot$ (brown dashed line in Figure 2.11), the average offset when taking ρ_c as the age proxy is always approximately within a factor of two of the reference value. It also becomes evident that, for the more massive evolutionary tracks, the average offset when considering τ_{scaled} as the age proxy is similar to the maximum error found when ρ_c is chosen. Thus, when considering the full grid, the adoption of ρ_c in place of τ_{scaled} as the age proxy seems well justified. Finally, Figure 2.11

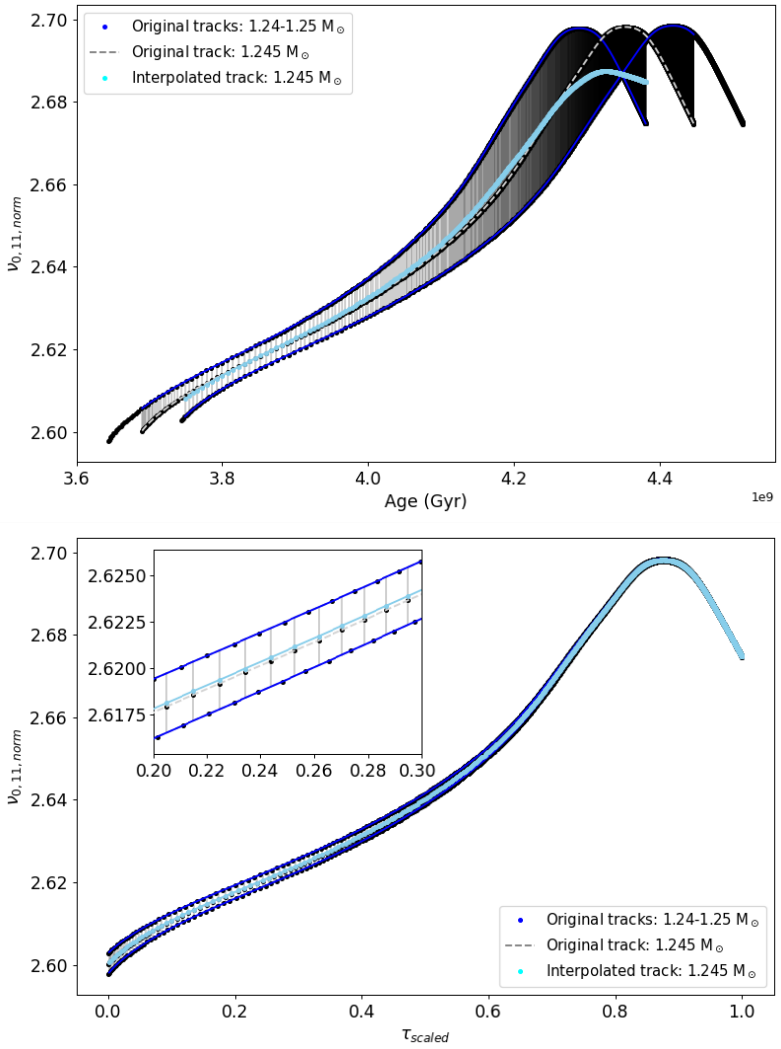


Figure 2.9: Evolution of the scaled frequencies for the $\ell = 0$ modes, with radial order n=11, resulting from the application of the interpolation algorithm to the mass track with 1.245 $M_{\odot}$, presented as a function of τ (top) and τ_{scaled} (bottom), when each is considered as the respective age proxy for interpolation. The bottom panel includes a subplot that zooms in on the region of the age proxy parameter space with the largest interpolation errors.

confirms that the evolutionary track of $M = 1.245$ $M_{\odot}$ (brown dotted line), considered in the previous sections, has typical interpolation errors, justifying its use in the more detailed analysis presented. It also shows that there is an evolutionary track ($M = 1.175$ $M_{\odot}$) for which interpolation performs significantly worse. We shall address the origin of these anomalously large interpolation errors found for the latter model track in Section 3.2.

2.3.5 Impact of the Order of Interpolation

Having discussed the results of interpolation considering different age proxies, we now compare the performance of the different orders of interpolation when interpolating across

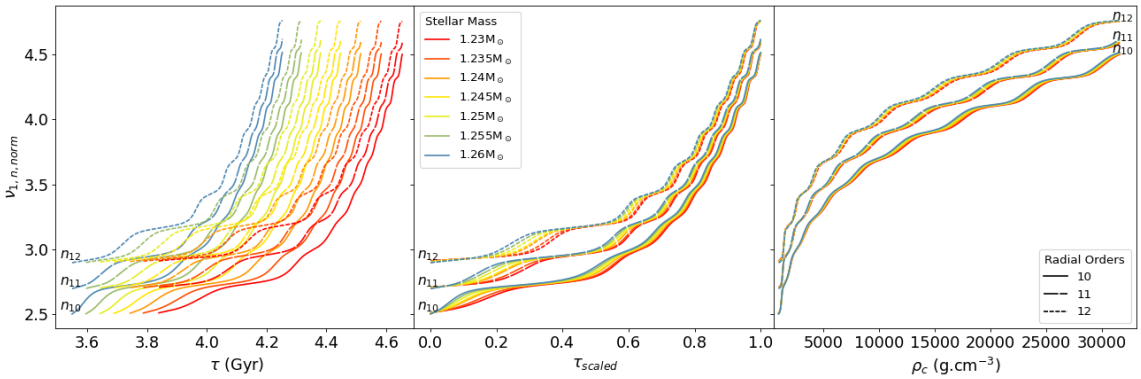


Figure 2.10: Evolution of the normalized frequencies of non-radial $\ell = 1$ modes, with radial orders $n = [10,11,12]$, for evolutionary tracks of the stellar grid with masses between 1.23 and 1.26 $M_\odot$, as a function of the various age proxies considered for interpolation: τ (left), τ_{scaled} (middle), and ρ_c (right). Different colours are used to represent different stellar masses and different line styles show different radial orders, according to the insets in the middle and right panel, respectively.

evolutionary tracks for a fixed value of the age proxy. We compare the results of applying linear interpolation (Figure 2.7) and cubic splines interpolation (Figure 2.8) to the $\ell = 1$ modes of models in the mass track with 1.245 $M_\odot$. These results, summarized in Table 2.4, show that the average offset and the maximum error hardly change when varying the order of interpolation. This holds true for both τ_{scaled} and ρ_c as age proxies.

Considering the full grid does not change these conclusions in any significant way, when taking ρ_c as the age proxy, we identified eight interpolated mass tracks where linear interpolation performed better (i.e., resulting in smaller μ and m values than when employing the cubic splines), nine cases where cubic splines interpolation performed better, and one case where the results were mixed (for $M = 1.225$ $M_\odot$, the smallest μ and m values were found using different methods). These results suggest no strong preference for either interpolation method when performing interpolation across evolutionary tracks. Moreover, inspection of the tables in Appendix B shows that the average offsets computed with linear and cubic splines interpolation for each individual track are almost always of the same order of magnitude. The most significant differences are found for $M = 1.165$ and 1.185 $M_\odot$, for which μ from linear interpolation can be approximately 6.2 and 3.2 times smaller than μ from cubic splines, respectively. These two cases, together with the mass track with 1.175 $M_\odot$, which presents the highest interpolation errors in this grid (see Figure 2.11), span the region of the mass parameter space where the core properties of the modelled stars change. This will be discussed in detail in Section 3.2.

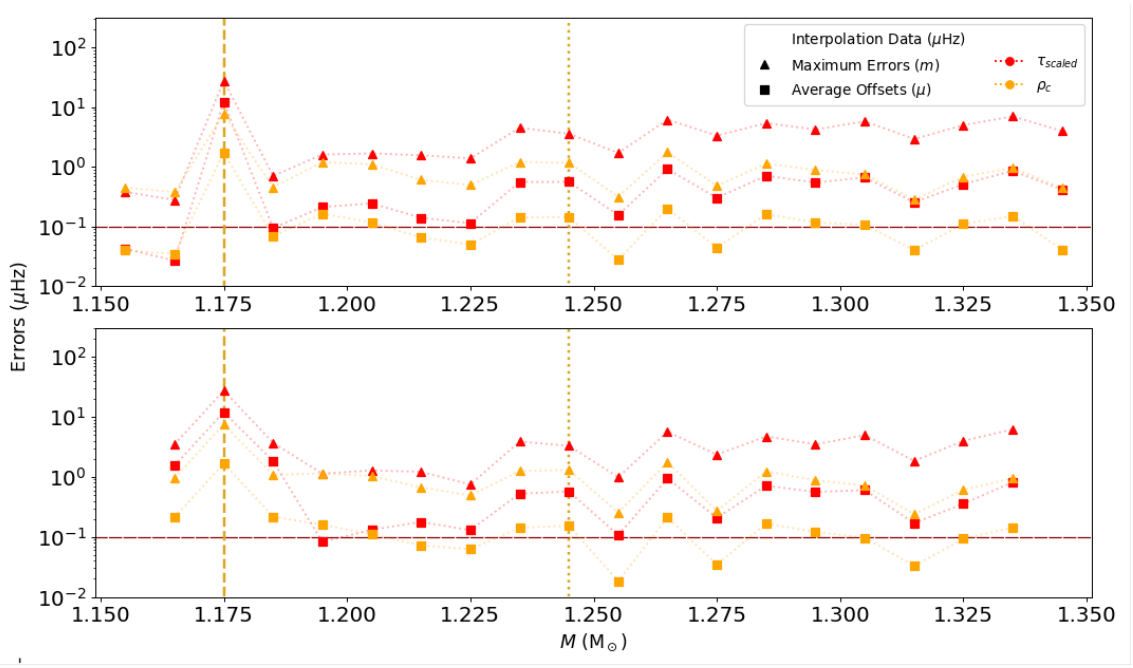


Figure 2.11: Average offsets (μ, indicated by squares; in μHz) and maximum errors (m, indicated by triangles; in μHz) from the full interpolation method, which considers cubic splines along evolutionary tracks and linear (top) or cubic splines (bottom) interpolation across evolutionary tracks and τ_{scaled} (red) or ρ_{c} (yellow) as the age proxy, for all $\ell = 1$ modes obtained for the interpolated tracks of the initial grid. The horizontal line at 10^{-1} μHz indicates the accuracy limit set for these tests. The vertical brown dotted line highlights the results for our reference track with $M = 1.245$ M$_\odot$, while the vertical brown dashed line highlights the anomalous track with $M = 1.175$ M$_\odot$.

Given the results presented in the previous subsections, we favour the interpolation approach that is both the simplest and least computationally expensive: cubic splines for interpolation along tracks, linear interpolation for interpolation across tracks, and ρ_{c} as the age proxy.

2.3.6 Testing the Grid Resolution

We now recall that every evolutionary track in the initial grid has between 2959 and 2963 models, with about half of them (approximately 1482 models) being used to determine the other half through interpolation. This is a large number of models occupying the system memory, and therefore, we aim to assess the impact of the grid resolution on the interpolation errors. Considering the results from the previous sections, we divide this analysis into two parts, with two different objectives. The first concerns interpolation along evolutionary tracks, where we determine what is the minimum number of models per track required to maintain accuracy within the specified limit.

Table 2.5: Average offsets (μ) and maximum errors (m) resulting from interpolation along the evolutionary track with $M = 1.245$ $M_\odot$ (considering a cubic polynomial or cubic splines method), when considering ρ_c as the age proxy, for all associated $\ell = 1$ mode frequencies, and for the indicated grid resolutions, $1/k$.

		Method for Interpolation Along	
Resolution	Errors	Cubic Polynomial	Cubic Splines
1/1	μ (μHz)	7.0×10^{-4}	3.4×10^{-4}
	m (μHz)	4.1×10^{-2}	3.3×10^{-2}
1/2	μ (μHz)	3.3×10^{-3}	1.0×10^{-3}
	m (μHz)	1.1×10^{-1}	8.3×10^{-2}
1/3	μ (μHz)	1.3×10^{-2}	5.4×10^{-3}
	m (μHz)	3.4×10^{-1}	2.1×10^{-1}
1/4	μ (μHz)	3.5×10^{-2}	1.6×10^{-2}
	m (μHz)	8.3×10^{-1}	5.6×10^{-1}
1/5	μ (μHz)	7.3×10^{-2}	3.1×10^{-2}
	m (μHz)	1.7×10^{0}	1.1×10^{0}
1/6	μ (μHz)	1.4×10^{-1}	1.3×10^{-1}
	m (μHz)	2.8×10^{0}	3.4×10^{0}

With this objective in mind, we consider multiple subgrids, each with a fraction of the resolution of the initial grid, $1/k$, where each evolutionary track is built by selecting every k^{th} model from the initial track. In this study, we focus on the evolutionary track with 1.245 $M_\odot$, and test grid resolutions ranging from 1/1 (the initial grid) to 1/6 of the initial grid (which contains only $\sim$247 models per track for interpolation). Although we continue to test different interpolation methods, we establish ρ_c as the definitive age proxy. The results are summarized in Table 2.5.

In addition to cubic splines, we tested the grid resolution using interpolation with cubic polynomials, for which we expect errors to increase as k^4. However, as we found that not to be the case, we made a sanity test on an evolutionary track with 10 times the number of models of the initial grid. In that much denser grid, we find that our interpolation routine produces errors that scale as expected, implying that the interpolation routine is correctly implemented but our grid is not sufficiently dense to reach such regime. This sanity test and its results are discussed in Appendix C.

We observe that both the average offset μ and the maximum error m increase significantly when the grid resolution is reduced. For a grid resolution of 1/6, both μ and m increase by more than 2 orders of magnitude. However, while the average offset changes from 3.4×10^{-4} to 1.3×10^{-1} μHz, a value still close to the established accuracy limit, the

Table 2.6: Average offsets (μ) and maximum errors (m) from the full interpolation algorithm (that considers cubic splines along tracks, the indicated interpolation method across tracks - linear or cubic splines, - and ρ_c as the age proxy) applied to all $\ell = 1$ modes associated with the evolutionary track with $M = 1.245$ $M_\odot$ (determined from adjacent evolutionary tracks), for different grid resolutions, $1/k$.

		Method for Interpolation Across	
Resolution	Errors	Linear	Cubic Splines
1/1	μ (μHz)	1.4×10^{-1}	1.5×10^{-1}
	m (μHz)	1.2×10^{0}	1.3×10^{0}
1/2	μ (μHz)	1.5×10^{-1}	1.6×10^{-1}
	m (μHz)	1.3×10^{0}	1.4×10^{0}
1/3	μ (μHz)	1.6×10^{-1}	1.7×10^{-1}
	m (μHz)	1.3×10^{0}	1.4×10^{0}
1/4	μ (μHz)	1.6×10^{-1}	1.7×10^{-1}
	m (μHz)	1.5×10^{0}	1.4×10^{0}
1/5	μ (μHz)	1.7×10^{-1}	1.7×10^{-1}
	m (μHz)	1.7×10^{0}	1.4×10^{0}
1/6	μ (μHz)	2.5×10^{-1}	1.8×10^{-1}
	m (μHz)	3.8×10^{0}	1.4×10^{0}

maximum errors increase from 3.3×10^{-2} to 3.4×10^{0} μHz, which is well beyond the established accuracy limit. To ensure that interpolation errors along evolution are within values comparable to the goal, our results suggest that the minimal grid resolution recommended should be no less than 1/3 of the initial grid (i.e., a grid with approximately 494 models per track for interpolation). In this case, the maximum error of 2.1×10^{-1} μHz is only slightly higher than the established accuracy limit.

The second part of the exercise concerns the impact of the grid resolution on the interpolation across evolutionary tracks. In Section 2.3.4, we found that the results for the current grid fail to comply with the reference accuracy in what concerns the maximum error, while performing reasonably close to the goal (within a factor of two) in what concerns the average offset, when ρ_c is used as the age proxy. Thus, depending on the quality of the data, the accuracy achieved with our reference grid may still suffice; in this case, it remains important to understand whether a similar accuracy can be achieved with a reduced number of models. To test this, and the corresponding impact on the interpolation errors, we repeat the exercise of decreasing the grid resolution for the case of full interpolation.

Table 2.6 displays the results of the full interpolation algorithm applied to different grid resolutions, considering cubic splines for interpolation along tracks, and either linear or

cubic splines for the interpolation across tracks. For the case previously established as the preferred option (cubic splines along and linear across), we observe a weaker dependence of the interpolation errors with the subgrid resolution compared to interpolation along evolution alone. Indeed, the average offsets remain close to the accuracy limit, increasing only slightly until the subgrid with 1/6 of the models is considered. Moreover, the maximum errors, which are found to be out of the accuracy limit already in the initial grid, hardly change when the number of models is decreased to 1/3 of the initial value. The impact of further decreasing the number of models to 1/6 of the initial number seems to depend on the order of the method applied for the interpolation across evolutionary tracks, with cubic splines performing somewhat better when the number of models is significantly decreased.

In conclusion, we find that reducing the number of models per evolutionary track to approximately 1/3 of the initial value does not impact the accuracy of the interpolation results from our grid in any significant way. However, we emphasize that, in all cases, the maximum interpolation errors remain significantly above the goal (as seen in Figure 2.11, and discussed in Section 2.3.4).

2.4. Conclusions

In this study, we began by examining a group of interpolation methods when applied both along and across evolutionary tracks, especially focusing on a specific mass track with 1.245 $M_\odot$. Accordingly, we analyzed all the frequency curves corresponding to this mass track, by considering two possible interpolation methods - linear interpolation and cubic splines, and three possible age proxies - τ, τ_{scaled}, and ρ_c.

For $\ell = 1$ frequency modes, our analysis of the mass track with 1.245 $M_\odot$ revealed that the most effective interpolation approach should consider cubic splines for interpolation along tracks, linear interpolation for interpolation across tracks, and ρ_c as the preferred age proxy. This approach resulted in an average offset of 1.5×10^{-1} μHz, which is about 1.5 times greater than the desired accuracy limit of 0.1 μHz, and a maximum error of 1.3×10^{0} μHz, which exceeds the accuracy limit by at least an order of magnitude. This showed that the accuracy goal is not satisfied in any of the configurations considered.

The results of applying interpolation to the full grid, shown in Figure 2.11, confirm the

preference for using ρ_c as the age proxy over τ_{scaled}, as it significantly improves the accuracy of interpolation for most tracks of the stellar grid. Furthermore, we observe that, with the exception of the mass track with 1.175 $M_\odot$, the average offset when taking ρ_c as the age proxy is always approximately within a factor of two of the reference value. Figure 2.11 also shows that the evolutionary track with $M = 1.245$ $M_\odot$, discussed in the previous subsections, exhibits typical interpolation errors, which justifies why it was chosen for a more detailed analysis, and supports the generalization of its conclusions to the full grid. The only exception, the mass track with 1.175 $M_\odot$, for which interpolation performs significantly worse, will be addressed in Section 3.2.

Finally, we also presented the results of testing different resolutions of the initial grid and their implications for the interpolation results. We found that reducing the number of models per evolutionary track to approximately 1/3 of the initial value (i.e., $\sim$500 models per evolutionary track) does not impact the accuracy of the interpolation results from our grid in any significant way. However, we emphasize that, for all resolutions tested, the maximum interpolation errors remain significantly above the goal.

3. The Effects of Convective Boundary Mixing on Interpolation

In Sections 2.3.4 and 2.3.5, we noted that all measurements of interpolation errors are significantly larger for the evolutionary track with $M = 1.175$ $M_\odot$ (see the brown dashed line in Figure 2.11). In this Chapter, we investigate the origin of these larger errors - connecting them to the treatment of core overshoot at the mass threshold for convective cores to appear in the main-sequence (MS). We also discuss the implications that such transition may have in the construction of future model grids.

The content of the following chapter is adapted from the work published in Clara et al. (2025), which has been published in *Astronomy & Astrophysics*.

3.1. Introduction

Recent years have seen a renewed interest in the subject of overshoot, with several studies directed towards the understanding of the underlying physics, distinguishing the various mixing mechanisms, and constraining the amount of overshooting required for different types of stars (Deheuvels et al. (2016), Claret and Torres (2017), Claret and Torres (2018), Pedersen et al. (2018), Mombarg et al. (2021), Anders and Pedersen (2023), Lindsay et al. (2024)).

In Section 1.2.3, we discussed the prescriptions most commonly applied when modelling overshoot in evolutionary codes, particularly for stars with convective cores (i.e. $M \gtrsim 1.1$ $M_\odot$). For these, we have discussed options for how to treat the thermal structure inside an overshoot region affected by extra mixing (see penetrative overshoot and convective overshoot), as well as how instantaneous and homogeneous the chemical mixing can be (see step overshoot and exponential diffusive overshoot)*. However, we did not address how the implementation of convective core overshoot should relate with the stellar parameters commonly considered as grid inputs, such as mass and initial metallicity.

In our grid (presented in Section 2.2), whenever a convective core is present, we adopted a prescription that combines convective overshoot (where $\nabla = \nabla_{\rm rad}$ in the overshoot region) and exponential diffusive overshoot (with $f_{\rm ov}$ as the free parameter), applied under

*We note that the diversity of implementations is due to the current lack of observations that could help constrain the physical properties of the extra mixing beyond convective cores.

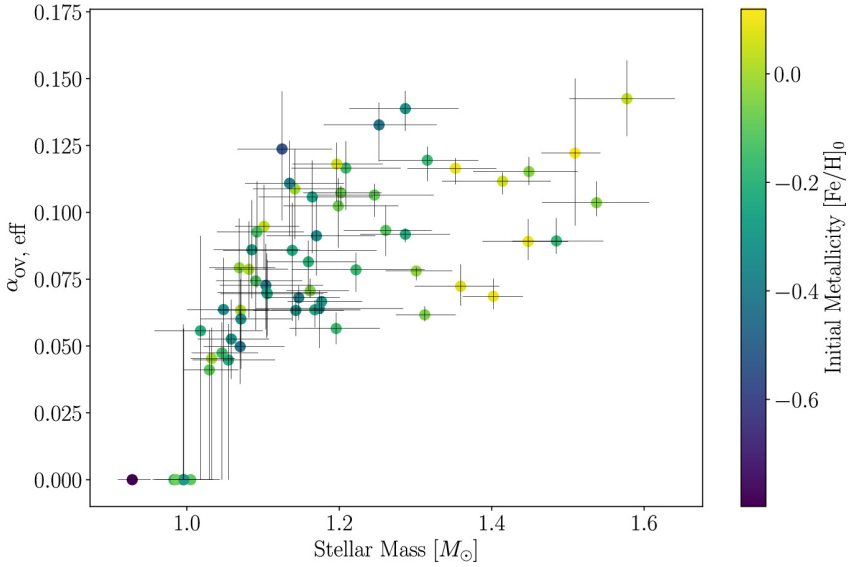


Figure 3.1: Inferred effective overshoot parameter $\alpha_{\rm ov,eff}$ shown as a function of the modelled stellar mass, for the sample of 62 early post-MS stars from Lindsay et al. (2024). Data points are colour-coded according to the modelled initial metallicity. The position and colour of each point represent the 50th percentile of each parameter for each target, with error bars representing the range from the 16th and the 84th percentiles of each parameter's posterior distribution. Plot from Lindsay et al. (2024).

the Schwarzschild criterion, and without semiconvection. Models for each evolutionary track were generated from the beginning of their pre main-sequence with $f_{\rm ov}$ set to 0.01. However, the core overshooting parameter remains poorly constrained, and other overshoot implementations could be considered.

This is expected, since subgiants do not possess convective cores (see Section 1.3). In practice, limits on this parameter for subgiant models are typically inferred indirectly, through studies of how stellar properties are affected by a convective core during the MS.

While subgiant stars do not have a convective core (cf. Section 1.3), the properties of overshooting during the main-sequence influence the cores of stars in the subgiant phase. Therefore, these more evolved stars can be used to constrain the properties of overshoot in their main-sequence progenitors. This has been proposed in several studies, such as that of Lindsay et al. (2024), whose main results we detail below. Figure 3.1 shows the results from Lindsay et al. (2024) for the effective overshoot parameter ($\alpha_{\rm ov,eff}$)* as a function of the stellar mass, with error bars representing the range between the 16th and the 84th percentiles of each parameter's posterior distribution. The results are separated into three main sections: (a) stars with $M \lesssim 1.0\ {\rm M}_\odot$, where $\alpha_{\rm ov,eff} = 0$, because these stars

*Lindsay et al. (2024) consider a step overshoot prescription with free parameters $\alpha_{\rm ov}$ (used as a grid input in their work) and $\alpha_{\rm ov,eff}$ (an effective overshoot parameter, calculated directly from the MESA-generated profile at the time step when the MESA-defined convective core mass was at its maximum).

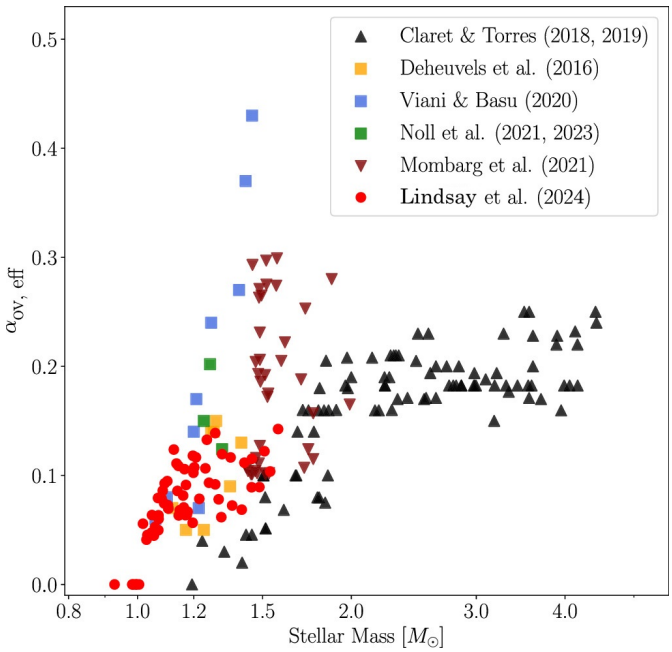


Figure 3.2: Inferred effective overshoot parameter $\alpha_{ov,eff}$ obtained from the works of Lindsay et al. (2024) (red points), Deheuvels et al. (2016) (yellow squares), Viani and Basu (2020) (blue squares), Noll and Deheuvels (2023), Noll et al. (2021) (green squares), Claret and Torres (2018, 2019) (black triangles) and Mombarg et al. (2021) (brown triangles) as a function of the stellar mass. Plot adapted from Lindsay et al. (2024).

cannot sustain convective cores for extended periods of time; (b) stars with $1.0 \lesssim M \lesssim 1.15$ $M_\odot$, where $\alpha_{ov,eff}$ increases with mass; and (c) stars with $M \gtrsim 1.15$ $M_\odot$, where $\alpha_{ov,eff}$ remains largely independent from stellar mass, even through spreading within a range between 0.075 and 0.125. Regarding the relation between $\alpha_{ov,eff}$ and initial metallicity ($[Fe/H]_0$), Lindsay et al. (2024) found no strong correlation between the two parameters.

The results from Lindsay et al. (2024) are compared to other works in Figure 3.2. The plot includes results from several studies that use asteroseismic data to estimate overshooting in similar MS convective cores (Deheuvels et al. (2016), Viani and Basu (2020), Noll and Deheuvels (2023), Noll et al. (2021)), as well as from studies based on a sample of high-mass MS stars from double-line eclipsing binary systems (Claret and Torres, 2018), and a sample of high-mass γ Doradus stars (Mombarg et al., 2021).

First, comparing the works that used asteroseismic data, Lindsay et al. (2024) found that the results at the low-mass end of the sample agree closely with previous works. However, for larger masses ($M \gtrsim 1.3$ $M_\odot$), the results diverge from those of Viani and Basu (2020), what appears to be a result of using different overshooting prescriptions*, and considering a much denser grid of stellar models during the modelling procedure.

*When modelling data, Lindsay et al. (2024) employed a step overshoot prescription, while Viani and Basu (2020) considered penetrative overshoot.

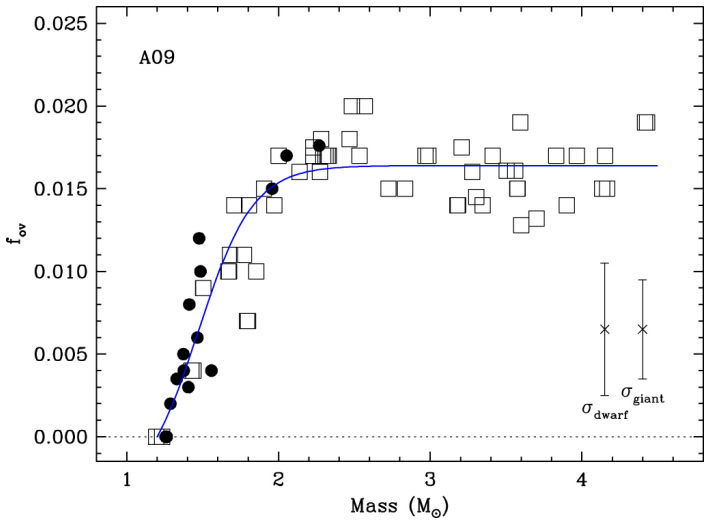


Figure 3.3: Inferred convective overshoot values (f_{ov}) shown as a function of stellar mass, for the sample of dwarf and giant double-line eclipsing binaries presented in Claret and Torres (2018). The typical error bars for these stars are indicated on the lower right. The solid curve provides a convenient fitting to the data, according to Equation 3.1. Plot from Claret and Torres (2018).

The results from Claret and Torres (2018)* show a dependence of $\alpha_{ov,eff}$ on mass similar to Lindsay et al. (2024), although covering a different range of masses. While the sample of eclipsing binaries from Claret and Torres (2018) shows a linear relationship between the two parameters for masses between 1.20 and 2.00 $M_\odot$, Lindsay et al. (2024) presents a similar relation for masses between 1.00 and 1.20 $M_\odot$. According to Lindsay et al. (2024), this might be associated with the different overshooting prescriptions†, with the different resolutions of stellar models grids employed in the modelling process, or with the different modelling procedures considered in each study‡.

In constructing a stellar grid, such as the one presented in Section 2.2.1, it is necessary not only to decide how to treat the overshooting layers, but also its dependence on the model properties. The studies reported above provide evidence that near the transition between stars with radiative cores to stars with convective cores, the overshoot is likely mass dependent, something that has not been considered in our original grid. In fact,

*We do not discuss the results of Mombarg et al. (2021) in the text as their sample is fully outside the mass range we consider, and so do not contribute significantly to this discussion.

†Similarly to Viani and Basu (2020), Mombarg et al. (2021) and Claret and Torres (2018) also considered a penetrative overshoot prescription. However, we note that the results from all these works have been calibrated for comparison, based on a tight correlation observed between α_{ov} and f_{ov}: $\alpha_{ov}/f_{ov} \approx 11.36 \pm 0.22$ (discussed in Claret and Torres (2018), Lindsay et al. (2024) and Anders and Pedersen (2023)).

‡Lindsay et al. (2024) used detailed asteroseismic data from individual oscillation modes, while Claret and Torres (2018) relied on masses, radii, and effective temperatures of binary stars.

based on their sample of high-mass MS eclipsing binaries, Claret and Torres (2018) provide the following relation between $f_{\rm ov}$ and stellar mass M,

$$f_{\rm ov} = \begin{cases} 0, \text{ if } M \leq 1.20 \mathrm{M}_{\odot} \\ \frac{0.02013}{1+e^{-5.5(M-1.47)}} - 0.00373, \text{ if } M > 1.20 \mathrm{M}_{\odot} \end{cases} \tag{3.1}$$

(illustrated in Figure 3.3). This fitting curve offers an observational-driven approach to considering the variation of the convective overshoot parameter $f_{\rm ov}$ as a function of the grid inputs, especially mass (M), using relatively few parameters. However, we emphasize that this formula was calibrated based on the sample from Claret and Torres (2018). Consequently, its numerical parameters need to be recalculated for different samples. This is addressed in the following sections, where we revisit the interpolation errors at the transition between models with radiative cores and models with convective cores.

3.2. The Convective Overshoot Problem in our Grid

To understand the origin of the large interpolation errors observed for the evolutionary track with $M = 1.175\ \mathrm{M}_{\odot}$ (in Figure 2.11), we now address the results from the perspective of a fixed radial order and multiple mass tracks. To that end, we compute an average offset similar to that presented in Equation 2.12, but now defined as a weighted mean of all absolute interpolated errors, $|\delta\nu_{i,\ell,n,M}|$, for a radial order of a mode on all interpolated models of all evolutionary tracks of the grid, as given by the equation

$$\mu_{\ell,n} = \frac{1}{\sum_M \sum_i w_{i,M}} \sum_M \sum_i |\delta\nu_{i,\ell,n,M}| w_{i,M} \tag{3.2}$$

where

$$w_{i,M} = (\tau_{\mathrm{scaled},i+1} - \tau_{\mathrm{scaled},i-1})/2, \tag{3.3}$$

where the sum in M is over all the evolutionary tracks of the grid considered for a radial order, while the sum in i is over all the models for a given radial order and evolutionary track. In these following sections, we drop the indices ℓ and n in the quantity $\mu_{\ell,n}$ and the indices i, M in $\delta\nu_{i,\ell,n,M}$.

Figure 3.4 presents the frequency interpolation errors for dipolar modes of the radial order $n = 11$ as a function of the age proxies $\tau_{\rm scaled}$ and $\rho_{\rm c}$. For the mass track with $M = 1.175$ $\mathrm{M}_{\odot}$, the interpolation errors are not only about an order of magnitude larger than the typical errors found for the other masses, but they are also systematic, being consistently positive

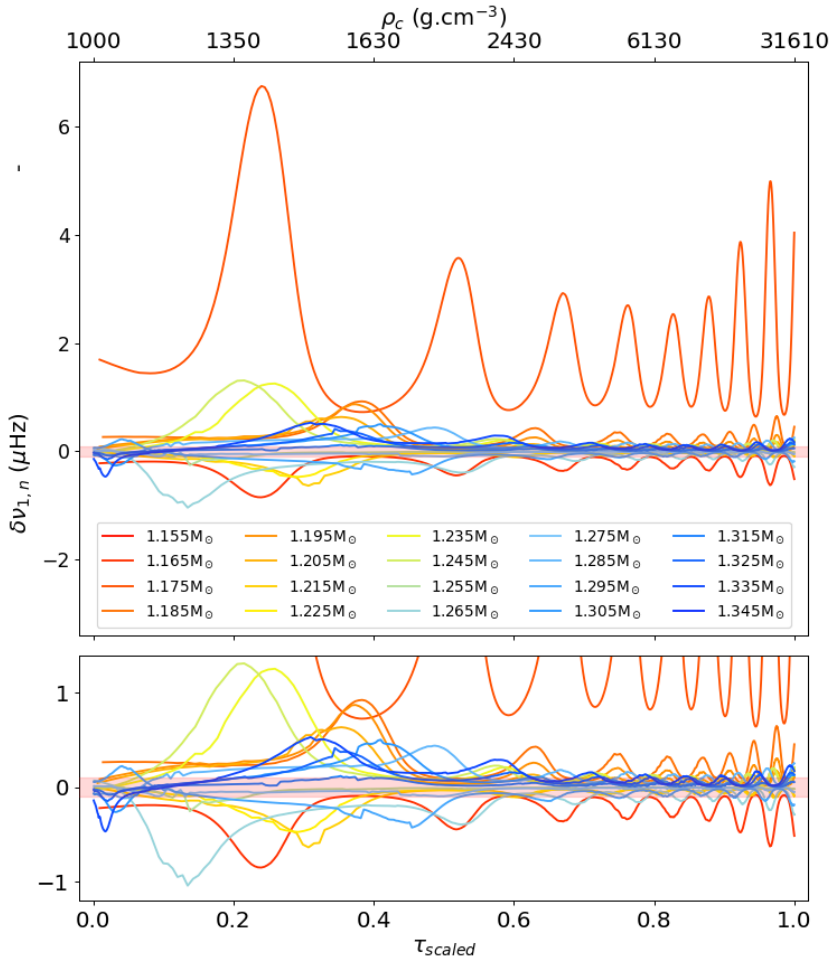


Figure 3.4: Interpolation errors as a function of τ_{scaled} (bottom x-axis) and ρ_c (top x-axis), that resulted from the application of the full interpolation algorithm (cubic splines along tracks and linear across tracks) across the complete grid. Results are shown for all $\nu_{1,11}$ mode frequencies, when ρ_c is used as the age proxy for interpolation. The transition mass between radiative and convective cores in the MS is 1.175 M$_\odot$ for a choice of f_{ov}=0.01. The bottom subplot zooms in on the results for interpolation from the top plot.

and significant along the entire track. This problem is not restricted to one particular dipole mode. In fact, all modes associated with the mass track with $M = 1.175$ M$_\odot$ exhibit similar large errors, that can be as high as 7.7×10^0 μHz, and average offsets of the order of 1.7×10^0 μHz. This is further illustrated in Figure 3.5, constructed by focusing on a specific evolutionary value of the age proxy ($\rho_c = 16000$ g.cm^{-3}) where the discontinuity is observed for all radial orders between the evolutionary tracks with $M = 1.175$ and 1.180 M$_\odot$.

To explore further aspects of this anomaly, we consider a smaller and denser subgrid of stellar models. This subgrid aims at understanding how increasing the density of evolutionary tracks in a grid of stellar models influences the results of the interpolation methods. It uses the same physics as the main grid (described in Section 2.2), but with different

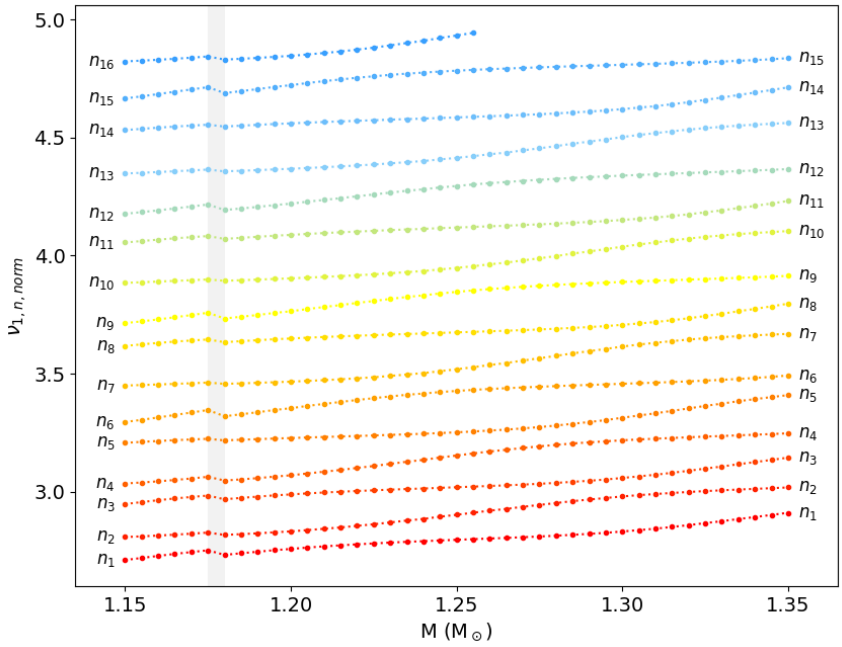


Figure 3.5: Evolution of the ℓ=1 mode frequencies (obtained through interpolation) with mass. Each point represents the frequency of the mode with the indicated radial order for the model at the corresponding mass and at a fixed position in the evolutionary track where ρ_c=16000 g.cm^{-3}.

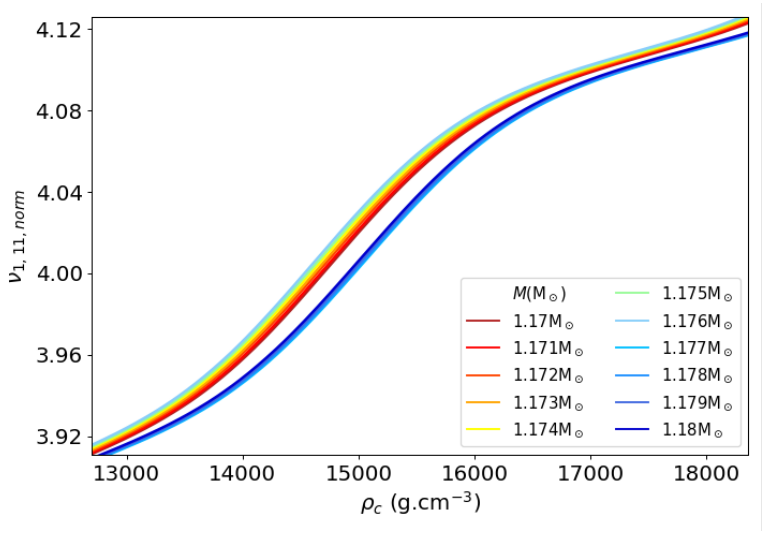


Figure 3.6: Evolution of the $\nu_{1,11,\text{norm}}$ mode frequency along an avoided crossing taking place at central densities between 13000 and 18000 g.cm^{-3}, for models of the first subgrid. The transition mass between radiative and convective cores in the MS is 1.176 M$_\odot$ for this subgrid with $f_{ov} = 0.01$.

mass inputs, with mass values varying between 1.170 and 1.180 M$_\odot$ in steps of 0.001 M$_\odot$.

Figure 3.6 shows the evolution of the mode frequency $\nu_{1,11,\text{norm}}$ with central density ρ_c for the different mass tracks of this subgrid, focusing on a middle stage of the subgiant phase (in the interval between $\rho_c = 13000$ and 18000 g.cm^{-3}, or equivalently, in the interval

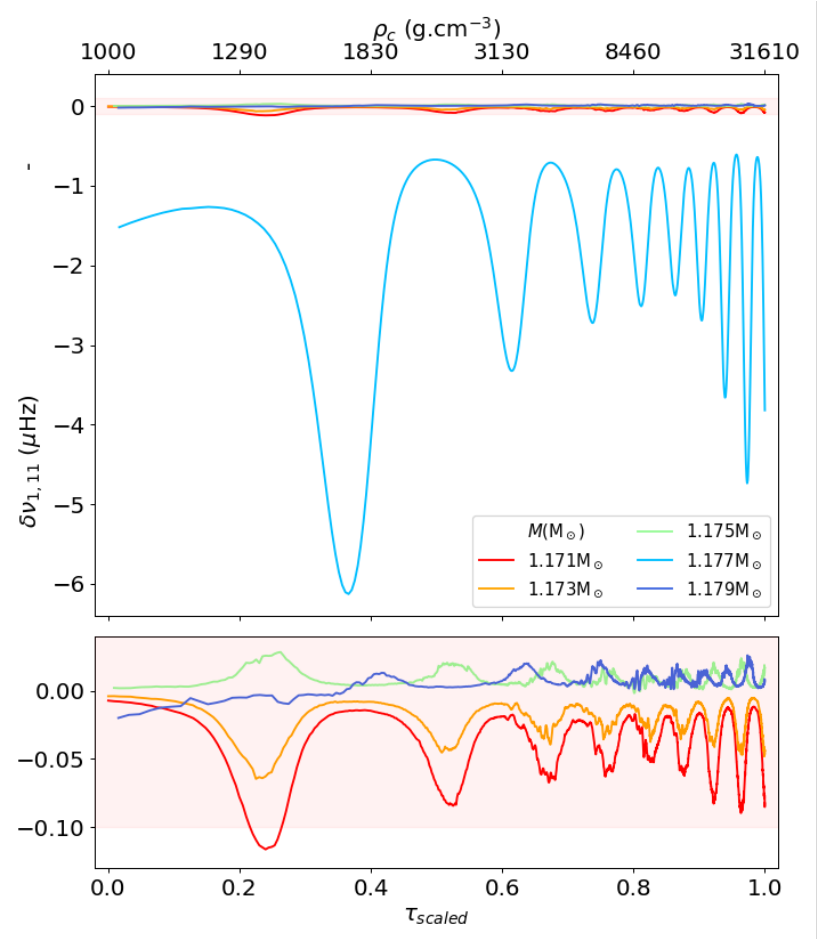


Figure 3.7: Interpolation errors as a function of τ_{scaled} (bottom x-axis) and ρ_c (top x-axis), that resulted from the application of the full interpolation algorithm (cubic splines along tracks and linear across tracks) to the first subgrid (with f_{ov}=0.01). Results are shown for all $\nu_{1,11}$ mode frequencies of the subgrid, when ρ_c is used the age proxy for interpolation. The transition mass between radiative and convective cores in the MS is 1.176 M$_\odot$ for this choice of f_{ov}. The bottom subplot zooms in on the results for interpolation presented in the top plot.

between $\tau_{\text{scaled}} = 0.890$ and 0.925). The initial results show that increasing the grid resolution in mass step exacerbates the problem, as the curves describing the evolution of the mode frequency along the evolutionary tracks with masses 1.176 and 1.177 M$_\odot$ are further apart than those with masses 1.175 and 1.180 M$_\odot$. This indicates that the interpolation problem presented in Figure 3.4 cannot be resolved by simply increasing the grid resolution in a specific region of the parameter space. This is confirmed in Figure 3.7, where the results of applying the full interpolation algorithm to this denser subgrid, specifically to the track with $M = 1.177$ M$_\odot$, show no clear improvement.

Thus, the persistence of large interpolation errors around $M = 1.175$ M$_\odot$ shows that the problem cannot be resolved by grid refinement alone, which motivates the introduction of new subgrids aimed at testing the underlying stellar physics.

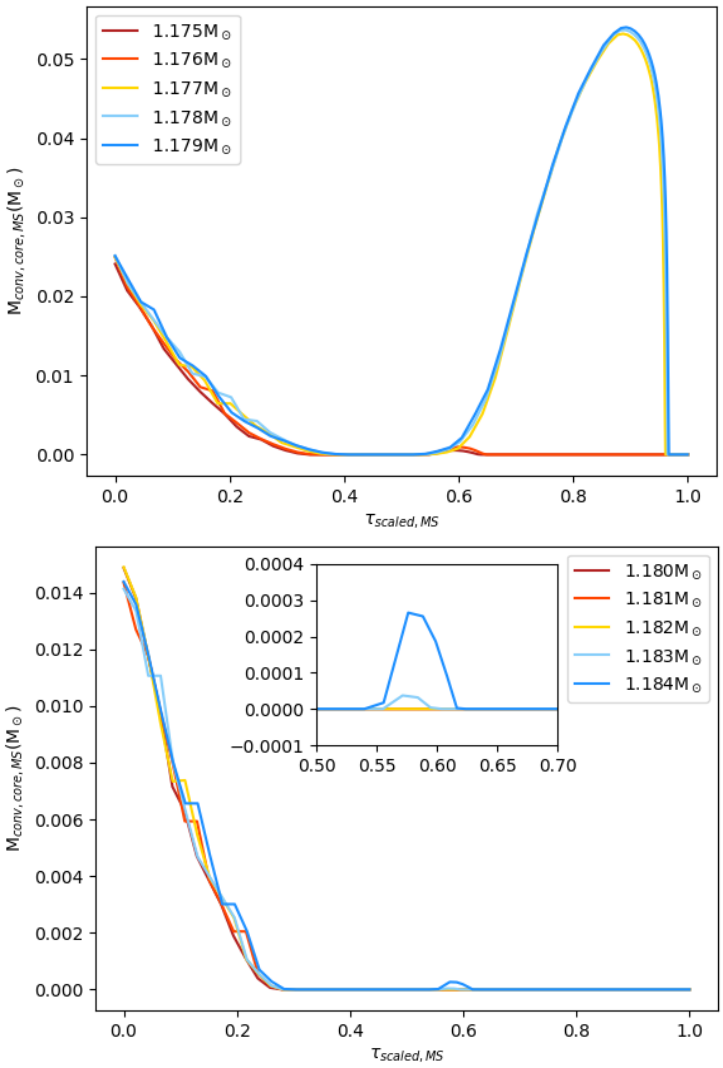


Figure 3.8: Evolution of the mass of the convective core during the MS phase ($M_{\text{conv core,MS}}$) as a function of the scaled age of the MS ($\tau_{\text{scaled,MS}}$), for the different mass inputs of our subgrids, with $f_{\text{ov}} = 0.01$ (left) and $f_{\text{ov}} = 0.00$ (right). The inset in the right plot presents a zoomed-in view of the results.

3.3. Discussing Solutions for the Convective Overshoot Problem

Considering the dependence of the avoided crossings on the core conditions (discussed in Section 1.4.2), we conjecture that the discontinuity observed in the behavior of the mode frequencies with mass could be a result of a change in the physical properties of the core. Indeed, the mass values at which the large interpolation errors occur are typically associated with the transition from stars with a radiative core to stars with a convective core during their MS. This conjecture is supported by the evolution of the convective core mass in our subgrid, as seen on the left plot of Figure 3.8. We observe that for evolutionary tracks with $M \leq 1.176\ \text{M}_{\odot}$, the mass of the convective core is non-zero at the beginning of the MS, but it quickly decreases to zero, remaining so until the end of the MS. However, for

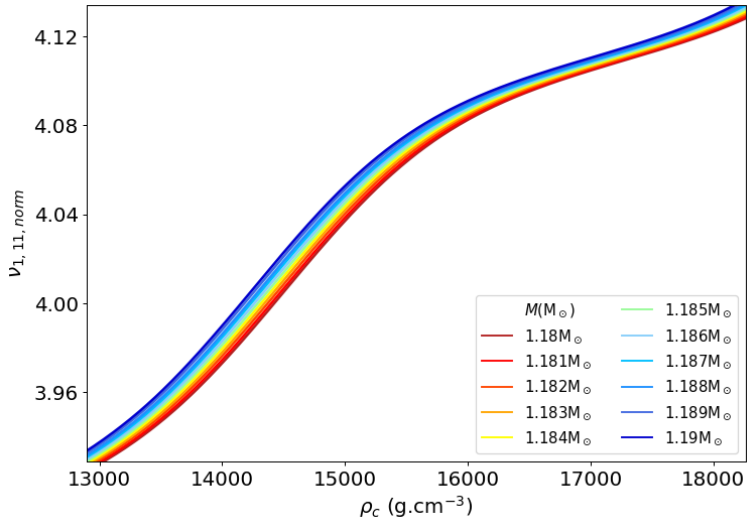


Figure 3.9: Evolution of the $\nu_{1,11,\text{norm}}$ mode frequency along an avoided crossing taking place at central densities between 13000 and 18000 g.cm^{-3}, for the models of the stellar subgrid with f_{ov}=0.00. The transition mass, between radiative and convective cores in the MS, is 1.182 M$_\odot$ for this choice of f_{ov}.

$M >$ 1.176 M$_\odot$, the convective core mass remains above zero for most of the MS stage, highlighting a possible relation between the structure of the star during the MS phase and the systematic interpolation errors observed during the subgiant phase.

To investigate the relation between the core structure and the interpolation errors, and to explore other ways of mitigating this problem, we analyse the impact of the adopted core physics, particularly convective overshoot. For that, we consider a second subgrid, with similar physics to the main grid, but with the convective overshoot turned off, i.e., $f_{\text{ov}} =$ 0.00. This adjustment implies a change in the transitional mass at which stars begin to develop a convective core. Thus, we consider different mass inputs for this subgrid, with values varying between 1.180 and 1.190 M$_\odot$ in steps of 0.001 M$_\odot$, as we observed that the transitional mass for the case with no convective overshoot lies between $M =$ 1.182 and 1.183 M$_\odot$ (as shown in the right panel in Figure 3.8).

Figure 3.9 shows the evolution of the mode frequency $\nu_{1,11,\text{norm}}$ with central density ρ_c for the mass tracks of the subgrid with no convective core overshoot, zoomed in on the same phase of the subgiant evolution as Figure 3.6. The discontinuity essentially disappears when f_{ov} is set to zero, which shows that the cause for the discontinuity is not the appearance of a sustained convective core during the MS *per se*, but rather an abrupt change in the core conditions resulting from the overshoot properties considered in the original grid. The change in the energy transport during the MS - together with an enlargement of the mixed region by overshoot - leads to an abrupt change in the central temperature,

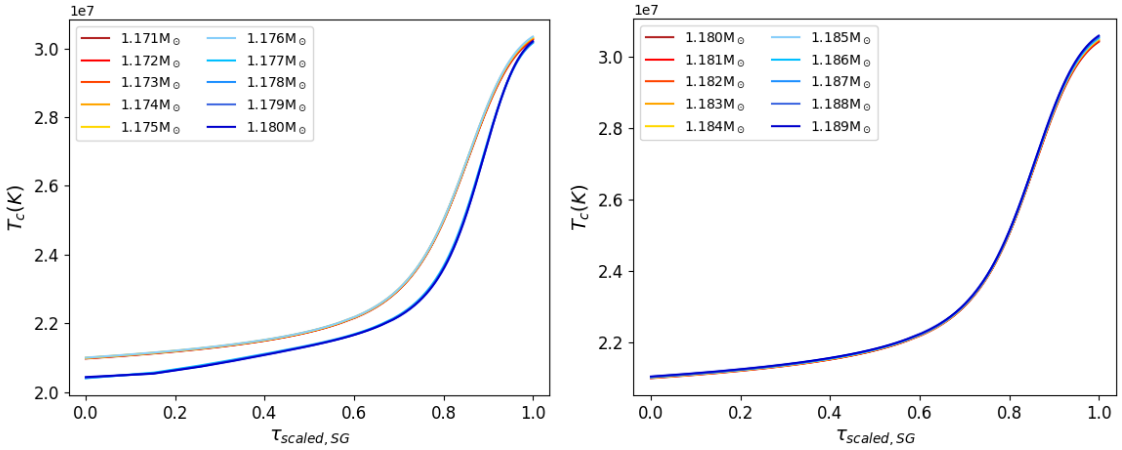


Figure 3.10: Evolution of the central temperature, T_c, with $\tau_{scaled,SG}$ (calculated for the subgiant phase) for the two subgrids discussed in this section, with $f_{ov} = 0.01$ (left) and $f_{ov} = 0.00$ (right).

T_c, when comparing models at fixed ρ_c in the two regimes, as depicted in the left panel of Figure 3.10. From Equation 1.62 (discussed in Section 1.4.2), at fixed ρ_c, we find out that $N^2 \propto T_c^{-1}$, which illustrates how abrupt changes in T_c affect the frequencies of the mixed modes, and consequently the interpolation results.

The results of applying our interpolation method to the second subgrid are shown in Figure 3.11. In this case, the interpolation errors associated with the transitional mass (which corresponds to the interpolated mass track with $M = 1.183$ $M_\odot$) are no longer unusually large, with a maximum error of 8.9×10^{-2} μHz, below the 0.1 μHz threshold.

Ignoring the mixing from the convective core into the radiative layers is useful to identify the origin of the large interpolation errors. However, this is not an adequate way to mitigate the interpolation problem in this region of the parameter space, since overshoot describes important physics that we know affect stellar structure through various phases of evolution. Above all, these results show the importance of either ensuring that the grid is built such as to minimize the impact of abrupt structural changes on interpolation, or, when there is no adequate way of doing that, accounting for the additional errors that may result from interpolation.

In Section 3.1, we discussed the observational evidence for a mass-dependent overshoot in the mass regime where the core changes from radiative to convective during the MS. Specifically, several works reported values of f_{ov} slowly increasing from zero, proportionally to stellar mass. Such mass dependence is expected to smooth the transition of the core properties, compared to adopting a fixed value of f_{ov} as in our original grid. With this

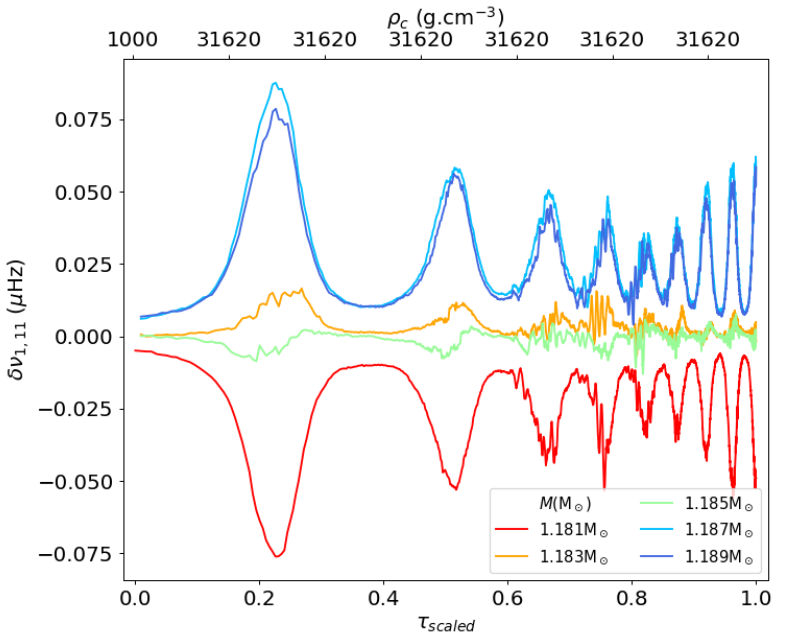


Figure 3.11: Interpolation errors as a function of τ_{scaled} (bottom x-axis) and ρ_c (top x-axis) that resulted from the application of the full interpolation algorithm (cubic splines along tracks and linear across tracks) to the second subgrid (with $f_{ov} = 0.00$). Results are shown for all $\nu_{1,11}$ mode frequencies of the subgrid, when ρ_c is used as the age proxy for interpolation. The transition mass between radiative and convective cores in the MS is 1.182 M$_\odot$ for this choice of f_{ov}.

in mind, we constructed a third subgrid with similar physics to the main grid, but with convective overshoot f_{ov} varying as a function of stellar mass M, according to the following variation of Equation 3.1

$$f_{ov} = \begin{cases} 0, \text{ if } M \leq 1.18\text{M}_\odot \\ \frac{0.02013}{1+e^{-5.5(M-1.45)}} - 0.00373, \text{ if } M > 1.18\text{M}_\odot \end{cases} . \tag{3.4}$$

In the above, the limits of the two branches and the term values in the lower branch of the equation were adjusted so as to agree with the mass at which MS models preceding the models in our grid change from having a radiative core to having a convective core, namely, $M = 1.18$ M$_\odot$. In this case, mass values for the tracks of the grid vary between 1.150 and 1.220 M$_\odot$ in steps of 0.005 M$_\odot$*.

The results of applying our interpolation method to the third subgrid are shown in Figure 3.12. As with the second grid, the large interpolation errors also disappear in this case. We note that the subgrid of models including a mass-dependent value of f_{ov} considers a

*We defined this range of masses as, according to Equation 3.4, f_{ov} increases approximately linearly with mass until $M \sim 2.00$ M$_\odot$, after which it becomes approximately constant. This limit lies well outside the mass range considered in the initial grid. Therefore, we focused on the region where the discontinuity is most pronounced.

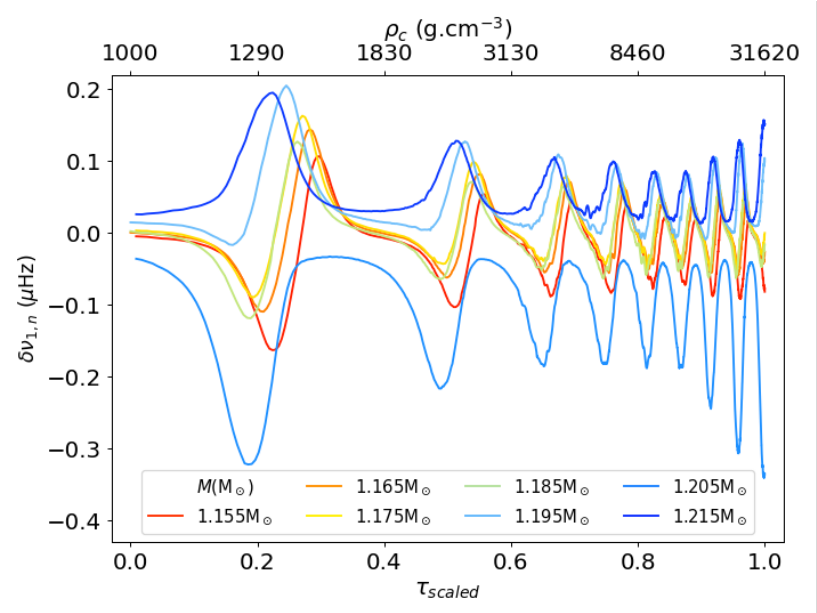


Figure 3.12: Interpolation errors as a function of τ_{scaled} (bottom x-axis) and ρ_c (top x-axis) that resulted from the application of the full interpolation algorithm (cubic splines along tracks and linear across tracks) to the third subgrid (with $f_{\text{ov}}(M)$). Results are shown for all $\nu_{1,11}$ mode frequencies of this subgrid, when ρ_c is the age proxy for interpolation.

step in mass similar to that of the original grid, thus more typically used in modelling grids. Therefore, the interpolation errors found for the transitional mass ($M = 1.175$ M$_\odot$ in this case) in this subgrid correspond to what may be expected in a typical grid of models. As the errors are of the same order of magnitude as the interpolation errors obtained for the other interpolated mass tracks, we conclude that adopting an observationally-driven mass dependence for the overshoot parameter mitigates the problem of interpolation across the mass regime where sustained convective cores appear in the MS.

3.4. Conclusions

The accuracy of interpolation is expected to be affected by abrupt changes of the mode frequencies across the parameter space. The study presented in Chapter 2 highlighted the large, systematic interpolation errors associated with the evolutionary track with $M =$ 1.175 M$_\odot$, prompting us to investigate their origin and implications for the construction of a model grid. We found that the errors likely stem from variations in core properties at specific mass transitions, particularly between stars with convective and radiative cores during their MS.

From the analysis of multiple (sub)grids, we found out that turning off convective overshoot (i.e., $f_{\text{ov}} = 0.00$) eliminates these systematic errors, demonstrating that overshoot

plays a key role in intensifying the abrupt changes in the core conditions. Given that turning off convective overshoot altogether is not a physically viable solution, we explored an observationally-driven alternative, which points to a smooth transition in the amount of overshoot when crossing the mass range where stars in the MS start to have a sustainable convective core. We showed that implementing a mass-dependent overshoot parameter, $f_{\mathrm{ov}}(M)$, smooths the transition between stars with radiative cores and stars with convective cores, reducing interpolation errors to values comparable with those observed in other mass tracks within the same grid.

Convective overshoot is not the only case that can lead to potential abrupt physical transitions in stellar model grids. The options made regarding the treatment of diffusion of chemical elements can also impact such models, since grids are often constructed so that diffusion is turned off at a given mass (Nsamba et al., 2025). Therefore, this chapter emphasizes that special attention should be given to these transitions when building any grid of stellar models, and that interpolation of the grid should be carefully tested before applying the grid to the modelling of stars.

4. A Mixed Mode Motivated Interpolation Algorithm

4.1. Introduction

As previously established, the description of the mixed modes that best fits our purposes considers the evolution of their frequencies as a function of central density, ρ_c (consistently with the theoretical framework presented in Section 1.4.2 and the results discussed in Chapter 2). Under this framework, the pronounced non-linearity of the mixed mode frequency curves becomes more systematically aligned, grouping together different curves that share the same mode degree ℓ and radial order n for different - but close in mass - evolutionary tracks (as illustrated in Figure 2.10). This reformulation has led to a significant improvement in the performance of our interpolation algorithms, even though the intrinsic non-linearity of the mixed modes continues to prevent us from obtaining results within the established accuracy.

The still relatively large errors in the interpolated frequencies occur for modes near the avoided crossings, where the evolution of the mode frequencies with any of the studied age proxies is highly non-linear. Recognizing this, we attempt in this chapter to design a new age proxy such that the mode frequencies' dependence on the new age proxy stays approximately linear throughout the whole subgiant phase. To that end, we use the asymptotic analysis of mixed modes to build a function whose properties describe well the evolution of a mode frequency both around and away from the avoided crossings.

Under the Jeffreys-Wentzel–Kramers–Brillouin (JWKB) approximation (Unno et al., 1989), eigenvalues can be determined by relating the phase integrals, $\theta = \int k_r \, dr$ (see Equation 1.44), in the p- and g-mode cavities to one another via a characteristic function of the form (see Equation 1.58 in Section 1.4)

$$\tan(\theta_p)\cot(\theta_g) = q, \tag{4.1}$$

where q is the coupling strength, a dimensionless coefficient that measures the strength of the coupling between the p- and g-mode cavities. Following Ong and Gehan (2023),

Equation 4.1 can be reformulated as

$$F(\nu) = \tan\Theta_\mathrm{p} \tan\Theta_\mathrm{g} - q \simeq 0, \tag{4.2}$$

particularly near the eigenvalues of the function $F(\nu)$. Here, Θ_p and Θ_g are given by

$$\Theta_\mathrm{p} = \pi \frac{\nu - \nu_\mathrm{p}}{\Delta\nu}\,, \qquad \Theta_\mathrm{g} = \pi \frac{1/\nu_\mathrm{g} - 1/\nu}{\Delta\Pi_\ell}\,, \tag{4.3}$$

where ν_p and ν_g are the frequencies of the pure p- and g-modes, respectively, $\Delta\nu$ is the large frequency separation (defined in Equation 1.51), and $\Delta\Pi_\ell$ is a characteristic period spacing, defined as

$$\Delta\Pi_\ell = \frac{\Pi_0}{\sqrt{\ell(\ell+1)}} = \frac{2\pi^2}{\sqrt{\ell(\ell+1)}} \left(\int_{r_1}^{r_2} N \frac{dr}{r} \right)^{-1} \sim \Delta(1/\nu_\mathrm{g}). \tag{4.4}$$

From trigonometry, we have that, for any angle Θ in the interval $[0, \pi]$,

$$\tan\Theta = \cot\left(\frac{\pi}{2} - \Theta\right) \Longrightarrow \Theta = \frac{\pi}{2} - \arctan\left(\frac{1}{\tan\Theta}\right), \tag{4.5}$$

where the arctan() function is to be taken in the interval $[-\pi/2, \pi/2]$.

By applying this identity to Equation 4.2, we obtain

$$\Theta_\mathrm{p} = \frac{\pi}{2} - \arctan\left(\frac{\tan\Theta_\mathrm{g}}{q}\right). \tag{4.6}$$

Substituting the expressions from Equation 4.3 into Equation 4.6 yields

$$\pi \frac{\nu - \nu_\mathrm{p}}{\Delta\nu} = \frac{\pi}{2} - \arctan\left(\frac{1}{q} \tan\left(\pi \frac{1/\nu_\mathrm{g} - 1/\nu}{\Delta\Pi_\ell}\right)\right), \tag{4.7}$$

which can be rearranged as

$$\nu = \nu_p + \frac{\Delta\nu}{2} - \frac{\Delta\nu}{\pi} \arctan\left(\frac{1}{q} \tan\left(\pi \frac{1/\nu_\mathrm{g} - 1/\nu}{\Delta\Pi_\ell}\right)\right). \tag{4.8}$$

Equation 4.8 admits two distinct solutions, corresponding to the limits when $\nu \sim \nu_p$ and $\nu \sim \nu_g$. In the first case ($\nu \sim \nu_p$), the condition $1/\nu_\mathrm{g} - 1/\nu_p \sim \Delta\Pi_\ell/2$ sets the argument of tan() function to be $\pi/2$, causing the argument of arctan() function to go to $+\infty$. The last term of Equation 4.8 then reduces to $\Delta\nu/2$, resulting in the initial assumption, $\nu = \nu_p$, thereby recovering the p-modes. In the second case ($\nu \sim \nu_g$), the argument of the tan() function vanishes, thereby eliminating the last term of Equation 4.8. This results in $\nu = \nu_p + \Delta\nu/2$, where we recover the pure g-modes. These limits are illustrated in Figure 4.1, where the $\nu \sim \nu_p$ (p-modes) case is represented by dotted lines, and the $\nu \sim \nu_g$

(g-modes) case by dashed lines.

Near the limit $\nu \sim \nu_g$, where $\tan\Theta_\mathrm{g} \sim \Theta_\mathrm{g}$, we can simplify Equation 4.8 to

$$\nu = \nu_\mathrm{p} + \frac{\Delta\nu}{2} - \frac{\Delta\nu}{\pi}\arctan\left(\frac{\pi}{q\Delta\Pi_\ell}\delta(1/\nu)\right), \tag{4.9}$$

where $\delta(1/\nu) \equiv 1/\nu_\mathrm{g} - 1/\nu$.

With the expression above, we recover the pure g-mode frequencies when $\delta(1/\nu) \to 0$ and also approximately recover the pure p-mode frequencies when $\delta(1/\nu) \gtrsim \Delta\Pi_\ell$. This way, except possibly within a small transition region far from the points where the mixed modes approach either pure p- or g- mode behavior, the mixed mode frequency around a given avoided crossing taking place at $\rho_\mathrm{c} = \rho_{\mathrm{c},0}$ can be written as a perturbation to the associated pure p-mode frequency approximately as

$$\nu(\rho_\mathrm{c}) = \nu_\mathrm{p} + \delta\nu_p = \nu_\mathrm{p} + \frac{\Delta\nu}{2} + \frac{\Delta\nu}{\pi}\arctan\left(\frac{\pi}{q\Delta\Pi_\ell}\frac{-\delta(1/\nu)}{\delta\rho_\mathrm{c}}(\rho_\mathrm{c} - \rho_{\mathrm{c},0})\right), \tag{4.10}$$

where $\delta\nu_p$ is the variation with respect to the pure p-mode frequency caused by the coupling with the associated pure g-mode. In the normalized form, this becomes

$$\begin{aligned}\nu_\mathrm{norm} &= \nu_{\mathrm{p,norm}} + \frac{\Delta\nu_\mathrm{norm}}{2} + \frac{\Delta\nu_\mathrm{norm}}{\pi}\arctan\left(\frac{\pi}{q\Delta\Pi_{\ell,\mathrm{norm}}}\frac{-\delta(1/\nu_\mathrm{norm})}{\delta\rho_\mathrm{c}}(\rho_\mathrm{c} - \rho_{\mathrm{c},0})\right) \\ &\equiv A + B(\pi/2 + \arctan(C(\rho_c - D))),\end{aligned} \tag{4.11}$$

where the subscript *norm* indicates that the quantity has been normalized by dividing or multiplying by the factor $\sqrt{GM/R^3}$, depending on whether it represents a frequency or period, respectively. The fitting parameters A, B, C and D are physically defined as

$$A = \nu_{\mathrm{p,norm}}; \quad B = \frac{\Delta\nu_\mathrm{norm}}{\pi}; \quad C = \frac{\pi}{q\Delta\Pi_{\ell,\mathrm{norm}}}\frac{-\delta(1/\nu_\mathrm{norm})}{\delta\rho_\mathrm{c}}; \quad D = \rho_{\mathrm{c},0}. \tag{4.12}$$

The parametrization presented by Equation 4.11 is valid to describe the evolution of a single avoided crossing, occurring at a given central density, here labelled $\rho_{\mathrm{c},0}$. To model the complete evolution of an $\ell = 1$ mode during the subgiant phase - a result of a sequence of couplings between pure p- and g-modes, as illustrated in Figure 4.1 - we can expand the original fitting function (Equation 4.11) and write

$$\nu_\mathrm{norm}(\rho_\mathrm{c}) = A + \sum_{i=0}^{I} B_i\left(\frac{\pi}{2} + \arctan\left(C_i(\rho_\mathrm{c} - D_i)\right)\right), \tag{4.13}$$

where A is the normalized frequency of the first p-mode in the series and the parameters B_i, C_i and D_i are given by the expressions presented in Equation 4.12. Here, i is an

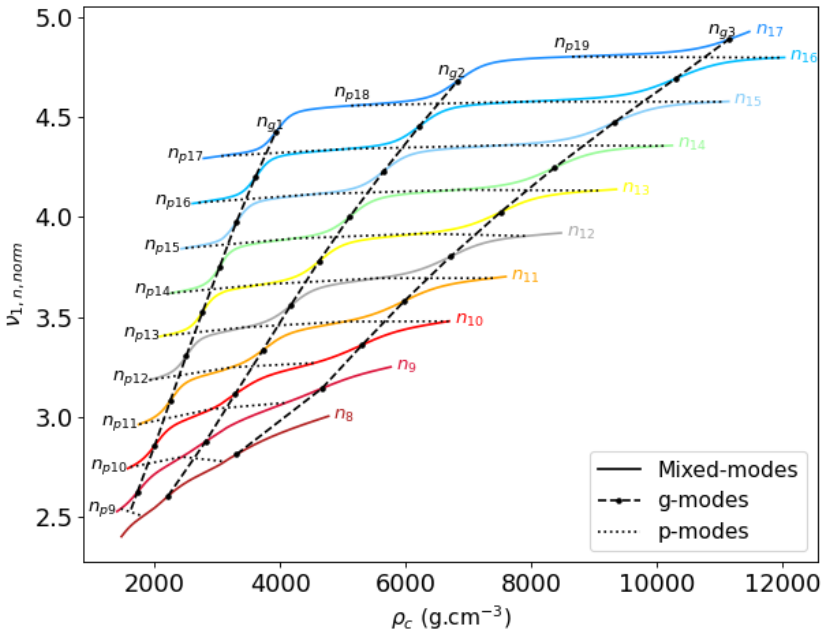


Figure 4.1: Evolution of the $\ell = 1$ frequency modes (colored lines), along with the inferred trajectories of the corresponding pure g modes (estimated using the centres of each avoided crossing; dashed lines) and pure p modes (estimated from the centres of each linear region of evolution, between avoided crossings; dotted lines) as a function of ρ_c, for a track with $M = 1.245$ M$_\odot$.

index representing each avoided crossing in a series, and I denotes the total number of avoided crossings identified by the fitting algorithm to best match the frequency data of each mixed mode being parametrised.

Building upon Equation 4.13, it is possible to reparametrize the evolution of the mode frequencies in terms of a new variable - a new age proxy - with respect to which the evolution is approximately linear. In that way, we may hope to develop more sophisticated interpolation algorithms (compared to those discussed in previous chapters) that may more effectively meet the strict accuracy requirements established by space missions like PLATO. These methods are examined in the following sections.

4.2. Interpolation using $\varphi(\rho_c)$ as an Alternative Age Proxy

Building upon the theoretical framework discussed in the previous section, we identify a promising avenue of investigation in the parametrization of the $\ell = 1$ frequency modes (in their normalized form) of the stellar grid. By employing Equation 4.13, that results from the parametrization of each frequency curve, the central density parameter, ρ_c, may be

transformed into a new variable, $\varphi(\rho_c)$, according to

$$\varphi(\rho_c) = A + \sum_{i=0}^{I} B_i \left(\frac{\pi}{2} + \arctan\left(C_i(\rho_c - D_i)\right) \right), \tag{4.14}$$

where the parameters are optimized for each frequency curve of a dipolar mode. In this formulation, the evolution of the frequencies as a function of $\varphi(\rho_c)$ becomes approximately linear, and the models - originally computed at a constant ρ_c step - become unevenly distributed in the new variable. They therefore contribute with unequal weights to the interpolation process when interpolation across tracks it taken at fixed values of $\varphi(\rho_c)$. Accordingly, this new variable may serve as a better proxy for stellar age in interpolation schemes. In this section, we evaluate the degree to which each frequency curve can be linearized when expressed as a function of the new variable and assess the performance of the interpolation algorithms (presented in previous chapters) when employing $\varphi(\rho_c)$ as the age proxy.

For the optimization of the parameters of each fitting function for each frequency curve, we employed the `scipy.optimize.curve_fit()` function from the Python SciPy library, using its default conditions. Beyond the basic inputs, we also provide initial guesses for each fitting parameter. Specifically, for parameter A, we take the normalized frequency mode $\nu_{\ell,n,\mathrm{norm}}$ near the TAMS, just prior to the first avoided crossing; for the parameters B_i, we take the normalized large frequency separation at each avoided crossing divided by π, $\Delta\nu_{\mathrm{norm},i}/\pi$; and for the parameters D_i, we take the points along the frequency curve where the second derivative changes sign from positive to negative. By contrast, the initial guesses for C_i, which controls the horizontal scaling of the function, are more challenging to determine, with their initial estimations requiring a trial-and-error approach.

We use an algorithm based on the function defined by Equation 4.14 and the aforementioned parameter initial guesses to optimize the fitting parameters pertaining to the evolution of the frequency of each mode along each frequency curve to the frequency data of our grid. The fits then allow us to determine how to transform from ρ_c to the new variable, $\varphi(\rho_c)$. Importantly, we note that this transformation depends on the mode (ℓ, n) considered. The fitting procedure is implemented by imposing a threshold condition, where the residuals - i.e. the difference between the theoretical mode frequencies calculated in our grid of models and the corresponding value estimated from the optimized fitting function

for each model j* - are given by

$$\partial\nu_{\ell,n,j} = \nu_{\ell,n,j,\text{parametrized}} - \nu_{\ell,n,j,\text{theoretical}}, \tag{4.15}$$

and we aim to constrain them to remain below 0.005 (in normalized frequency units, or, equivalently, below $0.005 \times \sqrt{GM/R^3}$, in μHz). For a stellar model with $M = 1.245$ M$_\odot$, this constraint allows frequency residuals to range from 1.50 μHz (near the TAMS) to 0.77 μHz (near the TASG). We note that this value is not directly related to the interpolation errors. It simply establishes how close to linear will the true evolution of the mode frequencies be, when expressed as function of the new age proxy (a zero residual would correspond to an exact linear evolution).

The results of this process for all $\nu_{1,11,\text{norm}}$ frequency modes of the stellar grid are presented in Figures 4.2 and 4.3. The fitting procedure, shown in Figure 4.2, performs as intended, with the frequency curves becoming quasi-linear when expressed as a function of $\varphi(\rho_c)$, as shown in the top plot of Figure 4.3. This is confirmed by the fact that the vast majority of the residuals fall below the established threshold, as shown in the bottom plot of Figure 4.3.

The results of the interpolation algorithm, which considers cubic splines along tracks and linear interpolation across tracks, and uses $\varphi(\rho_c)$ as the age proxy, are presented in Figure 4.4 (left plot) for all $\nu_{1,11}$ frequency modes of the stellar grid. When comparing these results with those obtained from interpolation using ρ_c as the age proxy (shown in the right plot of Figure 4.4), we find that the interpolation errors associated with the new variable are about an order of magnitude smaller than those obtained using ρ_c as the age proxy. This highlights the effectiveness of the proposed approach in achieving the desired accuracy. Indeed, in most cases, we find that the errors are significantly smaller than the typical observational uncertainties ($\sim$0.1 μHz). Exceptions are seen only at the beginning and at the end of the subgiant evolution, where the errors for a few models are comparable to this accuracy threshold.

It is worth noting that the interpolation errors remain within the required accuracy when using this method also for the stellar mass located at the transition where the core becomes convective (discussed in Chapter 3). As shown in Figure 4.5, the evolution of the frequency mode associated with the transition mass of our grid ($M = 1.175$ M$_\odot$) did not fall between the frequency curves associated with the respective adjacent masses ($M =$

*Here, the index j identifies a model within an evolutionary track in our grid, as in Chapter 2. It should not be confused with the index i used in the parameters above for the identification of avoided crossings.

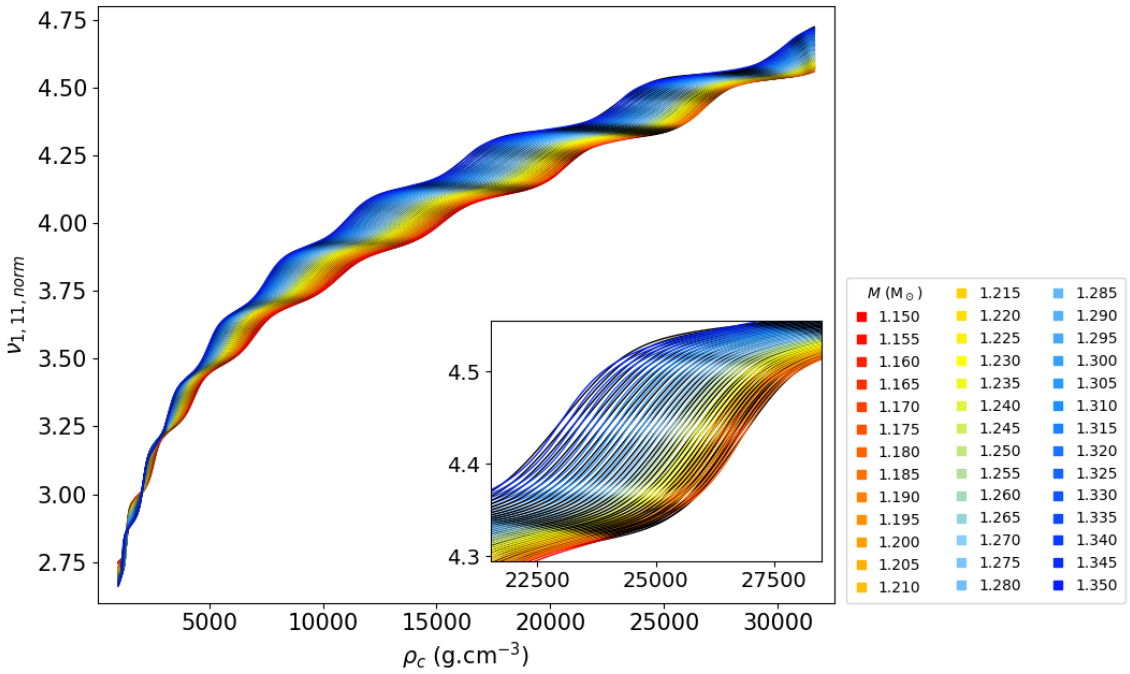


Figure 4.2: Evolution of the $\nu_{1,11,\text{norm}}$ frequency modes, expressed as a function of ρ_c (black lines), and the corresponding estimated fitting functions for each mass (coloured lines), for all evolutionary tracks of the stellar grid introduced in Chapter 2. The inset panel presents a zoomed-in view to help distinguish between the black and coloured lines.

1.170 and 1.180 $M_\odot$) when described as a function of ρ_c. However, when expressed as a function of the new parameter $\varphi(\rho_c)$, it becomes located in-between them, which explains the improved interpolation results seen in Figure 4.4.

The results illustrated in Figure 4.4 compare the interpolated frequencies with the true frequencies obtained from models that are part of the evolutionary track that we assume not to have. While the results show that the interpolation is significantly more accurate when the new variable is used as age proxy, they do not highlight a difficulty inherent to the use of this new age proxy, which we now attempt to explain.

The stretching of the mode frequency evolution, through the change of variable from ρ_c to $\varphi(\rho_c)$, is specific for each mass and radial order. Therefore, different oscillation modes from a single model in the parameter space $[M, \rho_c]$ occupy different points in the parameter space $[M, \varphi(\rho_c)]$. If we were to explore directly the converted parameter space - by drawing pairs of M and $\varphi(\rho_c)$ - and two or more mode frequencies were to be fitted simultaneously, a problem would emerge. Each mode frequency in our underlying true star is converted to a different point in the parameter space $[M, \varphi(\rho_c)]$ through a function that is unknown *a priori*. Therefore, the simultaneous fit of several model frequencies to

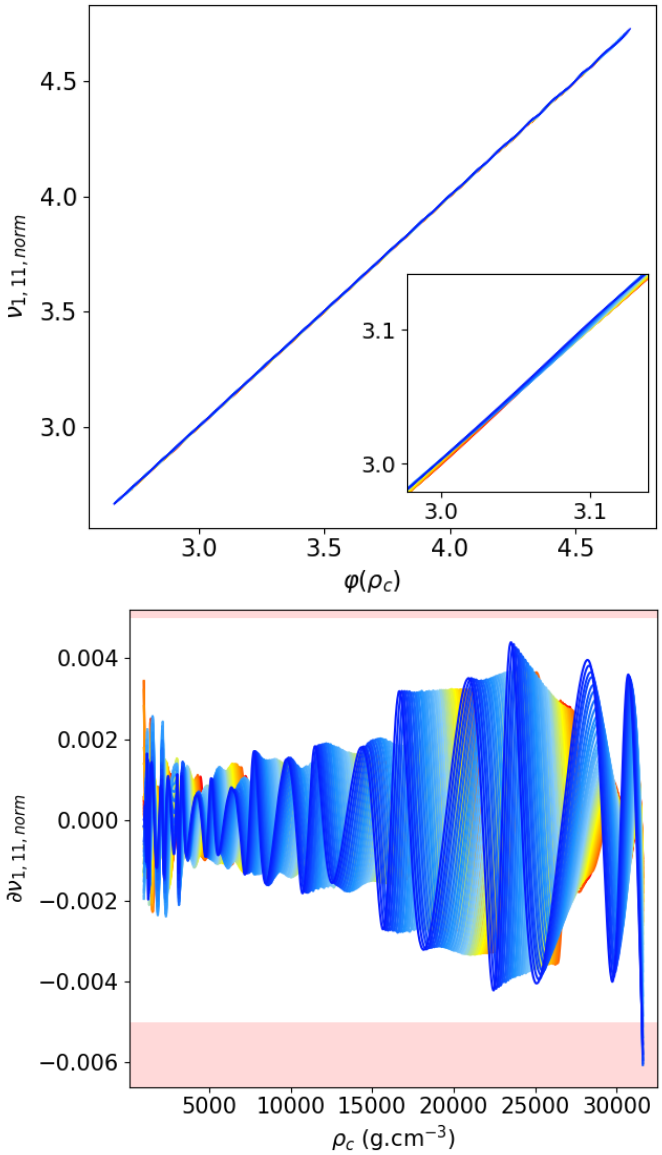


Figure 4.3: Results of the variable transformation algorithm described in the text, shown for all $\nu_{1,11,\text{norm}}$ frequency modes of the stellar grid introduced in Chapter 2. The frequency curves, initially expressed as a function of ρ_c (shown in Figure 4.2), become approximately linear when reparametrized in terms of the new variable $\varphi(\rho_c)$ (top). The residuals from the fitting procedure, determined according to Equation 4.15, are displayed in the bottom panel. The white band establishes the threshold of the fitting residuals, which should not exceed 0.005. The inset on the top panel presents a zoomed-in view. The coloured lines in each plot represent the mass values indicated in Figure 4.2.

the observations in the new parameter space would require the combined exploitation of several parts of the new parameter space, under the constraint that the stellar parameters (mass, age) are the same - because all observed modes emerge from the same star. Moreover, it is unclear how we would then interpolate classical observables (e.g., T_{eff}) to compare with the observations, because each mode frequency would be interpolated from a specific group of grid models - presumably the closest models in the converted parameter space - and the group of models would not necessarily be the same (i.e., have

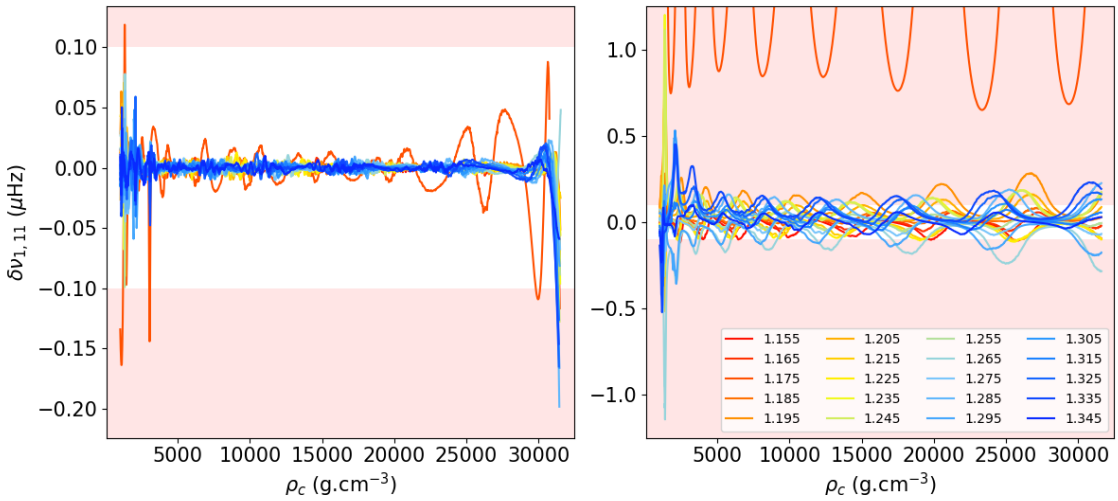


Figure 4.4: Interpolation errors resulting from the full interpolation algorithm (considering cubic splines along tracks and linear interpolation across tracks) as a function of ρ_c, for all $\nu_{1,11}$ frequency modes in the stellar grid. The left plot displays the results when the new variable $\varphi(\rho_c)$ is used as the age proxy, while the right plot shows the results when ρ_c is used as the age proxy instead. The error function that appears truncated at the top of the right panel corresponds to the mass track with M=1.175 $M_\odot$, the problematic case discussed in Chapter 3. In both plots, the white band indicates the typical range of observational errors, establishing the target threshold that our interpolation errors should not exceed.

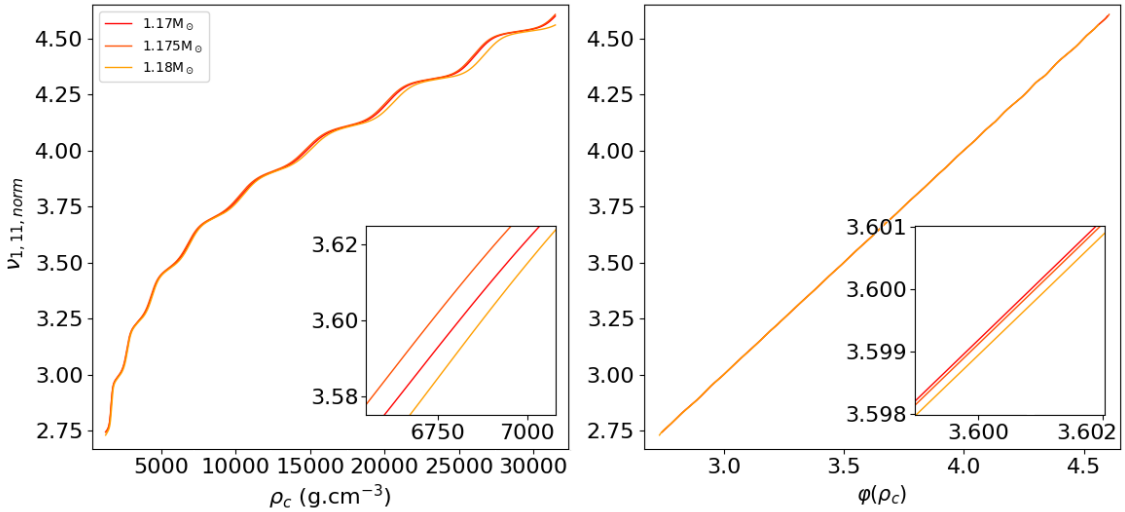


Figure 4.5: Evolution of the frequency modes $\nu_{1,11,\text{norm}}$ as a function of ρ_c (left) and $\varphi(\rho_c)$ (right) for the masses near the transition where the core becomes convective. The insets in each panel present zoomed-in views.

the same mass and age) for the different modes. It is unclear if such a complex approach would succeed or would be useful for more realistic grids, exploring a larger number of parameters. The alternative is to explore instead the original parameter space, by drawing models in the [M, ρ_c] parameter space, and convert these, as well as the model grid, to the new parameter space [M, $\varphi(\rho_c)$]. The interpolation of the classical observables would

proceed in the original parameter space while the interpolation of the different frequencies would take place in the new parameter space, for each single, well-defined model.

The process proposed above relies on the assumption that the transformation functions are available, not only for the evolutionary tracks in the stellar grid used in the interpolation, but also for the evolutionary tracks that contain the models that we want to interpolate for. In fact, such knowledge was required when computing the errors shown in the left panel of Figure 4.4. In practice, when working with real data, the evolutionary tracks containing the models that we want to interpolate for are not known because they are not part of the stellar grid. As a result, the functions required to convert the models whose frequencies we want to know between the two parameter spaces are not available.

Thus, to adequately test the benefits of the new age proxy, we need to consider a more realistic approach in which we know the transformation functions for the models in the grid, but not for the real star (or for any model randomly drawn during the optimization process, e.g., through an MCMC procedure). This requires us to develop a method for estimating the unknown fitting functions associated with any new model that may be drawn by the optimization algorithm. To estimate these unknown fitting functions, we first interpolated the corresponding fitting parameters (A, B_i, C_i, and D_i) from those determined for adjacent evolutionary tracks in the stellar grid, for which the fitting functions can still be obtained using the fitting procedure described in this section. With those parameters in hand, we then use Equation 4.1 to derive the corresponding functions.

In Figure 4.6, we compare the residuals from the transformation procedure, determined using Equation 4.15 (left panels) resulting from the variable transformation and the interpolation algorithms applied to all $\nu_{1,11}$ frequency modes of the grid. These results correspond to two scenarios: one in which all fitting functions are derived directly from the known evolutionary tracks, hence giving us access to the conversion from [M,ρ_c] to [M,$\varphi(\rho_c)$] for all models, including those we want to interpolate for (top row; same as in Figures 4.2-4.4), and another in which the fitting functions for the evolutionary tracks that contain the models we want to interpolate for are unknown *a priori* and have to be derived by interpolating the parameters A, B_i, C_i and D_i, as explained before (bottom row).

Although the residuals are kept below the previously imposed threshold (0.005, in normalized frequency)*, we note a clear difference in the mass-to-mass variations, with the first

*The only exception occurs at a single mass value, $M = 1.175$ M$_\odot$, which is already expected since the stellar grid used here is the same from Chapter 2, where the convective overshoot problem discussed in Chapter 3 is still present.

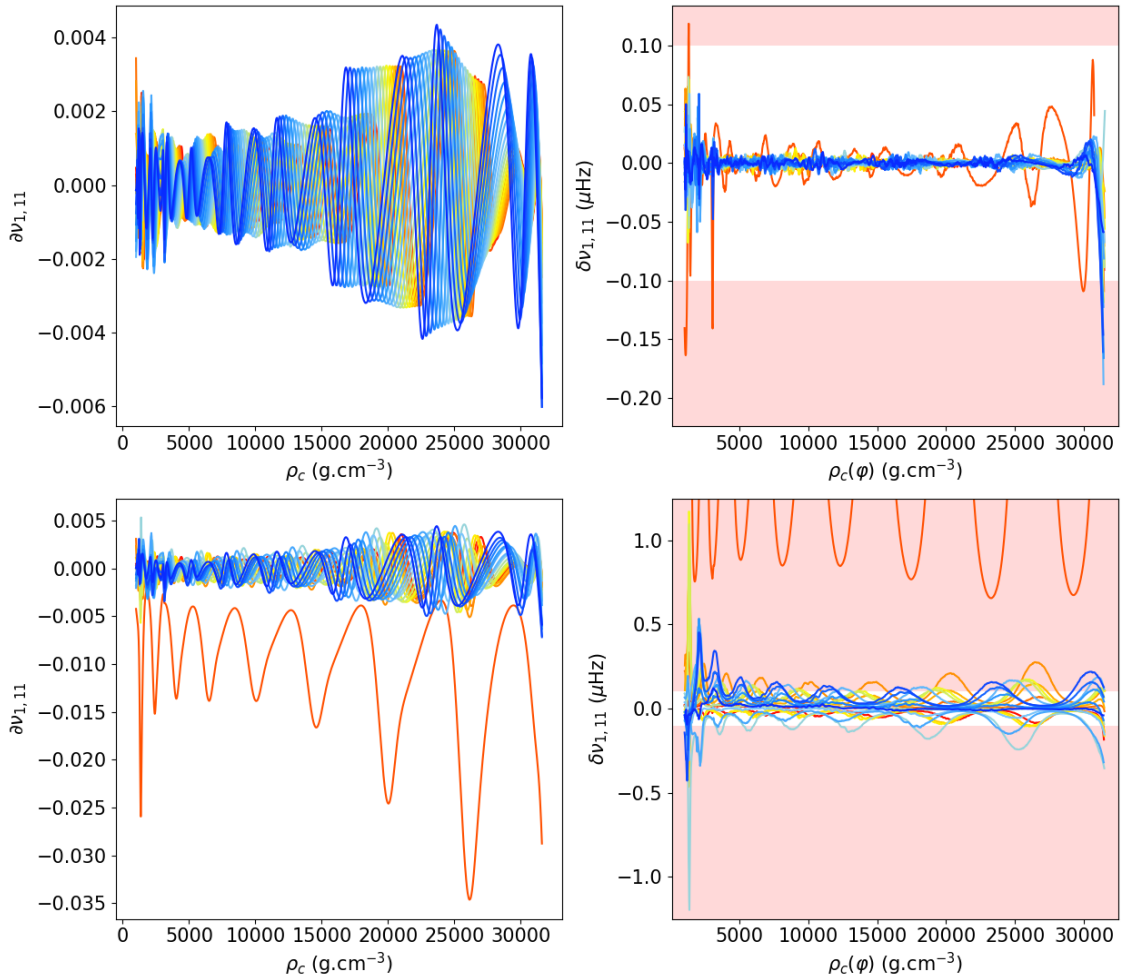


Figure 4.6: Comparison of the residuals from the fitting process (left column) and the interpolation errors (right column), resulting from the variable transformation of both known (top row) and unknown (bottom row) frequency fitting functions. These results are obtained through the application of the full interpolation algorithm (which uses cubic splines along and linear interpolation across evolutionary tracks) to all $\nu_{1,11}$ frequency modes in the stellar grid, using $\varphi(\rho_c)$ as the age proxy for interpolation. In both right-hand panels, the white area indicates the typical range of observational errors, serving as the limit for our interpolation errors. The coloured lines in each plot represent the same mass values indicated in the caption of Figure 4.4.

case (top left panel) showing a much smoother change in the residuals when adjacent masses are considered when compared to the second case (bottom left panel).

The results from the interpolation in the two cases are shown in the right panels of Figure 4.6. Clearly, the improvements observed in the top right panel of Figure 4.6 are no longer evident in the bottom right of Figure 4.6. In fact, most of the interpolation errors were reverted to values comparable to those reported in Section 2.3.4 (and shown in the right panel of Figure 4.4).

To investigate further, we repeat the same exercise for modes of different radial order.

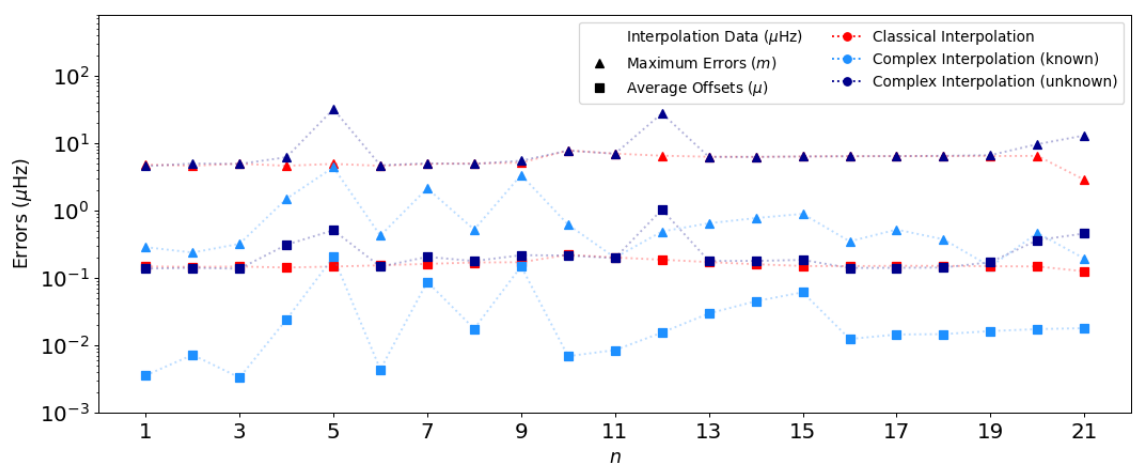


Figure 4.7: Average offsets (μ, indicated by squares; in μHz) and maximum errors (m, indicated by triangles; in μHz) obtained for all ℓ=1 modes of the initial grid. The results are presented for the three interpolation methods discussed in this section: the best classical interpolation method, defined in Chapter 2 (red), and the complex interpolation methods discussed in this chapter, both when the necessary fitting functions for the interpolated evolutionary tracks are known (cyan) and when they are unknown (blue).

Figure 4.7 illustrates the maximum errors and average offsets produced by the three interpolation methods discussed in this section for all $\ell = 1$ modes of the grid: the best classical interpolation method, which considers ρ_c as an age proxy, and the two complex interpolation methods, applied when the fitting functions for the mode frequencies of the interpolated evolutionary tracks are either known or unknown.

For most radial orders n, when the fitting functions are known, the complex interpolation methods provide improvements of roughly one order of magnitude over the classical method.* However, when the fitting functions are unknown, the final complex interpolation results revert to those obtained with the classical interpolation method - being sometimes even slightly worst.

This degradation in performance (compared to that presented at the beginning of this section) can be attributed to the fact that, although the data were nearly linearized prior to applying the interpolation algorithm, enabling an accurate interpolation, there is now a mismatch between the $\varphi(\rho_c)$ of the models used in the interpolation and that of the model for which we want to interpolate. This mismatch arises because the transformation applied on the latter model is affected by a significant error, since an additional interpolation is

*Exceptions occur for some radial orders, namely for $n = 5, 7, 9$. The large number of arctangent functions in these fitting functions requires precise initial guesses for each parameter in the `Python` code. In these cases, the deviations arise either from (a) insufficient data to fit a complete arctangent function for an incomplete avoided crossing, or (b) avoided crossings that are too smooth, making a correct fit difficult.

now performed on the parameters of the fitting functions. As a result, the benefits of the transformation procedure are not fully realized.

In conclusion, the results of this interpolation method show only marginal improvements over those presented in Section 2.3.4, which are insufficient to justify the use of a more complex interpolation algorithm - particularly when a simpler approach can render similar results.

5. Conclusions

Interpolation methods are commonly used by optimization codes (such as AIMS) to compensate for the lack of resolution in typical stellar grids, by predicting an approximate description of both the global and seismic properties of models at points in the parameter space that lie between those of the original pre-computed discrete grid. This way, these methods help mitigate the need for extreme fine grids of models, while still ensuring that the science requirements for space missions (such as PLATO) can be satisfied.

This issue becomes especially important during the subgiant phase, not only because subgiant stars evolve more rapidly across the HR diagram than they did during their main sequence, but also due to the emergence of avoided crossings. Previous studies (e.g. Deheuvels and Michel (2011)) have shown that the presence of mixed modes in subgiant stars – whose frequencies vary on a very short timescale (in evolutionary terms) – allows for the determination of stellar parameters with very high precision, provided the model grids considered have sufficient resolution. However, this is not the case for most stellar grids commonly used in this field. As shown in this work, their limited resolution often leads to errors that exceed typical observational uncertainties of 0.1 μHz, an accuracy limit we established based on previous works (e.g. Li et al. (2020)).

In this thesis, we performed a detailed study of classical interpolation algorithms applied to a grid of stellar models in the subgiant phase, characterizing the errors associated with classical interpolation schemes and discussing the associated problems with these interpolation schemes, while also exploring ways to improve them. We started by verifying whether these algorithms ensure the computation of non-radial $\ell = 1$ mode frequencies with interpolation errors within the typical observational errors ($\sim$ 0.1 μHz).

This study was applied to a grid of 41 evolutionary tracks, with stellar mass as the only grid input, varying between 1.150 and 1.350 $M_\odot$, and mass values separated in steps of 0.005 $M_\odot$. This range of mass values was chosen to cover the mass transition where their MS progenitors start to develop a sustained convective core. All other inputs were kept fixed, including the convective overshooting parameter, which was set to $f_{\rm ov} = 0.01$.

For the interpolation procedure, we tested several variations of the two-step interpolation algorithm, which considered various order methods (linear and cubic splines) and different options for age proxies (physical age, τ, scaled age, $\tau_{\rm scaled}$, and central density, $\rho_{\rm c}$) for

both interpolation along an evolutionary track and across evolutionary tracks of different masses.

We began by examining a group of interpolation methods applied both along and across evolutionary tracks, focusing on the $\ell = 1$ frequency modes of the mass track with M=1.245 $M_\odot$. For this mass track, we found that the most effective interpolation approach considers cubic splines for interpolation along tracks, linear interpolation for interpolation across tracks, and ρ_c as the preferred age proxy. However, even this approach produced an average offset of 1.5×10^{-1} μHz, about 1.5 times greater than the desired accuracy limit of 0.1 μHz, and a maximum error of 1.3×10^{0} μHz, which exceeds the accuracy limit by an order of magnitude. In conclusion, none of the considered configurations was able to satisfy the required accuracy limit.

The results of applying interpolation to the full grid (shown in Figure 2.11) reinforced the previous conclusions. The best results were obtained with the interpolation scheme that considered cubic spline interpolation along evolutionary tracks, linear interpolation across evolutionary tracks, and ρ_c as the age proxy. The latter is likely a reflection of the pronounced non-linearity of the mixed mode frequencies, which become more systematically aligned when presented as a function of ρ_c. However, the accuracy goal is not satisfied in any of the considered configurations, with the maximum interpolation error surpassing the reference accuracy limit of 0.1 μHz by at least an order of magnitude for most of the interpolated mass tracks. With the exception of the mass track with 1.175 $M_\odot$, the average offset when taking ρ_c as the age proxy is always approximately within a factor of two of the reference value. The best interpolation algorithm yielded average offsets within twice the reference limit, but maximum errors up to an order of magnitude higher. These results show that the identification of an age proxy that is fully appropriate for the interpolation of mode frequencies in the presence of avoided crossings remains an open problem.

We also examined the results of testing different resolutions of the initial grid and their implications for the interpolation results. We started with about 1500 models per evolutionary track to be used in interpolation, and decreased such number progressively to 1/6 of that value, in order to investigate how results are influenced by grid resolution. We found that reducing the number of models per evolutionary track to approximately 1/3 of the initial value (i.e., about 500 models per evolutionary track) does not affect the accuracy of the results from our grid in any significant way, as the average offset remains

only within twice the accuracy limit. This seems to establish a minimal number of models required per subgiant evolutionary track within the grid paradigm considered here. Nevertheless, we should emphasize that, for every configuration considered, the maximum errors across the grid remain significantly above the established goal, and that grid regions where the stellar structure varies abruptly are particularly prone to even larger systematic interpolation errors.

With respect to the mass track with 1.175 $M_{\odot}$, our results highlighted large, systematic interpolation errors all along the subgiant phase. This prompted an investigation of their origin and of the implications for the construction of model grids, based on how we expect interpolation to be affected by abrupt changes of the mode frequencies across the parameter space. We found that these errors likely arise from variations in core properties at specific mass transitions, particularly between stars with convective and radiative cores during their main sequence.

From the analysis of multiple grids, we found out that turning off the core convective overshoot eliminates these systematic errors, demonstrating that overshoot plays a key role in intensifying the abrupt changes in the core conditions. Given that turning off convective overshoot altogether is not physically realistic, we explored an observationally-driven alternative, which points to a smooth transition in the amount of overshoot when crossing the mass range where stars in the MS start to have a sustainable convective core. We showed that implementing a mass-dependent overshoot parameter, $f_{\mathrm{ov}}(M)$, smooths the transition between stars with radiative cores and stars with convective cores, reducing interpolation errors to values comparable with those observed in other mass tracks of the same stellar grid.

As convective overshoot is not the only factor that can lead to potential abrupt physical transitions in stellar grids (e.g. the options made regarding the treatment of diffusion of chemical elements can also impact such models), special attention should be given to these transitions when building any grid of models, and the interpolation of the grid should be carefully tested before applying the grid to the modelling of stars.

Given that the relatively large errors in the interpolated frequencies occur for modes near the avoided crossings, where the evolution of the mode frequency with any of the studied age proxies is highly non-linear, we also attempted to define a new age proxy, $\varphi(\rho_{\mathrm{c}})$, such that the mode frequencies' dependence on this new age proxy would remain approximately linear throughout the subgiant phase. For that, we employed an asymptotic

analysis to the mixed modes to build a function capable of accurately describing the evolution of a mode frequency both around and away from the avoided crossings.

Using the asymptotic representation of the modes, we have defined a new age proxy and showed that the interpolation across evolutionary tracks performed at a fixed value of this new age proxy is one order of magnitude better than when performed at fixed ρ_c. Moreover, we found that using the new age proxy dissipates the problem previously found when interpolating across the evolutionary tracks where convective cores start to develop. However, exploring the model parameter space in terms of the new variable is challenging because the asymptotic representation used to convert between ρ_c and the new variable is specific for each mass and mode radial order. To avoid that complexity, we attempted to develop a method that would enable exploring the original parameter space directly, but still interpolating across tracks at a fixed value of the new age proxy. This implied estimating the asymptotic representation of evolutionary tracks that are not part of the grid.

The results of this new procedure showed that the improvements observed before were no longer evident, with most of the interpolation errors reverting to values comparable to those reported when ρ_c was considered as the age proxy. This degradation in performance can be attributed to a mismatch between the $\varphi(\rho_c)$ of the models used in the interpolation and that of the target model (the frequencies of which we want to know through interpolation). This mismatch arises because the transformation applied on the latter model is affected by a significant error. As a result, the benefits of the transformation procedure previously observed could not be fully realized. Improvements to this method may still be possible in the future, either by modifying the function used to perform the fits to the evolution of the mode frequencies - which so far relied on approximations introduced when deriving Equation 4.9 - or by developing a method aimed at exploring directly the parameter space that results from the transformation from ρ_c to $\varphi(\rho_c)$.

Overall, this thesis has revealed persistent challenges that limit the accuracy of the interpolated mode frequencies when mixed modes are concerned. Considering that mixed modes in subgiant stars are thought to be of particular interest for the potential they offer to constrain stellar physics, our findings should be seen as a warning sign and provide motivation to invest in the development of alternative interpolation procedures. This is particularly so in the context of space missions collecting asteroseismic data to characterize stars, such as PLATO, whose pipelines may rely on the use of stellar grids of models.

References

Aerts, C., Christensen-Dalsgaard, J., and Kurtz, D. W. (2010). *Asteroseismology*. [Cited on page 21.]

Aguirre Børsen-Koch, V., Rørsted, J. L., Justesen, A. B., Stokholm, A., Verma, K., Winther, M. L., Knudstrup, E., Nielsen, K. B., Sahlholdt, C., Larsen, J. R., Cassisi, S., Serenelli, A. M., Casagrande, L., Christensen-Dalsgaard, J., Davies, G. R., Ferguson, J. W., Lund, M. N., Weiss, A., and White, T. R. (2022). The BAyesian STellar algorithm (BASTA): a fitting tool for stellar studies, asteroseismology, exoplanets, and Galactic archaeology. , 509(3):4344–4364. [Cited on pages 33 and 38.]

Anders, E. H. and Pedersen, M. G. (2023). Convective Boundary Mixing in Main-Sequence Stars: Theory and Empirical Constraints. *Galaxies*, 11(2):56. [Cited on pages 10, 12, 13, 15, 63, and 66.]

Asplund, M., Grevesse, N., Sauval, A. J., and Scott, P. (2009). The Chemical Composition of the Sun. , 47(1):481–522. [Cited on page 40.]

Baglin, A., Auvergne, M., Boisnard, L., Lam-Trong, T., Barge, P., Catala, C., Deleuil, M., Michel, E., and Weiss, W. (2006). CoRoT: a high precision photometer for stellar ecolution and exoplanet finding. 36:3749. [Cited on pages 1 and 32.]

Balser, D. S. (2006). The Chemical Evolution of Helium. , 132(6):2326–2332. [Cited on page 40.]

Bellinger, E. P., Basu, S., Hekker, S., Christensen-Dalsgaard, J., and Ball, W. H. (2021). Asteroseismic Inference of the Central Structure in a Subgiant Star. , 915(2):100. [Cited on page 3.]

Böhm-Vitense, E. (1958). Über die Wasserstoffkonvektionszone in Sternen verschiedener Effektivtemperaturen und Leuchtkräfte. Mit 5 Textabbildungen. , 46:108. [Cited on pages 9, 11, and 40.]

Campante, T. L., Schofield, M., Kuszlewicz, J. S., Bouma, L., Chaplin, W. J., Huber, D., Christensen-Dalsgaard, J., Kjeldsen, H., Bossini, D., North, T. S. H., Appourchaux, T., Latham, D. W., Pepper, J., Ricker, G. R., Stassun, K. G., Vanderspek, R., and Winn, J. N. (2016). The Asteroseismic Potential of TESS: Exoplanet-host Stars. , 830(2):138. [Cited on pages 1 and 32.]

Carroll, B. W. and Ostlie, D. A. (2017). *An introduction to modern astrophysics, Second Edition*. Pearson. [Cited on page 17.]

Clara, M. (2019). Asteroseismology with the Space Mission PLATO: Testing Modelling Requirements for Subgiant Stars. Master's thesis, FCUP. [Cited on page 3.]

Clara, M., Cunha, M. S., Avelino, P. P., Campante, T. L., Deheuvels, S., and Reese, D. R. (2025). On the seismic modelling of subgiant stars: testing different grid interpolation methods. *arXiv e-prints*, page arXiv:2501.09809. [Cited on pages 38 and 63.]

Claret, A. and Torres, G. (2017). The Dependence of Convective Core Overshooting on Stellar Mass: A Semi-empirical Determination Using the Diffusive Approach with Two Different Element Mixtures. , 849(1):18. [Cited on page 63.]

Claret, A. and Torres, G. (2018). The Dependence of Convective Core Overshooting on Stellar Mass: Additional Binary Systems and Improved Calibration. , 859(2):100. [Cited on pages x, 63, 65, 66, and 67.]

Claret, A. and Torres, G. (2019). The Dependence of Convective Core Overshooting on Stellar Mass: Reality Check and Additional Evidence. , 876(2):134. [Cited on page 65.]

Cox, J. P. and Giuli, R. T. (1968). *Principles of stellar structure*. [Cited on page 40.]

Cunha, M. S. (2018). Theory of Stellar Oscillations. 49:27. [Cited on pages 21 and 24.]

Cunha, M. S., Antoci, V., Holdsworth, D. L., Kurtz, D. W., Balona, L. A., Bognár, Z., Bowman, D. M., Guo, Z., Kołaczek-Szymański, P. A., Lares-Martiz, M., Paunzen, E., Skarka, M., Smalley, B., Sódor, Á., Kochukhov, O., Pepper, J., Richey-Yowell, T., Ricker, G. R., Seager, S., Buzasi, D. L., Fox-Machado, L., Hasanzadeh, A., Niemczura, E., Quitral-Manosalva, P., Monteiro, M. J. P. F. G., Stateva, I., De Cat, P., García Hernández, A., Ghasemi, H., Handler, G., Hey, D., Matthews, J. M., Nemec, J. M., Pascual-Granado, J., Safari, H., Suárez, J. C., Szabó, R., Tkachenko, A., and Weiss, W. W. (2019). Rotation and pulsation in Ap stars: first light results from TESS sectors 1 and 2. , 487(3):3523–3549. [Cited on pages 1 and 32.]

Cunha, M. S., Roxburgh, I. W., Aguirre Børsen-Koch, V., Ball, W. H., Basu, S., Chaplin, W. J., Goupil, M. J., Nsamba, B., Ong, J., Reese, D. R., Verma, K., Belkacem, K., Campante, T., Christensen-Dalsgaard, J., Clara, M. T., Deheuvels, S., Monteiro, M. J. P. F. G., Noll, A., Ouazzani, R. M., Rørsted, J. L., Stokholm, A., and Winther,

M. L. (2021a). PLATO hare-and-hounds exercise: asteroseismic model fitting of main-sequence solar-like pulsators. , 508(4):5864–5885. [Cited on pages 1 and 32.]

Cunha, M. S., Roxburgh, I. W., Aguirre Børsen-Koch, V., Ball, W. H., Basu, S., Chaplin, W. J., Goupil, M. J., Nsamba, B., Ong, J., Reese, D. R., Verma, K., Belkacem, K., Campante, T., Christensen-Dalsgaard, J., Clara, M. T., Deheuvels, S., Monteiro, M. J. P. F. G., Noll, A., Ouazzani, R. M., Rørsted, J. L., Stokholm, A., and Winther, M. L. (2021b). PLATO hare-and-hounds exercise: asteroseismic model fitting of main-sequence solar-like pulsators. , 508(4):5864–5885. [Cited on page 3.]

Cyburt, R. H., Fields, B. D., and Olive, K. A. (2003). Primordial nucleosynthesis in light of WMAP. *Physics Letters B*, 567(3-4):227–234. [Cited on page 40.]

Deheuvels, S., Brandão, I., Silva Aguirre, V., Ballot, J., Michel, E., Cunha, M. S., Lebreton, Y., and Appourchaux, T. (2016). Measuring the extent of convective cores in low-mass stars using Kepler data: toward a calibration of core overshooting. , 589:A93. [Cited on pages 63 and 65.]

Deheuvels, S. and Michel, E. (2011). Constraints on the structure of the core of subgiants via mixed modes: the case of HD 49385. , 535:A91. [Cited on pages 31, 32, and 90.]

Ferguson, J. W., Alexander, D. R., Allard, F., Barman, T., Bodnarik, J. G., Hauschildt, P. H., Heffner-Wong, A., and Tamanai, A. (2005). Low-Temperature Opacities. , 623(1):585–596. [Cited on page 40.]

Fossat, E., Boumier, P., Corbard, T., Provost, J., Salabert, D., Schmider, F. X., Gabriel, A. H., Grec, G., Renaud, C., Robillot, J. M., Roca-Cortés, T., Turck-Chièze, S., Ulrich, R. K., and Lazrek, M. (2017). Asymptotic g modes: Evidence for a rapid rotation of the solar core. , 604:A40. [Cited on page 28.]

Freytag, B., Ludwig, H. G., and Steffen, M. (1996). Hydrodynamical models of stellar convection. The role of overshoot in DA white dwarfs, A-type stars, and the Sun. , 313:497–516. [Cited on page 12.]

García, R. A. and Ballot, J. (2019). Asteroseismology of solar-type stars. *Living Reviews in Solar Physics*, 16(1):4. [Cited on page 28.]

García, R. A., Ballot, J., Eff-Darwich, A., Garrido, R., Jimenez, A., Mathis, S., Mathur, S., Moya, A., Palle, P. L., Regulo, C., Salabert, D., Suarez, J. C., and Turck-Chieze,

S. (2010). Towards a detection of individual g modes in the Sun. *arXiv e-prints*, page arXiv:1007.4445. [Cited on page 28.]

Gilliland, R. L., Brown, T. M., Christensen-Dalsgaard, J., Kjeldsen, H., Aerts, C., Appourchaux, T., Basu, S., Bedding, T. R., Chaplin, W. J., Cunha, M. S., De Cat, P., De Ridder, J., Guzik, J. A., Handler, G., Kawaler, S., Kiss, L., Kolenberg, K., Kurtz, D. W., Metcalfe, T. S., Monteiro, M. J. P. F. G., Szabó, R., Arentoft, T., Balona, L., Debosscher, J., Elsworth, Y. P., Quirion, P.-O., Stello, D., Suárez, J. C., Borucki, W. J., Jenkins, J. M., Koch, D., Kondo, Y., Latham, D. W., Rowe, J. F., and Steffen, J. H. (2010). Kepler Asteroseismology Program: Introduction and First Results. , 122(888):131. [Cited on pages 1 and 32.]

Gough, D. O. (1993). Linear adiabatic stellar pulsation. In Zahn, J. P. and Zinn-Justin, J., editors, *Astrophysical Fluid Dynamics - Les Houches 1987*, pages 399–560. [Cited on page 25.]

Goupil, M. J., Catala, C., Samadi, R., Belkacem, K., Ouazzani, R. M., Reese, D. R., Appourchaux, T., Mathur, S., Cabrera, J., Börner, A., Paproth, C., Moedas, N., Verma, K., Lebreton, Y., Deal, M., Ballot, J., Chaplin, W. J., Christensen-Dalsgaard, J., Cunha, M., Lanza, A. F., Miglio, A., Morel, T., Serenelli, A., Mosser, B., Creevey, O., Moya, A., Garcia, R. A., Nielsen, M. B., and Hatt, E. (2024). Predicted asteroseismic detection yield for solar-like oscillating stars with PLATO. , 683:A78. [Cited on pages 1 and 32.]

Grevesse, N. and Sauval, A. J. (1998). Standard Solar Composition. , 85:161–174. [Cited on page 40.]

Hekker, S. and Mazumdar, A. (2014). Solar-like oscillations in subgiant and red-giant stars: mixed modes. In Guzik, J. A., Chaplin, W. J., Handler, G., and Pigulski, A., editors, *Precision Asteroseismology*, volume 301 of *IAU Symposium*, pages 325–331. [Cited on page 26.]

Herwig, F. (2000). The evolution of AGB stars with convective overshoot. , 360:952–968. [Cited on pages 11 and 41.]

Huber, D., Chaplin, W. J., Chontos, A., Kjeldsen, H., Christensen-Dalsgaard, J., Bedding, T. R., Ball, W., Brahm, R., Espinoza, N., Henning, T., Jordán, A., Sarkis, P., Knudstrup, E., Albrecht, S., Grundahl, F., Fredslund Andersen, M., Pallé, P. L., Crossfield, I., Fulton, B., Howard, A. W., Isaacson, H. T., Weiss, L. M., Handberg, R., Lund, M. N., Serenelli, A. M., Rørsted Mosumgaard, J., Stokholm, A., Bieryla, A., Buchhave, L. A.,

Latham, D. W., Quinn, S. N., Gaidos, E., Hirano, T., Ricker, G. R., Vanderspek, R. K., Seager, S., Jenkins, J. M., Winn, J. N., Antia, H. M., Appourchaux, T., Basu, S., Bell, K. J., Benomar, O., Bonanno, A., Buzasi, D. L., Campante, T. L., Çelik Orhan, Z., Corsaro, E., Cunha, M. S., Davies, G. R., Deheuvels, S., Grunblatt, S. K., Hasanzadeh, A., Di Mauro, M. P., García, R. A., Gaulme, P., Girardi, L., Guzik, J. A., Hon, M., Jiang, C., Kallinger, T., Kawaler, S. D., Kuszlewicz, J. S., Lebreton, Y., Li, T., Lucas, M., Lundkvist, M. S., Mann, A. W., Mathis, S., Mathur, S., Mazumdar, A., Metcalfe, T. S., Miglio, A., Monteiro, M. J. P. F. G., Mosser, B., Noll, A., Nsamba, B., Ong, J. M. J., Örtel, S., Pereira, F., Ranadive, P., Régulo, C., Rodrigues, T. S., Roxburgh, I. W., Silva Aguirre, V., Smalley, B., Schofield, M., Sousa, S. G., Stassun, K. G., Stello, D., Tayar, J., White, T. R., Verma, K., Vrard, M., Yıldız, M., Baker, D., Bazot, M., Beichmann, C., Bergmann, C., Bugnet, L., Cale, B., Carlino, R., Cartwright, S. M., Christiansen, J. L., Ciardi, D. R., Creevey, O., Dittmann, J. A., Do Nascimento, Jr., J.-D., Van Eylen, V., Fürész, G., Gagné, J., Gao, P., Gazeas, K., Giddens, F., Hall, O. J., Hekker, S., Ireland, M. J., Latouf, N., LeBrun, D., Levine, A. M., Matzko, W., Natinsky, E., Page, E., Plavchan, P., Mansouri-Samani, M., McCauliff, S., Mullally, S. E., Orenstein, B., Garcia Soto, A., Paegert, M., van Saders, J. L., Schnaible, C., Soderblom, D. R., Szabó, R., Tanner, A., Tinney, C. G., Teske, J., Thomas, A., Trampedach, R., Wright, D., Yuan, T. T., and Zohrabi, F. (2019). A Hot Saturn Orbiting an Oscillating Late Subgiant Discovered by TESS. , 157(6):245. [Cited on page 3.]

Imbriani, G., Costantini, H., Formicola, A., Vomiero, A., Angulo, C., Bemmerer, D., Bonetti, R., Broggini, C., Confortola, F., Corvisiero, P., Cruz, J., Descouvemont, P., Fülöp, Z., Gervino, G., Guglielmetti, A., Gustavino, C., Gyürky, G., Jesus, A. P., Junker, M., Klug, J. N., Lemut, A., Menegazzo, R., Prati, P., Roca, V., Rolfs, C., Romano, M., Rossi-Alvarez, C., Schümann, F., Schürmann, D., Somorjai, E., Straniero, O., Strieder, F., Terrasi, F., and Trautvetter, H. P. (2005). S-factor of ^{14}N(p,γ)^{15}O at astrophysical energies*. *European Physical Journal A*, 25(3):455–466. [Cited on page 40.]

Kippenhahn, R., Weigert, A., and Weiss, A. (2013). *Stellar Structure and Evolution*. Springer-Verlag. [Cited on pages 9, 14, and 21.]

Koch, D. G., Borucki, W. J., Basri, G., Batalha, N. M., Brown, T. M., Caldwell, D., Christensen-Dalsgaard, J., Cochran, W. D., DeVore, E., Dunham, E. W., Gautier, Thomas N., I., Geary, J. C., Gilliland, R. L., Gould, A., Jenkins, J., Kondo, Y., Latham, D. W., Lissauer, J. J., Marcy, G., Monet, D., Sasselov, D., Boss, A., Brownlee, D.,

Caldwell, J., Dupree, A. K., Howell, S. B., Kjeldsen, H., Meibom, S., Morrison, D., Owen, T., Reitsema, H., Tarter, J., Bryson, S. T., Dotson, J. L., Gazis, P., Haas, M. R., Kolodziejczak, J., Rowe, J. F., Van Cleve, J. E., Allen, C., Chandrasekaran, H., Clarke, B. D., Li, J., Quintana, E. V., Tenenbaum, P., Twicken, J. D., and Wu, H. (2010). Kepler Mission Design, Realized Photometric Performance, and Early Science. , 713(2):L79–L86. [Cited on pages 1 and 32.]

Krishna Swamy, K. S. (1966). Profiles of Strong Lines in K-Dwarfs. [Cited on page 40.]

Kunz, R., Fey, M., Jaeger, M., Mayer, A., Hammer, J. W., Staudt, G., Harissopulos, S., and Paradellis, T. (2002). Astrophysical Reaction Rate of ^{12}C(α, γ)^{16}O. , 567(1):643–650. [Cited on page 40.]

Lebreton, Y. and Reese, D. R. (2020). SPInS, a pipeline for massive stellar parameter inference. A public Python tool to age-date, weigh, size up stars, and more. , 642:A88. [Cited on page 33.]

Ledoux, P. (1947). On stellar models with convection and discontinuity of the mean molecular weight. , 52:155. [Cited on page 13.]

Li, T., Bedding, T. R., Christensen-Dalsgaard, J., Stello, D., Li, Y., and Keen, M. A. (2020). Asteroseismology of 36 Kepler subgiants - II. Determining ages from detailed modelling. , 495(3):3431–3462. [Cited on pages 3, 4, 38, 39, and 90.]

Li, T., Bedding, T. R., Kjeldsen, H., Stello, D., Christensen-Dalsgaard, J., and Deng, L. (2019). Asteroseismic modelling of the subgiant μ Herculis using SONG data: lifting the degeneracy between age and model input parameters. , 483(1):780–789. [Cited on page 32.]

Lindsay, C. J., Ong, J. M. J., and Basu, S. (2024). Fossil Signatures of Main-sequence Convective Core Overshoot Estimated through Asteroseismic Analyses. , 965(2):171. [Cited on pages x, 63, 64, 65, and 66.]

Mombarg, J. S. G., Van Reeth, T., and Aerts, C. (2021). Constraining stellar evolution theory with asteroseismology of γ Doradus stars using deep learning. Stellar masses, ages, and core-boundary mixing. , 650:A58. [Cited on pages 63, 65, and 66.]

Mosser, B., Elsworth, Y., Hekker, S., Huber, D., Kallinger, T., Mathur, S., Belkacem, K., Goupil, M. J., Samadi, R., Barban, C., Bedding, T. R., Chaplin, W. J., García, R. A., Stello, D., De Ridder, J., Middour, C. K., Morris, R. L., and Quintana, E. V. (2012).

Characterization of the power excess of solar-like oscillations in red giants with Kepler. , 537:A30. [Cited on page 42.]

Noll, A. and Deheuvels, S. (2023). Impact of central mixing scheme and nuclear reaction network on the extent of convective cores. , 676:A70. [Cited on page 65.]

Noll, A., Deheuvels, S., and Ballot, J. (2021). Probing core overshooting using subgiant asteroseismology: The case of KIC10273246. , 647:A187. [Cited on pages 3 and 65.]

Nsamba, B., Campante, T. L., Monteiro, M. J. P. F. G., Cunha, M. S., Rendle, B. M., Reese, D. R., and Verma, K. (2018). Asteroseismic modelling of solar-type stars: internal systematics from input physics and surface correction methods. , 477(4):5052–5063. [Cited on page 42.]

Nsamba, B., Moedas, N., Campante, T. L., Cunha, M. S., Hernández, A. G., Suárez, J. C., Monteiro, M. J. P. F. G., Fernandes, J., Jiang, C., and Akinsanmi, B. (2021). Asteroseismic modelling of solar-type stars: a deeper look at the treatment of initial helium abundance. , 500(1):54–65. [Cited on page 40.]

Nsamba, B., Weiss, A., and Kamulali, J. (2025). Uniform characterization of an ensemble of main-sequence benchmark stars: effect of Gaia-based data on grid search models. , 536(3):2558–2571. [Cited on page 76.]

Ong, J. M. J. and Gehan, C. (2023). Mode Mixing and Rotational Splittings. II. Reconciling Different Approaches to Mode Coupling. , 946(2):92. [Cited on page 77.]

Paxton, B., Bildsten, L., Dotter, A., Herwig, F., Lesaffre, P., and Timmes, F. (2011). Modules for Experiments in Stellar Astrophysics (MESA). , 192(1):3. [Cited on pages 40 and 41.]

Paxton, B., Cantiello, M., Arras, P., Bildsten, L., Brown, E. F., Dotter, A., Mankovich, C., Montgomery, M. H., Stello, D., Timmes, F. X., and Townsend, R. (2013). Modules for Experiments in Stellar Astrophysics (MESA): Planets, Oscillations, Rotation, and Massive Stars. , 208(1):4. [Cited on page 40.]

Paxton, B., Marchant, P., Schwab, J., Bauer, E. B., Bildsten, L., Cantiello, M., Dessart, L., Farmer, R., Hu, H., Langer, N., Townsend, R. H. D., Townsley, D. M., and Timmes, F. X. (2015). Modules for Experiments in Stellar Astrophysics (MESA): Binaries, Pulsations, and Explosions. , 220(1):15. [Cited on page 40.]

Paxton, B., Schwab, J., Bauer, E. B., Bildsten, L., Blinnikov, S., Duffell, P., Farmer, R., Goldberg, J. A., Marchant, P., Sorokina, E., Thoul, A., Townsend, R. H. D., and Timmes, F. X. (2018). Modules for Experiments in Stellar Astrophysics (MESA): Convective Boundaries, Element Diffusion, and Massive Star Explosions. , 234(2):34. [Cited on page 40.]

Paxton, B., Smolec, R., Schwab, J., Gautschy, A., Bildsten, L., Cantiello, M., Dotter, A., Farmer, R., Goldberg, J. A., Jermyn, A. S., Kanbur, S. M., Marchant, P., Thoul, A., Townsend, R. H. D., Wolf, W. M., Zhang, M., and Timmes, F. X. (2019). Modules for Experiments in Stellar Astrophysics (MESA): Pulsating Variable Stars, Rotation, Convective Boundaries, and Energy Conservation. , 243(1):10. [Cited on page 40.]

Pedersen, M. G., Aerts, C., Pápics, P. I., and Rogers, T. M. (2018). The shape of convective core overshooting from gravity-mode period spacings. , 614:A128. [Cited on pages 10, 11, 13, and 63.]

Planck Collaboration, Ade, P. A. R., Aghanim, N., Arnaud, M., Ashdown, M., Aumont, J., Baccigalupi, C., Banday, A. J., Barreiro, R. B., Bartlett, J. G., Bartolo, N., Battaner, E., Battye, R., Benabed, K., Benoît, A., Benoit-Lévy, A., Bernard, J. P., Bersanelli, M., Bielewicz, P., Bock, J. J., Bonaldi, A., Bonavera, L., Bond, J. R., Borrill, J., Bouchet, F. R., Boulanger, F., Bucher, M., Burigana, C., Butler, R. C., Calabrese, E., Cardoso, J. F., Catalano, A., Challinor, A., Chamballu, A., Chary, R. R., Chiang, H. C., Chluba, J., Christensen, P. R., Church, S., Clements, D. L., Colombi, S., Colombo, L. P. L., Combet, C., Coulais, A., Crill, B. P., Curto, A., Cuttaia, F., Danese, L., Davies, R. D., Davis, R. J., de Bernardis, P., de Rosa, A., de Zotti, G., Delabrouille, J., Désert, F. X., Di Valentino, E., Dickinson, C., Diego, J. M., Dolag, K., Dole, H., Donzelli, S., Doré, O., Douspis, M., Ducout, A., Dunkley, J., Dupac, X., Efstathiou, G., Elsner, F., Enßlin, T. A., Eriksen, H. K., Farhang, M., Fergusson, J., Finelli, F., Forni, O., Frailis, M., Fraisse, A. A., Franceschi, E., Frejsel, A., Galeotta, S., Galli, S., Ganga, K., Gauthier, C., Gerbino, M., Ghosh, T., Giard, M., Giraud-Héraud, Y., Giusarma, E., Gjerløw, E., González-Nuevo, J., Górski, K. M., Gratton, S., Gregorio, A., Gruppuso, A., Gudmundsson, J. E., Hamann, J., Hansen, F. K., Hanson, D., Harrison, D. L., Helou, G., Henrot-Versillé, S., Hernández-Monteagudo, C., Herranz, D., Hildebrandt, S. R., Hivon, E., Hobson, M., Holmes, W. A., Hornstrup, A., Hovest, W., Huang, Z., Huffenberger, K. M., Hurier, G., Jaffe, A. H., Jaffe, T. R., Jones, W. C., Juvela, M., Keihänen, E., Keskitalo, R., Kisner, T. S., Kneissl, R., Knoche, J., Knox, L., Kunz, M., Kurki-Suonio,

H., Lagache, G., Lähteenmäki, A., Lamarre, J. M., Lasenby, A., Lattanzi, M., Lawrence, C. R., Leahy, J. P., Leonardi, R., Lesgourgues, J., Levrier, F., Lewis, A., Liguori, M., Lilje, P. B., Linden-Vørnle, M., López-Caniego, M., Lubin, P. M., Macías-Pérez, J. F., Maggio, G., Maino, D., Mandolesi, N., Mangilli, A., Marchini, A., Maris, M., Martin, P. G., Martinelli, M., Martínez-González, E., Masi, S., Matarrese, S., McGehee, P., Meinhold, P. R., Melchiorri, A., Melin, J. B., Mendes, L., Mennella, A., Migliaccio, M., Millea, M., Mitra, S., Miville-Deschênes, M. A., Moneti, A., Montier, L., Morgante, G., Mortlock, D., Moss, A., Munshi, D., Murphy, J. A., Naselsky, P., Nati, F., Natoli, P., Netterfield, C. B., Nørgaard-Nielsen, H. U., Noviello, F., Novikov, D., Novikov, I., Oxborrow, C. A., Paci, F., Pagano, L., Pajot, F., Paladini, R., Paoletti, D., Partridge, B., Pasian, F., Patanchon, G., Pearson, T. J., Perdereau, O., Perotto, L., Perrotta, F., Pettorino, V., Piacentini, F., Piat, M., Pierpaoli, E., Pietrobon, D., Plaszczynski, S., Pointecouteau, E., Polenta, G., Popa, L., Pratt, G. W., Prézeau, G., Prunet, S., Puget, J. L., Rachen, J. P., Reach, W. T., Rebolo, R., Reinecke, M., Remazeilles, M., Renault, C., Renzi, A., Ristorcelli, I., Rocha, G., Rosset, C., Rossetti, M., Roudier, G., Rouillé d'Orfeuil, B., Rowan-Robinson, M., Rubiño-Martín, J. A., Rusholme, B., Said, N., Salvatelli, V., Salvati, L., Sandri, M., Santos, D., Savelainen, M., Savini, G., Scott, D., Seiffert, M. D., Serra, P., Shellard, E. P. S., Spencer, L. D., Spinelli, M., Stolyarov, V., Stompor, R., Sudiwala, R., Sunyaev, R., Sutton, D., Suur-Uski, A. S., Sygnet, J. F., Tauber, J. A., Terenzi, L., Toffolatti, L., Tomasi, M., Tristram, M., Trombetti, T., Tucci, M., Tuovinen, J., Türler, M., Umana, G., Valenziano, L., Valiviita, J., Van Tent, F., Vielva, P., Villa, F., Wade, L. A., Wandelt, B. D., Wehus, I. K., White, M., White, S. D. M., Wilkinson, A., Yvon, D., Zacchei, A., and Zonca, A. (2016). Planck 2015 results. XIII. Cosmological parameters. , 594:A13. [Cited on page 40.]

Rauer, H., Catala, C., Aerts, C., Appourchaux, T., Benz, W., Brandeker, A., Christensen-Dalsgaard, J., Deleuil, M., Gizon, L., Goupil, M. J., Güdel, M., Janot-Pacheco, E., Mas-Hesse, M., Pagano, I., Piotto, G., Pollacco, D., Santos, Ċ., Smith, A., Suárez, J. C., Szabó, R., Udry, S., Adibekyan, V., Alibert, Y., Almenara, J. M., Amaro-Seoane, P., Eiff, M. A.-v., Asplund, M., Antonello, E., Barnes, S., Baudin, F., Belkacem, K., Bergemann, M., Bihain, G., Birch, A. C., Bonfils, X., Boisse, I., Bonomo, A. S., Borsa, F., Brandão, I. M., Brocato, E., Brun, S., Burleigh, M., Burston, R., Cabrera, J., Cassisi, S., Chaplin, W., Charpinet, S., Chiappini, C., Church, R. P., Csizmadia, S., Cunha, M., Damasso, M., Davies, M. B., Deeg, H. J., Díaz, R. F., Dreizler, S., Dreyer, C., Eggenberger, P., Ehrenreich, D., Eigmüller, P., Erikson, A., Farmer, R., Feltzing, S., de Oliveira Fialho, F.,

Figueira, P., Forveille, T., Fridlund, M., García, R. A., Giommi, P., Giuffrida, G., Godolt, M., Gomes da Silva, J., Granzer, T., Grenfell, J. L., Grotsch-Noels, A., Günther, E., Haswell, C. A., Hatzes, A. P., Hébrard, G., Hekker, S., Helled, R., Heng, K., Jenkins, J. M., Johansen, A., Khodachenko, M. L., Kislyakova, K. G., Kley, W., Kolb, U., Krivova, N., Kupka, F., Lammer, H., Lanza, A. F., Lebreton, Y., Magrin, D., Marcos-Arenal, P., Marrese, P. M., Marques, J. P., Martins, J., Mathis, S., Mathur, S., Messina, S., Miglio, A., Montalban, J., Montalto, M., Monteiro, M. J. P. F. G., Moradi, H., Moravveji, E., Mordasini, C., Morel, T., Mortier, A., Nascimbeni, V., Nelson, R. P., Nielsen, M. B., Noack, L., Norton, A. J., Ofir, A., Oshagh, M., Ouazzani, R. M., Pápics, P., Parro, V. C., Petit, P., Plez, B., Poretti, E., Quirrenbach, A., Ragazzoni, R., Raimondo, G., Rainer, M., Reese, D. R., Redmer, R., Reffert, S., Rojas-Ayala, B., Roxburgh, I. W., Salmon, S., Santerne, A., Schneider, J., Schou, J., Schuh, S., Schunker, H., Silva-Valio, A., Silvotti, R., Skillen, I., Snellen, I., Sohl, F., Sousa, S. G., Sozzetti, A., Stello, D., Strassmeier, K. G., Švanda, M., Szabó, G. M., Tkachenko, A., Valencia, D., Van Grootel, V., Vauclair, S. D., Ventura, P., Wagner, F. W., Walton, N. A., Weingrill, J., Werner, S. C., Wheatley, P. J., and Zwintz, K. (2014). The PLATO 2.0 mission. *Experimental Astronomy*, 38(1-2):249–330. [Cited on pages 1 and 32.]

Rauer, H., Heras, A., Mas-Hesse, M., and Pagano, I. (2023). The PLATO Mission – An Overview. In *AAS/Division for Planetary Sciences Meeting Abstracts*, volume 55 of *AAS/Division for Planetary Sciences Meeting Abstracts*, page 319.01. [Cited on pages 1 and 32.]

Rendle, B. M., Buldgen, G., Miglio, A., Reese, D., Noels, A., Davies, G. R., Campante, T. L., Chaplin, W. J., Lund, M. N., Kuszlewicz, J. S., Scott, L. J. A., Scuflaire, R., Ball, W. H., Smetana, J., and Nsamba, B. (2019). AIMS - a new tool for stellar parameter determinations using asteroseismic constraints. , 484(1):771–786. [Cited on pages 3, 33, and 38.]

Ricker, G. R., Winn, J. N., Vanderspek, R., Latham, D. W., Bakos, G. Á., Bean, J. L., Berta-Thompson, Z. K., Brown, T. M., Buchhave, L., Butler, N. R., Butler, R. P., Chaplin, W. J., Charbonneau, D., Christensen-Dalsgaard, J., Clampin, M., Deming, D., Doty, J., De Lee, N., Dressing, C., Dunham, E. W., Endl, M., Fressin, F., Ge, J., Henning, T., Holman, M. J., Howard, A. W., Ida, S., Jenkins, J. M., Jernigan, G., Johnson, J. A., Kaltenegger, L., Kawai, N., Kjeldsen, H., Laughlin, G., Levine, A. M., Lin, D., Lissauer, J. J., MacQueen, P., Marcy, G., McCullough, P. R., Morton, T. D., Narita, N., Paegert,

M., Palle, E., Pepe, F., Pepper, J., Quirrenbach, A., Rinehart, S. A., Sasselov, D., Sato, B., Seager, S., Sozzetti, A., Stassun, K. G., Sullivan, P., Szentgyorgyi, A., Torres, G., Udry, S., and Villasenor, J. (2015). Transiting Exoplanet Survey Satellite (TESS). *Journal of Astronomical Telescopes, Instruments, and Systems*, 1:014003. [Cited on pages 1 and 32.]

Rodrigues, T. S., Bossini, D., Miglio, A., Girardi, L., Montalbán, J., Noels, A., Trabucchi, M., Coelho, H. R., and Marigo, P. (2017). Determining stellar parameters of asteroseismic targets: going beyond the use of scaling relations. , 467(2):1433–1448. [Cited on page 33.]

Schwarzschild, M. (1958). *Structure and evolution of the stars.* [Cited on pages 8, 9, and 13.]

Silva Aguirre, V., Ballot, J., Serenelli, A. M., and Weiss, A. (2011). Constraining mixing processes in stellar cores using asteroseismology. Impact of semiconvection in low-mass stars. , 529:A63. [Cited on pages 13, 14, and 15.]

Sonneveld, P. (1969). Errors in cubic spline interpolation. *Journal of Engineering Mathematics*, 3(2):107–117. [Cited on page 117.]

Stokholm, A., Nissen, P. E., Silva Aguirre, V., White, T. R., Lund, M. N., Mosumgaard, J. R., Huber, D., and Jessen-Hansen, J. (2019). The subgiant HR 7322 as an asteroseismic benchmark star. , 489(1):928–940. [Cited on page 3.]

Townsend, R. H. D. and Teitler, S. A. (2013). GYRE: an open-source stellar oscillation code based on a new Magnus Multiple Shooting scheme. , 435(4):3406–3418. [Cited on page 42.]

Unno, W., Osaki, Y., Ando, H., Saio, H., and Shibahashi, H. (1989). *Nonradial oscillations of stars*. [Cited on pages 21, 22, 24, 25, 30, and 77.]

Viallet, M., Meakin, C., Prat, V., and Arnett, D. (2015). Toward a consistent use of overshooting parametrizations in 1D stellar evolution codes. , 580:A61. [Cited on pages 10 and 13.]

Viani, L. S. and Basu, S. (2020). Examining the Relationship Between Convective Core Overshoot and Stellar Properties Using Asteroseismology. , 904(1):22. [Cited on pages 65 and 66.]

A. Interpolation Errors of $\ell = 1$ Modes Resulting from Interpolation Along Evolutionary Tracks

The following table of tables presents the average offset (μ) and maximum error (m) (in μHz) from the "interpolation along" method (that considers the indicated interpolation method along evolutionary tracks), for all $\ell = 1$ modes obtained for the interpolated tracks of the initial grid, with the interpolated mass value indicated on the top-left cell of each table.

Table A.1: Average offsets (μ) and maximum errors (m) from interpolation along evolutionary tracks. The results are for all $\ell = 1$ modes associated with the missing models of each evolutionary track of the stellar grid, determined from interpolation using adjacent models of the same evolutionary track, for each of the age proxies indicated. We notice that, for all cases, interpolation errors are the same for τ and τ_{scaled} as the age proxies (due to the reasons explained in Section 2.3.1).

M=1.150 $M_\odot$	Errors	Linear	Cubic Splines
τ, τ_{scaled}	μ (μHz)	2.9×10^{-3}	1.3×10^{-4}
	m (μHz)	9.0×10^{-2}	5.6×10^{-3}
ρ_c	μ (μHz)	2.7×10^{-3}	1.2×10^{-4}
	m (μHz)	7.8×10^{-2}	5.6×10^{-3}

M=1.155 $M_\odot$	Errors	Linear	Cubic Splines
τ, τ_{scaled}	μ (μHz)	2.9×10^{-3}	1.3×10^{-4}
	m (μHz)	9.0×10^{-2}	4.7×10^{-3}
τ	μ (μHz)	2.8×10^{-3}	1.3×10^{-4}
	m (μHz)	8.1×10^{-2}	4.6×10^{-3}

M=1.160 $M_\odot$	Errors	Linear	Cubic Splines
τ, τ_{scaled}	μ (μHz)	3.0×10^{-3}	1.3×10^{-4}
	m (μHz)	9.4×10^{-2}	5.0×10^{-3}
τ	μ (μHz)	2.9×10^{-3}	1.2×10^{-4}
	m (μHz)	8.2×10^{-2}	4.9×10^{-3}

M=1.165 $M_\odot$	Errors	Linear	Cubic Splines
τ, τ_{scaled}	μ (μHz)	3.1×10^{-3}	1.3×10^{-4}
	m (μHz)	9.4×10^{-2}	5.5×10^{-3}
ρ_c	μ (μHz)	2.9×10^{-3}	1.3×10^{-4}
	m (μHz)	8.2×10^{-2}	5.4×10^{-3}

M=1.170 $M_\odot$	Errors	Linear	Cubic Splines
τ, τ_{scaled}	μ (μHz)	3.1×10^{-3}	1.2×10^{-4}
	m (μHz)	9.3×10^{-2}	4.3×10^{-3}
ρ_c	μ (μHz)	3.0×10^{-3}	1.2×10^{-4}
	m (μHz)	8.3×10^{-2}	4.2×10^{-3}

M=1.175 $M_\odot$	Errors	Linear	Cubic Splines
τ, τ_{scaled}	μ (μHz)	3.2×10^{-3}	1.2×10^{-4}
	m (μHz)	9.6×10^{-2}	5.4×10^{-3}
ρ_c	μ (μHz)	3.0×10^{-3}	1.2×10^{-4}
	m (μHz)	8.4×10^{-2}	4.9×10^{-3}

M=1.180 $M_\odot$	Errors	Linear	Cubic Splines
τ, τ_{scaled}	μ (μHz)	3.6×10^{-3}	2.4×10^{-4}
	m (μHz)	1.4×10^{-1}	3.1×10^{-2}
ρ_c	μ (μHz)	3.4×10^{-3}	3.5×10^{-4}
	m (μHz)	1.1×10^{-1}	3.2×10^{-2}

M=1.185 $M_\odot$	Errors	Linear	Cubic Splines
τ, τ_{scaled}	μ (μHz)	3.7×10^{-3}	2.4×10^{-4}
	m (μHz)	1.4×10^{-1}	5.3×10^{-2}
ρ_c	μ (μHz)	3.6×10^{-3}	4.0×10^{-4}
	m (μHz)	1.4×10^{-1}	5.1×10^{-2}

M=1.190 $M_\odot$	Errors	Linear	Cubic Splines
τ, τ_{scaled}	μ (μHz)	3.8×10^{-3}	2.1×10^{-4}
	m (μHz)	1.5×10^{-1}	1.6×10^{-2}
ρ_c	μ (μHz)	3.9×10^{-3}	3.6×10^{-4}
	m (μHz)	1.1×10^{-1}	3.1×10^{-2}

M=1.195 $M_\odot$	Errors	Linear	Cubic Splines
τ, τ_{scaled}	μ (μHz)	4.0×10^{-3}	2.8×10^{-4}
	m (μHz)	1.7×10^{-1}	3.0×10^{-2}
ρ_c	μ (μHz)	4.0×10^{-3}	3.5×10^{-4}
	m (μHz)	1.3×10^{-1}	2.8×10^{-2}

M=1.200 $M_\odot$	Errors	Linear	Cubic Splines
τ, τ_{scaled}	μ (μHz)	4.2×10^{-3}	2.7×10^{-4}
	m (μHz)	1.6×10^{-1}	4.6×10^{-2}
ρ_c	μ (μHz)	4.4×10^{-3}	4.6×10^{-4}
	m (μHz)	1.5×10^{-1}	4.7×10^{-2}

M=1.205 $M_\odot$	Errors	Linear	Cubic Splines
τ, τ_{scaled}	μ (μHz)	4.4×10^{-3}	3.6×10^{-4}
	m (μHz)	1.7×10^{-1}	8.4×10^{-2}
ρ_c	μ (μHz)	4.6×10^{-3}	5.5×10^{-4}
	m (μHz)	1.4×10^{-1}	8.3×10^{-2}

M=1.210 $M_\odot$	Errors	Linear	Cubic Splines
τ, τ_{scaled}	μ (μHz)	4.4×10^{-3}	2.6×10^{-4}
	m (μHz)	1.6×10^{-1}	3.7×10^{-2}
ρ_c	μ (μHz)	4.6×10^{-3}	4.1×10^{-4}
	m (μHz)	1.5×10^{-1}	3.9×10^{-2}

M=1.215 $M_\odot$	Errors	Linear	Cubic Splines
τ, τ_{scaled}	μ (μHz)	4.7×10^{-3}	2.9×10^{-4}
	m (μHz)	1.7×10^{-1}	5.3×10^{-2}
ρ_c	μ (μHz)	4.9×10^{-3}	4.5×10^{-4}
	m (μHz)	1.5×10^{-1}	5.8×10^{-2}

M=1.220 $M_\odot$	Errors	Linear	Cubic Splines
τ, τ_{scaled}	μ (μHz)	4.7×10^{-3}	2.6×10^{-4}
	m (μHz)	1.8×10^{-1}	4.2×10^{-2}
ρ_c	μ (μHz)	5.0×10^{-3}	4.4×10^{-4}
	m (μHz)	1.5×10^{-1}	5.5×10^{-2}

M=1.225 $M_\odot$	Errors	Linear	Cubic Splines
τ, τ_{scaled}	μ (μHz)	4.9×10^{-3}	3.1×10^{-4}
	m (μHz)	2.0×10^{-1}	4.4×10^{-2}
ρ_c	μ (μHz)	5.4×10^{-3}	6.2×10^{-4}
	m (μHz)	1.6×10^{-1}	7.1×10^{-2}

M=1.230 $M_\odot$	Errors	Linear	Cubic Splines
τ, τ_{scaled}	μ (μHz)	5.0×10^{-3}	2.5×10^{-4}
	m (μHz)	1.9×10^{-1}	5.2×10^{-2}
ρ_c	μ (μHz)	5.3×10^{-3}	5.4×10^{-4}
	m (μHz)	1.5×10^{-1}	6.0×10^{-2}

M=1.235 $M_\odot$	Errors	Linear	Cubic Splines
τ, τ_{scaled}	μ (μHz)	5.1×10^{-3}	2.5×10^{-4}
	m (μHz)	1.7×10^{-1}	3.5×10^{-2}
ρ_c	μ (μHz)	5.5×10^{-3}	5.1×10^{-4}
	m (μHz)	1.6×10^{-1}	8.9×10^{-2}

M=1.240 $M_\odot$	Errors	Linear	Cubic Splines
τ, τ_{scaled}	μ (μHz)	5.3×10^{-3}	2.8×10^{-4}
	m (μHz)	1.8×10^{-1}	5.3×10^{-2}
ρ_c	μ (μHz)	5.5×10^{-3}	5.1×10^{-4}
	m (μHz)	2.0×10^{-1}	7.8×10^{-2}

M=1.245 $M_\odot$	Errors	Linear	Cubic Splines
τ, τ_{scaled}	μ (μHz)	5.4×10^{-3}	2.3×10^{-4}
	m (μHz)	1.7×10^{-1}	3.0×10^{-2}
ρ_c	μ (μHz)	5.5×10^{-3}	3.4×10^{-4}
	m (μHz)	1.8×10^{-1}	3.3×10^{-2}

M=1.250 $M_\odot$	Errors	Linear	Cubic Splines
τ, τ_{scaled}	μ (μHz)	5.4×10^{-3}	2.4×10^{-4}
	m (μHz)	2.0×10^{-1}	2.2×10^{-2}
ρ_c	μ (μHz)	5.6×10^{-3}	4.5×10^{-4}
	m (μHz)	1.8×10^{-1}	5.5×10^{-2}

M=1.255 $M_\odot$	Errors	Linear	Cubic Splines
τ, τ_{scaled}	μ (μHz)	5.6×10^{-3}	2.9×10^{-4}
	m (μHz)	1.8×10^{-1}	5.1×10^{-2}
ρ_c	μ (μHz)	5.6×10^{-3}	5.1×10^{-4}
	m (μHz)	1.7×10^{-1}	8.3×10^{-2}

M=1.260 $M_\odot$	Errors	Linear	Cubic Splines
τ, τ_{scaled}	μ (μHz)	5.5×10^{-3}	2.6×10^{-4}
	m (μHz)	1.8×10^{-1}	5.9×10^{-2}
ρ_c	μ (μHz)	5.6×10^{-3}	4.0×10^{-4}
	m (μHz)	1.7×10^{-1}	6.4×10^{-2}

M=1.265 $M_\odot$	Errors	Linear	Cubic Splines
τ, τ_{scaled}	μ (μHz)	5.5×10^{-3}	2.5×10^{-4}
	m (μHz)	1.8×10^{-1}	4.7×10^{-2}
ρ_c	μ (μHz)	5.5×10^{-3}	3.7×10^{-4}
	m (μHz)	1.7×10^{-1}	4.6×10^{-2}

M=1.270 $M_\odot$	Errors	Linear	Cubic Splines
τ, τ_{scaled}	μ (μHz)	5.5×10^{-3}	2.8×10^{-4}
	m (μHz)	1.7×10^{-1}	4.1×10^{-2}
ρ_c	μ (μHz)	5.5×10^{-3}	4.6×10^{-4}
	m (μHz)	1.7×10^{-1}	5.9×10^{-2}

M=1.275 $M_\odot$	Errors	Linear	Cubic Splines
τ, τ_{scaled}	μ (μHz)	5.5×10^{-3}	3.7×10^{-4}
	m (μHz)	1.7×10^{-1}	5.6×10^{-2}
ρ_c	μ (μHz)	5.4×10^{-3}	5.4×10^{-4}
	m (μHz)	1.7×10^{-1}	6.0×10^{-2}

M=1.280 $M_\odot$	Errors	Linear	Cubic Splines
τ, τ_{scaled}	μ (μHz)	5.4×10^{-3}	2.7×10^{-4}
	m (μHz)	1.8×10^{-1}	4.4×10^{-2}
ρ_c	μ (μHz)	5.4×10^{-3}	4.8×10^{-4}
	m (μHz)	1.8×10^{-1}	6.6×10^{-2}

M=1.285 $M_\odot$	Errors	Linear	Cubic Splines
τ, τ_{scaled}	μ (μHz)	5.3×10^{-3}	2.2×10^{-4}
	m (μHz)	1.7×10^{-1}	2.8×10^{-2}
ρ_c	μ (μHz)	5.3×10^{-3}	3.9×10^{-4}
	m (μHz)	1.7×10^{-1}	7.2×10^{-2}

M=1.290 $M_\odot$	Errors	Linear	Cubic Splines
τ, τ_{scaled}	μ (μHz)	5.2×10^{-3}	2.7×10^{-4}
	m (μHz)	1.7×10^{-1}	5.1×10^{-2}
ρ_c	μ (μHz)	5.3×10^{-3}	4.8×10^{-4}
	m (μHz)	1.6×10^{-1}	9.7×10^{-2}

M=1.295 $M_\odot$	Errors	Linear	Cubic Splines
τ, τ_{scaled}	μ (μHz)	5.2×10^{-3}	3.4×10^{-4}
	m (μHz)	1.7×10^{-1}	7.0×10^{-2}
ρ_c	μ (μHz)	5.2×10^{-3}	4.6×10^{-4}
	m (μHz)	1.6×10^{-1}	7.0×10^{-2}

M=1.300 $M_\odot$	Errors	Linear	Cubic Splines
τ, τ_{scaled}	μ (μHz)	5.1×10^{-3}	2.1×10^{-4}
	m (μHz)	1.7×10^{-1}	1.8×10^{-2}
ρ_c	μ (μHz)	5.0×10^{-3}	3.0×10^{-4}
	m (μHz)	1.6×10^{-1}	3.6×10^{-2}

M=1.305 $M_\odot$	Errors	Linear	Cubic Splines
τ, τ_{scaled}	μ (μHz)	5.0×10^{-3}	3.1×10^{-4}
	m (μHz)	1.7×10^{-1}	4.4×10^{-2}
ρ_c	μ (μHz)	5.1×10^{-3}	4.7×10^{-4}
	m (μHz)	1.7×10^{-1}	6.0×10^{-2}

M=1.310 $M_\odot$	Errors	Linear	Cubic Splines
τ, τ_{scaled}	μ (μHz)	4.9×10^{-3}	2.6×10^{-4}
	m (μHz)	1.7×10^{-1}	3.9×10^{-2}
ρ_c	μ (μHz)	4.9×10^{-3}	4.0×10^{-4}
	m (μHz)	1.7×10^{-1}	7.1×10^{-2}

M=1.315 $M_\odot$	Errors	Linear	Cubic Splines
τ, τ_{scaled}	μ (μHz)	4.8×10^{-3}	3.4×10^{-4}
	m (μHz)	1.7×10^{-1}	1.0×10^{-1}
ρ_c	μ (μHz)	4.8×10^{-3}	4.5×10^{-4}
	m (μHz)	1.6×10^{-1}	1.1×10^{-1}

M=1.320 $M_\odot$	Errors	Linear	Cubic Splines
τ, τ_{scaled}	μ (μHz)	4.7×10^{-3}	3.1×10^{-4}
	m (μHz)	1.8×10^{-1}	5.9×10^{-2}
ρ_c	μ (μHz)	4.8×10^{-3}	4.4×10^{-4}
	m (μHz)	1.6×10^{-1}	7.3×10^{-2}

M=1.325 $M_\odot$	Errors	Linear	Cubic Splines
τ, τ_{scaled}	μ (μHz)	4.6×10^{-3}	2.5×10^{-4}
	m (μHz)	1.9×10^{-1}	5.0×10^{-2}
ρ_c	μ (μHz)	4.6×10^{-3}	3.0×10^{-4}
	m (μHz)	1.5×10^{-1}	5.1×10^{-2}

M=1.330 $M_\odot$	Errors	Linear	Cubic Splines
τ, τ_{scaled}	μ (μHz)	4.5×10^{-3}	2.5×10^{-4}
	m (μHz)	1.9×10^{-1}	4.8×10^{-2}
ρ_c	μ (μHz)	4.6×10^{-3}	3.3×10^{-4}
	m (μHz)	1.6×10^{-1}	7.4×10^{-2}

M=1.335 $M_\odot$	Errors	Linear	Cubic Splines
τ, τ_{scaled}	μ (μHz)	4.4×10^{-3}	2.9×10^{-4}
	m (μHz)	1.8×10^{-1}	4.9×10^{-2}
ρ_c	μ (μHz)	4.4×10^{-3}	3.3×10^{-4}
	m (μHz)	1.5×10^{-1}	4.9×10^{-2}

M=1.340 $M_\odot$	Errors	Linear	Cubic Splines
τ, τ_{scaled}	μ (μHz)	4.2×10^{-3}	2.0×10^{-4}
	m (μHz)	1.9×10^{-1}	6.0×10^{-2}
ρ_c	μ (μHz)	4.2×10^{-3}	2.5×10^{-4}
	m (μHz)	2.0×10^{-1}	5.7×10^{-2}

M=1.345 $M_\odot$	Errors	Linear	Cubic Splines
τ, τ_{scaled}	μ (μHz)	4.1×10^{-3}	2.0×10^{-4}
	m (μHz)	2.0×10^{-1}	3.5×10^{-2}
ρ_c	μ (μHz)	4.1×10^{-3}	3.1×10^{-4}
	m (μHz)	1.6×10^{-1}	5.4×10^{-2}

M=1.350 $M_\odot$	Errors	Linear	Cubic Splines
τ, τ_{scaled}	μ (μHz)	4.0×10^{-3}	2.5×10^{-4}
	m (μHz)	2.0×10^{-1}	4.8×10^{-2}
ρ_c	μ (μHz)	4.0×10^{-3}	3.2×10^{-4}
	m (μHz)	1.5×10^{-1}	6.4×10^{-2}

B. Interpolation Errors of $\ell = 1$ Modes Resulting from the Full Interpolation Algorithm

The following table of tables presents the average offset (μ) and maximum error (m) (in μHz) from the full interpolation method (that considers cubic splines along evolutionary tracks and the indicated interpolation method across evolutionary tracks), for all $\ell = 1$ modes obtained for the interpolated tracks of the initial grid, with the interpolated mass value indicated on the top-left cell of each table.

Table B.1: Average offsets (μ) and maximum errors (m) from the full interpolation algorithm (that considers cubic splines along tracks and the indicated interpolation method across tracks). The results are for all $\ell = 1$ modes associated with the interpolated evolutionary tracks of the grid (i.e., those whose third decimal place of the associated mass value is 5), determined from interpolation using adjacent evolutionary tracks, for each of the age proxies indicated.

M=1.155 $M_\odot$	Errors	Linear	Cubic Splines
τ	μ (μHz)	1.2×10^{1}	—
	m (μHz)	3.6×10^{1}	—
τ_{scaled}	μ (μHz)	4.2×10^{-2}	—
	m (μHz)	3.8×10^{-1}	—
ρ_c	μ (μHz)	4.0×10^{-2}	—
	m (μHz)	4.5×10^{-1}	—

M=1.165 $M_\odot$	Errors	Linear	Cubic Splines
τ	μ (μHz)	1.2×10^{1}	1.1×10^{1}
	m (μHz)	3.5×10^{1}	3.0×10^{1}
τ_{scaled}	μ (μHz)	2.7×10^{-2}	1.5×10^{0}
	m (μHz)	2.8×10^{-1}	3.5×10^{0}
ρ_c	μ (μHz)	3.4×10^{-2}	2.1×10^{-1}
	m (μHz)	3.8×10^{-1}	9.5×10^{-1}

M=1.175 $M_\odot$	Errors	Linear	Cubic Splines
τ	μ (μHz)	1.2×10^{1}	1.1×10^{1}
	m (μHz)	3.4×10^{1}	2.9×10^{1}
τ_{scaled}	μ (μHz)	1.2×10^{1}	1.2×10^{1}
	m (μHz)	2.7×10^{1}	2.7×10^{1}
ρ_c	μ (μHz)	1.7×10^{0}	1.7×10^{0}
	m (μHz)	7.7×10^{0}	7.5×10^{0}

M=1.185 $M_\odot$	Errors	Linear	Cubic Splines
τ	μ (μHz)	8.2×10^{0}	1.1×10^{1}
	m (μHz)	3.1×10^{1}	3.0×10^{1}
τ_{scaled}	μ (μHz)	9.4×10^{-2}	1.8×10^{0}
	m (μHz)	7.0×10^{-1}	3.7×10^{0}
ρ_c	μ (μHz)	6.9×10^{-2}	2.2×10^{-1}
	m (μHz)	4.5×10^{-1}	1.1×10^{0}

M=1.195 $M_\odot$	Errors	Linear	Cubic Splines
τ	μ (μHz)	7.8×10^{0}	7.4×10^{0}
	m (μHz)	2.9×10^{1}	3.0×10^{1}
τ_{scaled}	μ (μHz)	2.1×10^{-1}	8.3×10^{-2}
	m (μHz)	1.6×10^{0}	1.1×10^{1}
ρ_c	μ (μHz)	1.6×10^{-1}	1.6×10^{-1}
	m (μHz)	1.2×10^{0}	1.1×10^{0}

M=1.205 $M_\odot$	Errors	Linear	Cubic Splines
τ	μ (μHz)	7.5×10^{0}	6.9×10^{0}
	m (μHz)	2.7×10^{1}	2.9×10^{1}
τ_{scaled}	μ (μHz)	2.4×10^{-1}	1.3×10^{-1}
	m (μHz)	1.7×10^{0}	1.3×10^{0}
ρ_c	μ (μHz)	1.2×10^{-1}	1.1×10^{-1}
	m (μHz)	1.1×10^{0}	1.0×10^{0}

M=1.215 $M_\odot$	Errors	Linear	Cubic Splines
τ	μ (μHz)	7.4×10^{0}	6.7×10^{0}
	m (μHz)	2.5×10^{1}	2.9×10^{1}
τ_{scaled}	μ (μHz)	1.4×10^{-1}	1.8×10^{-1}
	m (μHz)	1.6×10^{0}	1.2×10^{0}
ρ_c	μ (μHz)	6.5×10^{-2}	7.2×10^{-2}
	m (μHz)	6.0×10^{-1}	6.7×10^{-1}

M=1.225 $M_\odot$	Errors	Linear	Cubic Splines
τ	μ (μHz)	7.3×10^{0}	6.4×10^{0}
	m (μHz)	2.5×10^{1}	2.8×10^{1}
τ_{scaled}	μ (μHz)	1.1×10^{-1}	1.3×10^{-1}
	m (μHz)	1.4×10^{0}	7.4×10^{-1}
ρ_c	μ (μHz)	4.9×10^{-2}	6.2×10^{-2}
	m (μHz)	4.9×10^{-1}	4.9×10^{-1}

M=1.235 $M_\odot$	Errors	Linear	Cubic Splines
τ	μ (μHz)	7.3×10^{0}	6.4×10^{0}
	m (μHz)	2.5×10^{1}	2.7×10^{1}
τ_{scaled}	μ (μHz)	5.5×10^{-1}	5.3×10^{-1}
	m (μHz)	4.5×10^{0}	3.9×10^{0}
ρ_c	μ (μHz)	1.4×10^{-1}	1.4×10^{-1}
	m (μHz)	1.2×10^{0}	1.3×10^{0}

M=1.245 $M_\odot$	Errors	Linear	Cubic Splines
τ	μ (μHz)	7.3×10^{0}	6.1×10^{0}
	m (μHz)	2.6×10^{1}	2.7×10^{1}
τ_{scaled}	μ (μHz)	5.6×10^{-1}	5.7×10^{-1}
	m (μHz)	3.6×10^{0}	3.3×10^{0}
ρ_c	μ (μHz)	1.4×10^{-1}	1.5×10^{-1}
	m (μHz)	1.2×10^{0}	1.3×10^{0}

M=1.255 $M_\odot$	Errors	Linear	Cubic Splines
τ	μ (μHz)	7.2×10^{0}	6.2×10^{0}
	m (μHz)	2.6×10^{1}	2.7×10^{1}
τ_{scaled}	μ (μHz)	1.5×10^{-1}	1.1×10^{-1}
	m (μHz)	1.7×10^{0}	9.9×10^{-1}
ρ_c	μ (μHz)	2.7×10^{-2}	1.8×10^{-2}
	m (μHz)	3.1×10^{-1}	2.5×10^{-1}

M=1.265 $M_\odot$	Errors	Linear	Cubic Splines
τ	μ (μHz)	7.1×10^{0}	6.1×10^{0}
	m (μHz)	2.6×10^{1}	2.6×10^{1}
τ_{scaled}	μ (μHz)	9.1×10^{-1}	9.4×10^{-1}
	m (μHz)	6.1×10^{0}	5.7×10^{0}
ρ_c	μ (μHz)	2.0×10^{-1}	2.1×10^{-1}
	m (μHz)	1.7×10^{0}	1.8×10^{0}

M=1.275 $M_\odot$	Errors	Linear	Cubic Splines
τ	μ (μHz)	7.2×10^{0}	6.0×10^{0}
	m (μHz)	2.6×10^{1}	2.5×10^{1}
τ_{scaled}	μ (μHz)	3.0×10^{-1}	2.1×10^{-1}
	m (μHz)	3.3×10^{0}	2.4×10^{0}
ρ_c	μ (μHz)	4.4×10^{-2}	3.5×10^{-2}
	m (μHz)	4.8×10^{-1}	2.7×10^{-1}

M=1.285 $M_\odot$	Errors	Linear	Cubic Splines
τ	μ (μHz)	7.3×10^{0}	6.0×10^{0}
	m (μHz)	2.7×10^{1}	2.3×10^{1}
τ_{scaled}	μ (μHz)	7.0×10^{-1}	7.1×10^{-1}
	m (μHz)	5.4×10^{0}	4.7×10^{0}
ρ_c	μ (μHz)	1.6×10^{-1}	1.7×10^{-1}
	m (μHz)	1.1×10^{0}	1.2×10^{0}

M=1.295 $M_\odot$	Errors	Linear	Cubic Splines
τ	μ (μHz)	7.2×10^{0}	6.0×10^{0}
	m (μHz)	2.7×10^{1}	2.3×10^{1}
τ_{scaled}	μ (μHz)	5.4×10^{-1}	5.6×10^{-1}
	m (μHz)	4.2×10^{0}	3.5×10^{0}
ρ_c	μ (μHz)	1.2×10^{-1}	1.2×10^{-1}
	m (μHz)	8.8×10^{-1}	8.8×10^{-1}

M=1.305 $M_\odot$	Errors	Linear	Cubic Splines
τ	μ (μHz)	7.3×10^{0}	6.1×10^{0}
	m (μHz)	2.7×10^{1}	2.2×10^{1}
τ_{scaled}	μ (μHz)	6.6×10^{-1}	6.0×10^{-1}
	m (μHz)	5.8×10^{0}	5.0×10^{0}
ρ_c	μ (μHz)	1.1×10^{-1}	9.7×10^{-2}
	m (μHz)	7.4×10^{-1}	7.2×10^{-1}

M=1.315 $M_\odot$	Errors	Linear	Cubic Splines
τ	μ (μHz)	7.3×10^{0}	6.1×10^{0}
	m (μHz)	2.6×10^{1}	2.2×10^{1}
τ_{scaled}	μ (μHz)	2.5×10^{-1}	1.7×10^{-1}
	m (μHz)	2.9×10^{0}	1.8×10^{0}
ρ_c	μ (μHz)	4.0×10^{-2}	3.3×10^{-2}
	m (μHz)	2.8×10^{-1}	2.4×10^{-1}

M=1.325 $M_\odot$	Errors	Linear	Cubic Splines
τ	μ (μHz)	7.4×10^{0}	6.3×10^{0}
	m (μHz)	2.5×10^{1}	2.2×10^{1}
τ_{scaled}	μ (μHz)	5.1×10^{-1}	3.6×10^{-1}
	m (μHz)	5.0×10^{0}	4.0×10^{0}
ρ_c	μ (μHz)	1.1×10^{-1}	9.4×10^{-2}
	m (μHz)	6.8×10^{-1}	6.1×10^{-1}

M=1.335 $M_\odot$	Errors	Linear	Cubic Splines
τ	μ (μHz)	7.5×10^{0}	6.4×10^{0}
	m (μHz)	2.3×10^{1}	2.2×10^{1}
τ_{scaled}	μ (μHz)	8.6×10^{-1}	8.1×10^{-1}
	m (μHz)	7.0×10^{0}	6.2×10^{0}
ρ_c	μ (μHz)	1.5×10^{-1}	1.4×10^{-1}
	m (μHz)	9.6×10^{-1}	9.5×10^{-1}

M=1.345 $M_\odot$	Errors	Linear	Cubic Splines
τ	μ (μHz)	7.7×10^{0}	—
	m (μHz)	2.3×10^{1}	—
τ_{scaled}	μ (μHz)	4.1×10^{-1}	—
	m (μHz)	4.0×10^{0}	—
ρ_c	μ (μHz)	4.1×10^{-2}	—
	m (μHz)	4.5×10^{-1}	—

C. Testing Grid Resolution

In Section 2.3.6, we tested the resolution of the initial grid by determining and comparing the values of both μ and m obtained through the application of interpolation along the evolutionary tracks of different subgrids, with each evolutionary track of each subgrid being built by collecting every k^{th} model of the initial track. We observed that both μ and m increase by a significant factor whenever the grid resolution is reduced, regardless of the cubic (polynomial or splines) interpolation method considered.

However, in the case of cubic polynomial interpolation methods, we expected the interpolation errors to increase by a factor of k^4 relative to the errors from the initial grid*. In other words, because the interpolation method approximates the real frequency function using a Taylor expansion of the form

$$f(x) \simeq f(a) + \frac{1}{1!}\frac{df(a)}{dx}(x-a) + \frac{1}{2!}\frac{d^2f(a)}{dx^2}(x-a)^2 + \frac{1}{3!}\frac{d^3f(a)}{dx^3}(x-a)^3 + \mathcal{O}(x^4), \quad \text{(C.1)}$$

that ignores the higher-order term $\mathcal{O}(x^4)$, we expected the ratio between the errors in the initial grid and those in the reduced subgrid, $\mu(1/1)/\mu(1/k)$, to be approximately k^4. However, this was not observed to be the case.

In this Appendix, we explain the tests conducted on our interpolation algorithm to investigate why the interpolation errors do not follow the expected increase with grid resolution.

To simulate the evolution of an $\ell = 1$ frequency mode in our initial grid, specifically in the region of the subgiant phase where the largest interpolation errors have been observed in our main work (ρ_c = [1000,3000] g.cm^{-3}), we generated two frequency functions (in their normalized form), using the equation

$$\begin{aligned}\nu_{1,n,\text{norm}}(\rho_c) = 3.0 + 0.03 \cdot \arctan(0.05(\rho_c - 1180)) + \\ + 0.02 \cdot \arctan(0.02(\rho_c - 1750)) + 0.01 \cdot \arctan(0.01(\rho_c - 2600)).\end{aligned} \quad \text{(C.2)}$$

The difference between the two frequency functions lies in the number of models calculated. One function was determined with 200 initial models distributed within the mentioned parameter space, representing a model density similar to that of our initial grid

*For cubic splines, the situation is less clear, due to piece-wise nature of the method (Sonneveld, 1969).

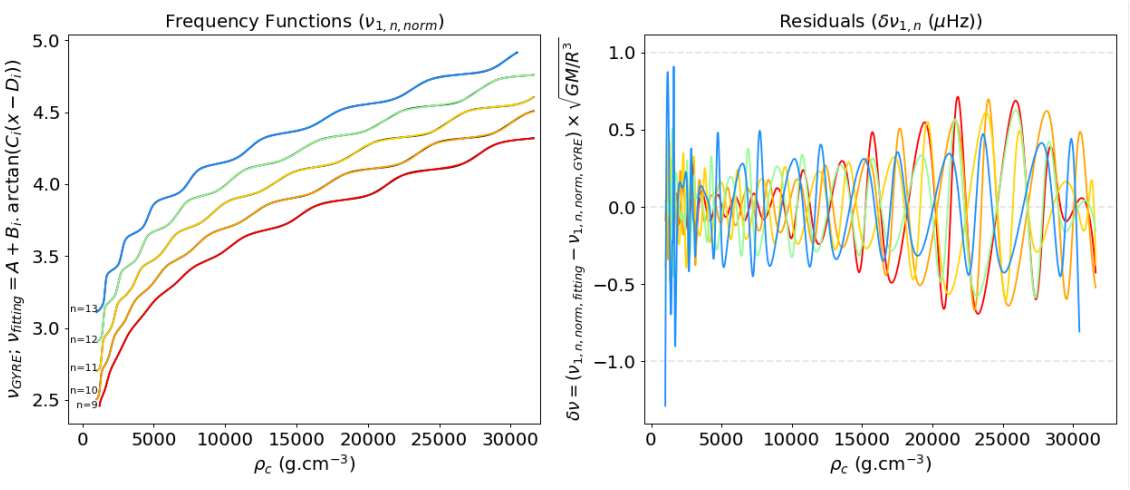


Figure C.1: Results of applying the fitting function described in Section 4.1 to $\ell = 1$ frequency modes with radial orders n = [9,10,11,12,13], computed using GYRE for the mass track with 1.245 $M_\odot$ from our initial grid. The frequency curves, expressed as a function of ρ_c, are fitted using Equation 4.13, with A, B_i, C_i and D_i as the fitting parameters specific to each frequency curve. The frequency curves determined by GYRE (black) and the fitted frequency curves (coloured) are displayed on the left panel. The residuals, calculated as the differences between the frequencies calculated with GYRE and the frequencies estimated from the fitting functions, multiplied by the normalizing factor $\sqrt{GM/R^3}$, are shown on the right panel, in μHz units.

($\Delta\rho_c = 10$ g.cm^{-3}). The second function was determined with 2000 initial models uniformly distributed in the same parameter space, representing a model density 10 times larger than that of our initial grid ($\Delta\rho_c = 1$ g.cm^{-3}).

We chose to use fitting functions instead of asteroseismic codes like GYRE to generate the frequency data for this study, as generating a stellar grid with evolutionary tracks containing such a large number of models requires considerable computation time and storage, reducing the computational efficiency of the algorithm (as discussed in Section 1.5). Furthermore, we have also shown (in Chapter 4) that a sum of arctangent-type functions can well reproduce the frequencies generated by asteroseismic algorithms like GYRE for the initial grid, usually being able to reproduce such frequencies with errors smaller than 1.0 μHz (as shown in Figure C.1).

The results of applying the three interpolation algorithms - linear, cubic polynomial, and cubic splines - to both our frequency curves are displayed in Figure C.2 and Table C.1. Figure C.2 presents the results for the frequency curve with 200 initial models on the left and the frequency curve with 2000 initial models on the right, with their respective degraded versions distinguished by different colours. The top row displays the results for the three interpolation methods, comparing them against the original frequency curves. The three bottom rows depict the respective interpolation errors for each method considered

Table C.1: Average offsets (μ) resulting from interpolation along frequency curves determined using Equation C.2 (with 200 and 2000 initial models), when considering three interpolation methods (linear on top, cubic polynomial in the middle, and cubic splines at the bottom), ρ_c as the age proxy, and the indicated grid resolutions, $1/k$.

	Method for Interpolation Along				
Resolution	200 initial models Linear	Error Factor	2000 initial models Linear	Error Factor	Expected Error Factor
1/1	1.6×10^{-4}	1.0	1.6×10^{-6}	1.0	1
1/2	3.6×10^{-4}	2.2	6.3×10^{-6}	4.0	4
1/3	1.4×10^{-3}	8.6	1.4×10^{-5}	9.0	9
1/4	2.0×10^{-3}	12.1	2.5×10^{-5}	15.6	16
1/5	2.8×10^{-3}	17.0	4.0×10^{-5}	25.2	25
1/6	1.4×10^{-3}	8.3	5.7×10^{-5}	36.3	36
Resolution	200 initial models Cubic Polynomial	Error Factor	2000 initial models Cubic Polynomial	Error Factor	Expected Error Factor
1/1	5.2×10^{-5}	1.0	7.0×10^{-9}	1.0	1
1/2	5.8×10^{-5}	1.1	1.2×10^{-7}	15.8	16
1/3	1.1×10^{-3}	20.8	5.6×10^{-7}	77.3	81
1/4	1.5×10^{-3}	28.9	1.5×10^{-6}	211.2	256
1/5	2.0×10^{-3}	38.8	4.2×10^{-6}	572.1	625
1/6	1.1×10^{-3}	20.6	8.2×10^{-6}	1131.5	1296
Resolution	200 initial models Cubic Splines	Error Factor	2000 initial models Cubic Splines	Error Factor	Expected Error Factor
1/1	4.4×10^{-5}	1.0	8.0×10^{-10}	1.0	1
1/2	1.5×10^{-4}	3.3	1.5×10^{-8}	17.5	16
1/3	1.2×10^{-3}	26.8	8.7×10^{-8}	104.2	81
1/4	1.9×10^{-3}	42.8	2.7×10^{-7}	326.5	256
1/5	3.4×10^{-3}	79.0	1.1×10^{-6}	1285.2	625
1/6	3.6×10^{-3}	81.6	3.3×10^{-6}	3893.6	1296

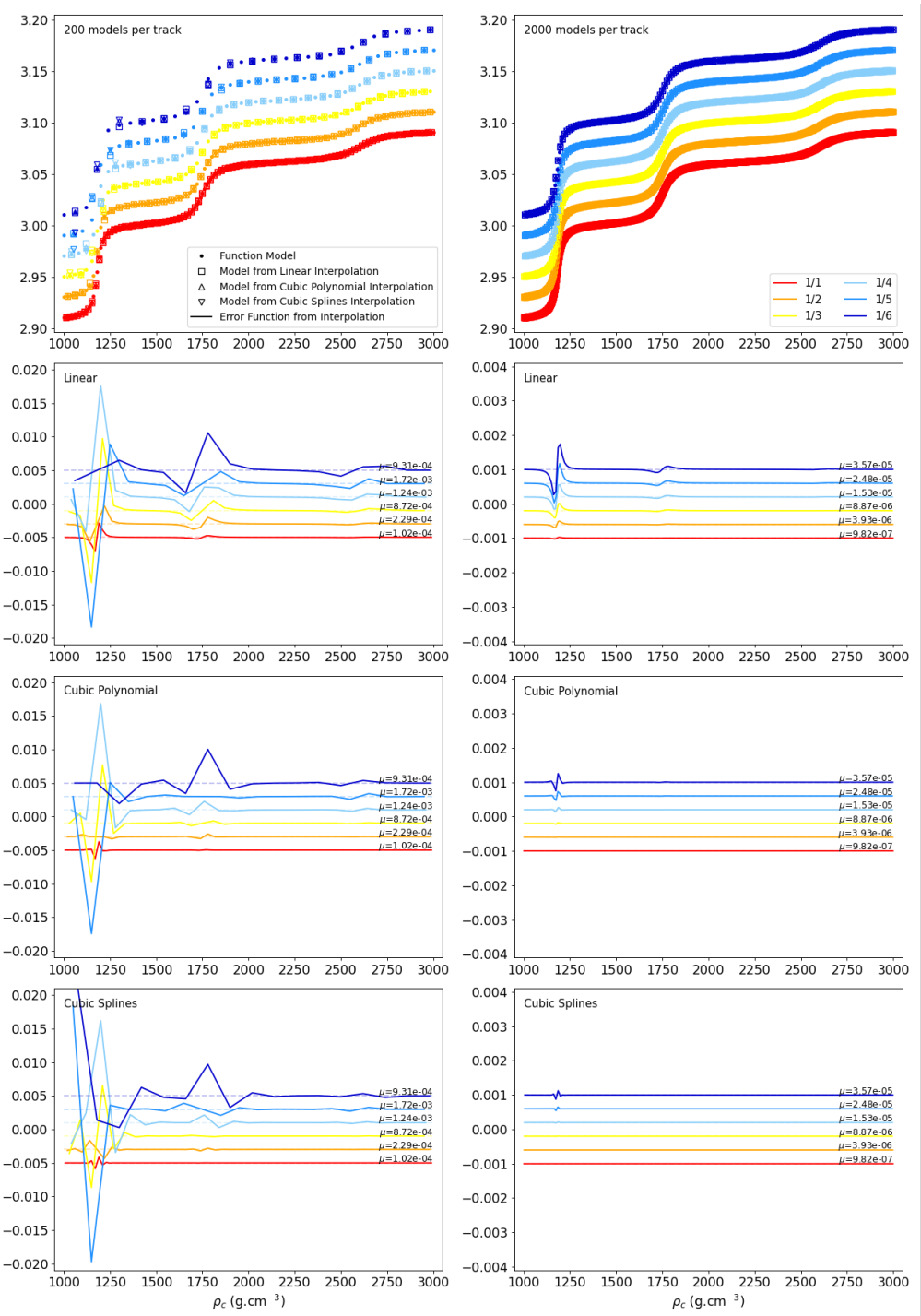


Figure C.2: Results of interpolation tests applied to the resolution of frequency modes of an evolutionary track in the subgiant phase. The plots compare the results of interpolation applied to two frequency functions, one with an original track of 200 models (left) and another with 2000 models (right), and of their degraded versions, whose resolution $1/k$ in respect to the original function (track 1/1, in red) is indicated by different colours. (Top row) Interpolation results for each of the 3 tested methods: linear (□), cubic polynomial (△), and cubic splines (▽), and for each of the resolutions considered. (Three bottom rows) Interpolation errors that result from interpolation applied to each of the tracks, for each of the methods considered (linear in the second row, cubic polynomials in the third row, and cubic splines in the fourth row), for each of the resolutions considered. The corresponding average offset μ for each error function is also presented. In all plots, the results have been vertically split for visualization purposes (with no effects on the interpolation code). As a reference, $\delta\nu = 0.0$ μHz is indicated by a dashed line for each interpolation error function.

(linear in the second row, cubic polynomials in the third row, and cubic splines in the fourth row), along with the corresponding average error displacement.

For the polynomial interpolation methods (both linear and cubic), the results indicate that the degraded curves derived from the 200-model frequency curve do not exhibit the expected error factor of k^4 for cubic interpolation (nor the expected error factor of k^2 in the case of linear interpolation). In contrast, the degraded frequency curves derived from the 2000-model frequency curve do follow the expected scaling. This suggests that our initial grid, where the model spacing for each evolutionary track is comparable to that of the 200-model frequency curve - is not within the regime where this theoretical increment holds. Importantly, this sanity check shows that our interpolation algorithm produces results that are consistent with the theoretical expectations.

Meanwhile, for the cubic spline interpolation, none of the frequency curves follow the error scaling of k^4. This deviation seems to arise from the dependence on the first and second derivatives (see Section 2.2.2) that also contribute to the accuracy of the interpolation method, influencing the scaling factor expected from the neglected residuals from the correspondent Taylor expansion. In our exercise, the error factor for the 200-model case is observed to increase in significantly smaller steps than expected, while for the 2000-model case, the error increments exceed those obtained for the case of cubic polynomials.

In conclusion, these findings indicate that our interpolation routine produces errors that scale as expected under sufficiently high resolution for the stellar grid. However, the deviations observed in the error scaling factors calculated from our results suggest that our initial grid is not dense enough to fall within this regime.